Investigation of the Hemodynamics of Coronary Arteries - Effect of Stenting

Naresh Kumar Coimbatore Selvarasu

Dissertation submitted to the faculty of the Virginia Polytechnic Institute and State University in partial fulfillment of the requirements for the degree of

Doctor of Philosophy
In
Mechanical Engineering

Danesh K. Tafti, Chair
Pavlos P. Vlachos
Mark R. Paul
Mayuresh J. Patil
Raffaella De Vita

April 4th 2013
Blacksburg, Virginia

Keywords: Coronary artery motion, Fluid Structure Interaction (FSI), Curvature, Torsion, Wall Shear Stress, Oscillatory Shear Index, Vorticity Flux Density, Secondary Flow Patterns, Compliance Variation

Investigation of the Hemodynamics of Coronary Arteries - Effect of Stenting

Naresh Kumar Coimbatore Selvarasu

ABSTRACT

Cardiovascular diseases (CVD) are the leading cause of death in the world. According to the World Health Organization (WHO) 17.3 million people died from cardiovascular disease in 2008, representing 30% of all global deaths. The most common modality of treatment of occluded arteries is the use of stents. Despite the widespread use of stents, the incidence of post-stent restenosis is still high. The study of stents in conditions that are similar to in-vivo conditions is limited. This work tries to address the behavior of stents in conditions similar to in-vivo conditions in a generalized framework, thus providing insights for stent design and deployment. Three dimensional, time accurate computational fluid dynamics (CFD) simulations in a pulsatile flow with fluid-structure interaction (FSI) were carried out in realistic coronary arteries, with physiologically relevant flow parameters and dynamics due to induced motion of the heart. In addition, the geometric effects of the stent on the artery were studied to point towards possible beneficial stent deployment strategies. The results suggest that discontinuities in compliance and dynamic geometry cause critical changes in local hemodynamics, namely altering the local pressure and velocity gradients. Increasing the stent length, reducing the transition length and increasing the overexpansion caused adverse flow conditions. From this work, detailed flow characteristics and hemodynamic characteristics due to the compliance mismatch and applied motion were obtained that gave insights towards better stent design and deployment.

Dedicated to my parents and teachers

ACKNOWLEDGEMENTS

This dissertation would not have been possible without the guidance and the help of several individuals who in one way or another contributed and extended their valuable assistance in undertaking and completing of this work. First and foremost, my utmost gratitude to Dr. Danesh Tafti, W. S. Cross Professor of Mechanical Engineering, whose sincerity and encouragement I will never forget. Dr. Tafti has been my inspiration in overcoming all the obstacles in the completion of this research work. I would like to thank my PhD Committee Dr. Mark Paul, Dr. Pavlos Vlachos, Dr. Mayuresh Patil and Dr. Raffaella De Vita for their support, encouragement and insights towards the completion of my research goals. I would like to thank the administrators and staff of the Mechanical Engineering Department for the help and support during the course of the last few years. I would like to thank my lab-mates and friends for the continuous encouragement, intriguing discussions, moral support and for putting up with my bad jokes. Last but not the least, I would like to thank my family for the patience and for providing the strength to complete this work.

TABLE OF CONTENTS

LIST OF FIGURES

LIST OF TABLES

NOMENCLATURE

a	Radius of the helical tube, elastic modulus scaling factor
b	Line fit parameter for Stent authority
BMS	Bare metal stents
CA	Coronary Artery
DES	Drug eluting stents
Dn	Dean Number, $Dn = \mathrm{Re}_D \kappa^{0.5}$
E	Elastic modulus
$\sqrt{g}$	Jacobian of transformation
$\sqrt{g}U_g^j$	Contravariant Flux Vector due to grid movement
$\sqrt{g}U^j$	Contravariant Flux Vector
g^{ij}	Contravariant metric tensor
G	Shear Modulus
Gn	Germano Number, $Gn = \mathrm{Re}_D \tau$
F	Applied Force in FSI formulation
h	Height of the cylinder on which the helix rests, Wall thickness
L	Length of helical tube
k	Timoshenko shear correction factor
LCA	Left Coronary Artery
n	Normal Direction
P, p	Pressure
R	Radius of curvature of in plane curved tube, Reflection Coefficient
r	Radial coordinate in the helical coordinate system
RCA	Right Coronary Artery
Re	Reynolds number, $\mathrm{Re} = \dfrac{\rho\left(a^*\right)^2 \omega^*}{\mu}$
s	Axial coordinate in the helical coordinate system, Shear rate
SA	Stent Authority
T, t	Time, Biological age of the artery
TD	Helical tube diameter
u	Velocity component
v	Velocity component
WSS	Wall Shear Stress, $WSS = \dfrac{1}{\Omega^2}\left(\dfrac{\partial v_s}{\partial r}\right)$
x	Axial direction
Y	Flow Admittance
$\vec{x}$	Physical Spatial vector
α	Radius of the cylinder on which the helix rests, Sensitivity of uptake process to shear rate for intimal thickening
β	Pitch of the helix, Activation energy for the retardation process of intimal

	thickening
γ	Gamma Parameter, $\gamma = \frac{Gn}{Dn^{1.5}}$
δ	Transient boundary layer thickness, Intimal thickness
ϕ	Radial deformation in FSI formulation
ε	Deformation parameter
ϕ	Poisson's Ratio
θ	Circumferential direction in the helical coordinate system
κ	Curvature of helix, $\kappa = \frac{\alpha}{\alpha^2 + \beta^2}$
μ	Dynamic Viscosity
ν	Kinematic viscosity
$\vec{\xi}$	Computational Space vector
ρ	Density
τ	Torsion of helix, shear stress, $\tau = \frac{\beta}{\alpha^2 + \beta^2}$
ω	Angular Frequency, Vorticity
Ω	Womersley Number, $\Omega = \sqrt{\frac{\rho\omega^*}{\mu}} a^*$

Subscripts

avg	Time averaged values
f	Fluid values
in	Value at the inlet
n	Normal direction
out	Value at the outlet
r	Radial direction in the helical coordinate system
s	Axial direction in the helical coordinate system
w	Wall Values
θ	Circumferential direction in the helical coordinate system
begin	Beginning location of compliance discontinuity
trans	Transition length of compliance discontinuity
end	Ending location of compliance discontinuity
s	Stented
us	Unstented

Superscripts

$*$	Dimensional Values

1. Introduction

Motivation

Cardiovascular diseases (CVD) are the number one causes of death in the world. According to the World Health Organization (WHO) 17.3 million people died from cardiovascular disease in 2008, representing 30 % of all global deaths, with Coronary Artery Disease (CAD) being one of the major contributors, with 7.3 million deaths. Thus, there is a critical need to address existing and emerging challenges and develop novel tools to diagnose, monitor, and treat coronary artery diseases.

The hydrodynamics of pulsatile flows in flexible vessels with wall deformations and large dynamic changes in geometry such as that seen in coronary arteries are not well understood. These flow conditions exhibit fluid structure interactions (FSI), flow and structural instabilities and pressure wave reflections that affect flow patterns, induced stresses and transport processes. However, despite extensive previous work there is practically no research on the effect that compliance mismatch and stiffness discontinuities have on the hydrodynamics in realistic physiological conditions that include the effects of motion of the myocardium on the coronary artery. In particular, the prediction of in-vivo flow conditions in coronary arteries (CA) and the performance of prosthesis like stents under these conditions, that cause variation in local compliance are not understood. It is hypothesized that in coronary artery flows, the large scale motions of the myocardium along with local variations or discontinuities of the vessel stiffness alter the pressure gradients leading to non-physiological flow patterns and abnormal wall shear stresses. It is inferred that this combined mechanism can have significant hemodynamic effects. An attempt to investigate the effect of dynamic geometry variation and stiffness variation -as manifested in stented coronary arteries- on the character of the flow is made in this work. Coronary artery flows are complex and involve multiple mechanical and chemical interactions and stimuli. Although the role of dynamic variation of the geometry and stiffness variation is only one piece of the puzzle, yet it is the one that has arguably received the least attention. This can be primarily attributed to limitations of computational tools for properly resolving the inherent FSI problem. The proposed hypothesis is presented in Fig. 1.1

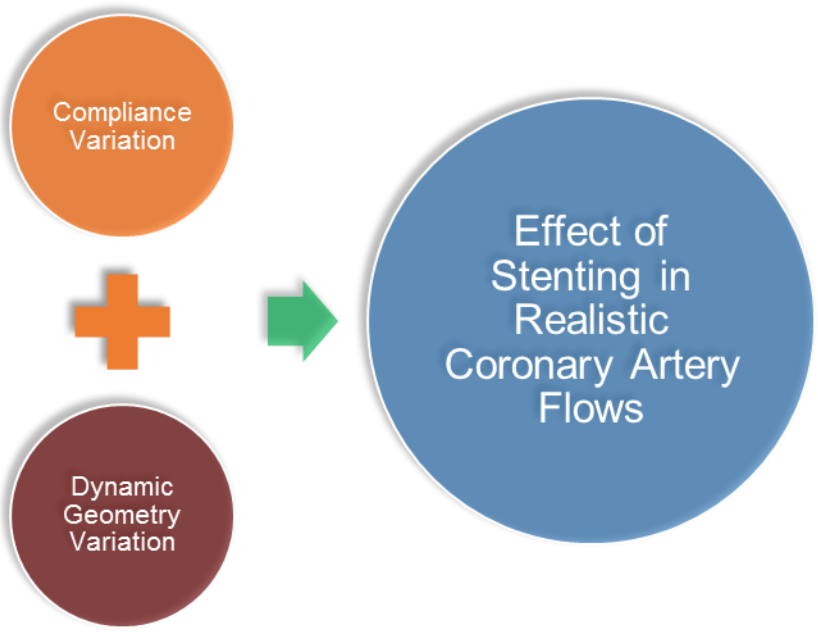

Figure 1.1 Integration of compliance variation and dynamic geometry variation to simulate realistic coronary artery flows

Objective

The main purpose of this work is to quantify the effect of the compliance change due to stenting in realistic coronary arteries, including the effects of the deformation of the artery under the influence of applied fluid forces (FSI) and the induced motion of the artery due to the motion of the myocardium itself. There has been considerable recent work to study the mechanical properties of stents by numerical analysis or in vitro mechanical tests, and to compare them by type or brand. However, these studies cannot yet predict their in vivo performance. This study will also try to quantify the effect of stent parameters: length, transition length and expansion area, on hemodynamics. This work would be helpful in the design of stents and aid in understanding the bio-fluid dynamic effects of stenting. The research objectives to this end are:

- Baseline study to establish the hypothesis of the effect of compliance mismatch on hemodynamics
    - This objective provides the basis for the hypothesis that the compliance mismatch would affect the local hemodynamics, leading to the change in WSS and OSI near the discontinuities in compliance.

- Characterize the flow due to dynamic motion of a generalized CA
    - This objective will characterize the effects of curvature and torsion on the hemodynamics, including the dynamics of the change in curvature and torsion with time, forming the basis for studying the effect of the compliance mismatch under realistic conditions. This work will help us in isolating the effect of curvature and torsion on flow.
- Study the effect of compliance change due to stenting of a generalized CA
    - This objective will characterize the effects of compliance mismatch on the hemodynamics under in-vivo conditions, including the dynamics of the change in curvature and torsion with time. To the best of our knowledge, this the first study of its kind.
- Study the effect of stent deployment strategies due to stenting in a generalized CA
    - This objective will try to answer critical clinical questions with regard to the effect of stent deployment strategies on local hemodynamics.

Coronary Arteries in Brief

The coronary arteries are the vessels that supply blood to the heart itself, originating at the aortic sinuses. The heart consists of four chambers, two ventricles and two atria, which contract and expand in tandem in a rhythmic fashion. The blood from the left ventricle is carried by the aorta to the whole body and returns back to the right atrium. This is called the systemic circulation. The blood from the right ventricle flows to the lungs and returns back with oxygen to the left atrium, forming the pulmonary circulation. The systemic circulation is at a higher pressure due to the need to reach all extremities of the body, thus the work done by the left side of the heart is higher compared to the right side. This is reflected by the presence of a more extensive coronary network on the left side of the heart. There are two main arteries that supply blood to the heart, the left main coronary artery (LCA) and the right coronary artery (RCA). The LCA further branches out into the left anterior descending (LAD) and the Left circumflex (LCX) arteries. The arteries themselves are supported and connected to the myocardium and thus are affected by the movement of the heart. It should also be noted that the coronary arteries themselves deform and are compliant.

Contributions of this Work

The main scientific and engineering contributions of this work is the development of a general framework to simulate close-to-real mechanical conditions that is experienced by flow in a coronary artery. This was done by conceptualizing the artery as a helical tube resting on a beating cylindrical heart. The large scale three-dimensional motion with physiologically relevant pulsatile flow conditions through compliant arteries provided a rich and physically relevant environment for investigating the impact of stents placed in the vessel. To our knowledge, this is the first study to include all these effects in a coherent framework allowing for a meaningful quantitative assessment of the effect of different parameters on hemodynamics. Effects of stent compliance mismatch, stent length, stent overexpansion, and stent transition length are investigated under the influence of changing curvature and torsion imposed by the motion of the beating heart.

The following journal articles were written during the course of this work and are an integral part of this dissertation:

- "Hydrodynamic Effects of Compliance Mismatch in Stented Arteries", Selvarasu NKC, Tafti DK, Vlachos PP, ASME JBME, Volume 133, Issue: 2, FEB 2011

- "Investigation of the Effects of Dynamic Change in Curvature and Torsion on Pulsatile Flow in a Helical Tube", Selvarasu NKC and Tafti DK, ASME JBME, Volume 134, Issue: 7, JUL 2012

- "Effects of Compliance Mismatch in Elastic Helical Under the Influence of Dynamic Changes in Curvature and Torsion", Selvarasu NKC and Tafti DK, ***Submitted***

- "Effects of Stent Length, Transition Length and Overexpansion in Stented Arteries", Selvarasu NKC and Tafti DK, ***To be Submitted***

- "Effect of Pin Density on Heat -Mass Transfer and Fluid Flow at Low Reynolds Numbers in Minichannels", N.K.C. Selvarasu, D. Tafti, N.E. Blackwell, ASME Journal of Heat Transfer, Journal of Heat Transfer, Vol. 132

- “Implementing modular adaptation of scientific software”, Pilsung Kang, N.K.C. Selvarasu, Naren Ramakrishnan, Calvin J. Ribbens, Danesh K. Tafti, Yang Cao, Srinidhi Varadarajan, , Journal of Computational Science, Volume 3, Issues 1–2

Organization of Thesis

The rest of the manuscript is organized as follows. The second chapter presents a brief review of the relevant literature. Chapter 3 presents the methods used to tackle the problem at hand. Chapter 4 presents the results supporting the hypothesis that compliance changes affect the hemodynamics. To this end a straight compliant tube with no applied motion was used. Chapter 5 presents the results providing the flow characteristics for non-compliant helical tubes subject to realistic myocardial motion. Chapter 6 presents the results of compliant helical tubes subject to both changes in compliance and myocardial motion. Chapter 7 presents the effects of three stent parameters – length, transition length and deployment overexpansion area. Chapter 8 presents a comparison of the flow in a straight non-moving vs. a moving stented artery. Finally Conclusions and Summary of this work are presented in Chapter 9.

2. Literature Review

The relationship of arterial tissue and fluid mechanics to cardiovascular disease has been in the forefront of research for many years[1, 2]. A thorough review on the topic is beyond the scope of this thesis. However, the strong relationship between the fluid mechanics of the vessels and the mechanisms associated with atherosclerosis and thrombosis is well documented. Particularly, the significance of wall shear stresses in arterial flow and their role in the development of disease has been the topic of numerous studies [3, 4]. The literature that is relevant to this work consists of works concerned with dynamic changes in geometry, compliance variation and various deployment strategies. Presented below is some of the literature relevant to this work. This chapter is organized as follows. First we present the literature that is of relevance to dynamic change in geometry, followed by the literature of relevance to compliance variation. Finally we present the literature that is of relevance to the various stent deployment strategies.

Dynamic Change in Geometry of the Coronary Artery

The effect of the dynamic change in curvature and torsion under pulsatile flow conditions on local hemodynamics is not fully understood. In this work, we focus our investigation on the localized hemodynamic effects of dynamic changes in curvature and torsion. It is our objective to understand and reveal the mechanism by which changes in curvature and torsion contribute towards observed wall shear stress distribution. The literature that is relevant to the problem studied in this work can be grouped into three classes – study of flow in stationary helical tubes, study of the effect of motion on flow under simplified conditions with applied 2D motion, and studies that are based on patient specific geometries and observed motion at discrete times of the cardiac cycle. A brief summary of all three classes of work will be presented in the below paragraphs.

Flow in Stationary Helical Tubes

There is extensive research, both numerical and theoretical, on flow in static helical tubes with circular cross section, focusing on secondary transport. Wang [5] studied flow in a tube with small curvature and at low Reynolds number and found that the recirculating zones drop from two to one when the Reynolds number is reduced.

Germano [6] developed a orthogonal helical coordinate system to analyze helical tube flow. Kao [7] used the coordinate system developed by Germano[6] and obtained secondary flow patterns for different torsion values. It was shown in the above work that as the torsion increases, the two-cell vortex structure changes, with one vortex structure dominating the other. Yamamoto et al. [8] investigated high Dean number flows in a tube with large curvature and torsion, providing vector plots of the secondary flows. They saw a dominant vortex develop with increase in Reynolds number. An extensive review on flow in curved tubes was provided by Berger et al. [9]. Gammak and Hydon [10] studied steady and unsteady flows in pipes with small, slowly varying curvature and torsion. They found that the azimuthal WSS increased by the introduction of torsion. For a uniform pipe, the introduction of torsion breaks the symmetric structure (of flow without torsion) and skews the velocity profiles in the direction of the torsion. They concluded that as curvature increases, the axial velocity is forced towards the outer wall and the secondary velocity field is increased in strength. Increasing torsion skews the components of velocity in the direction of increasing torsion. Peterson and Plesniak [11] presented the results of an experimental investigation to determine the influence of two physiologically relevant inlet conditions on the flow physics downstream of an idealized stenosis are presented. The mean, maximum and minimum Reynolds numbers of 364, 1424 and 24, respectively, and a Womersley number of 4.6 was studied. Curvature-induced secondary flow was found to play a minor role in the near-stenosis region. Vortex ring formation was relatively unaffected by the mean velocity gradient and secondary flow.

Flow in Moving Tubes

The works listed above are just a few from the extensive literature on the flow in fixed static helical tubes. Comparatively, the number of works studying the dynamic effects of change in curvature and torsion is limited. Moore et al. [12] studied the effect of axial movement on a straight tube, with the applied movement obtained from coronary angiography. It was found that the movement affects the shear stress oscillation. Santamarina et al. [13] studied the effects of varying curvature on flow through a circularly curved tube. They observed that the wall shear rate for the dynamic case was within 6% of the static case. As an extension of the above work, the effect of frequency

of curvature change was studied by Moore et al. [14]. It was concluded that the dynamic curvature change frequency affected the inner wall shear rates in coronary arteries.

Patient Specific Studies

The third class of work found in the literature is based on patient specific geometries. A model of the bifurcation of the left anterior descending coronary artery and its first diagonal branch was studied by Prose et al. [15]. The influence of curvature was found to increase downstream of the branch. Zeng et al. [16] studied one right coronary artery (RCA) using the geometry and motion from biplane cine-angiograms incorporating observed bending and torsion. The instantaneous WSS values varied by 150% in the dynamic case compared to static case. Little difference was seen in the time averaged WSS between the static and dynamic cases, with the pulsatile effects dominating the flow. Theodora Kakos et al. [17] studied the flow in a left anterior descending (LAD) artery with the motion and geometry obtained from x-ray angiograms. They observed that the motion of the artery damped the recirculation zones formed, compared to a steady static case. Torii et al. [18] studied an RCA based on observed MR images and observed that OSI was affected to a greater extent than the WSS due to the applied motion.

Variability of Coronary Artery Geometry and Motion

All the above conclusions were based on the study of one patient specific artery and thus are limited. The variability of CA geometry and its motion is quite extensive between individuals. Ding et al [19-21] studied coronary artery dynamics by tracking motion of the arteries in-vivo. They observed that there was variation in the motion between individuals and between different vessels themselves in one person. This led them to hypothesize that the variability of motion affects the susceptibility of vessels to atherosclerosis between the patients and between the vessels. There is also wide variability in the anatomical layout and the geometry of coronary artery (CA) between patients. Brinkman et al. [22] studied 30 autopsy hearts to find the geometric distribution of the left coronary artery(LCA). Based on measured geometric parameters, they found no correlation between the 30 hearts studied, with the parameters varying considerably. Zhu et al. [21] studied the geometry of 32 left anterior descending (LAD) arteries and 35

right coronary arteries from angiographic images. They too found major variations in geometry, with 80% of this variation being explainable in terms of the curvature and torsion change. The variation of the curvature about the mean was 25% and the variation of the torsion was 65% for the LAD. The geometry of the CA affects the local hemodynamics and shear stresses as evident from specific sites being prone to atherosclerosis. This leads to the conclusion that measured/calculated hemodynamics would change drastically from one individual to another.

Need for Studying the Effect of Dynamic Change in Geometry

In summary, the literature is limited with regards to the dynamic effects of motion on flow, especially of curvature and torsion, as are experienced by coronary arteries. From the extensive studies on flow in stationary helices, it is known that the flow patterns are affected by curvature and torsion. From the studies of simple 2D applied motion, it is known that the WSS is affected by the dynamic changes in geometry [12-14]. Patient specific models do not help draw general conclusions, due to the fact that the variations in geometry and motion observed are drastic between patients. Hence to draw general conclusions, a generalized geometry is needed, both to study the effect of the shape and the displacement of the CA due to the myocardium. Also, the effect of dynamic curvature and torsion change on flow patterns in a CA has not been studied in detail.

Thus, one of the objective of this work is to study the effect of the dynamic change in curvature and torsion on flow in an idealized helical coronary artery resting on a cylindrical myocardium.

Effect of Compliance Variation on Arterial Flow

The most common treatment modality for occlusive cardiovascular disease is the use of stents. Although existing stents perform their function of supporting diseased arterial tissue, stent design profoundly influences the post-procedural hemodynamic and solid mechanical environment of the stented artery [23-25].

Stone et al.[26] showed that regions of low wall shear stress had higher accumulation of atherosclerotic plaque accompanied with increase in external wall radius showing a positive wall remodeling. They also note that within the stented region there is intimal

thickening, causing a reduction of lumen and an increase in fluid velocity and wall shear stress. It was observed that the neointimal thickness was inversely proportional to the WSS, suggesting a hemodynamic contribution to restenosis. Pache et al. [27] studied the effect of stent strut thickness on restenosis during the ISAR-STEREO-2 Trial, by observing the effect of different type of stents on restenosis in 611 patients with CAD. The rate of restenosis was 17.9% in the thin stent group and 31.4% in the thick stent group, mainly through late lumen loss. Studies on coronary artery bypass grafts provide contrasting results as to the contribution of the magnitude of the wall shear stress on hyperplasia or the role of the WSS gradient [28-30]. Also studies have shown that the graft success rate is increased by reducing the compliance mismatch between the host native artery and the graft [31, 32].

Charonko et al. [33] developed a one-dimensional finite-difference model to predict pressure wave reflections in stented arteries, and a parametric study of variations in stent and vessel properties was performed, including: stent stiffness, length, and compliance transition region, as well as vessel radius and wall thickness. Charonko et al. also studied the effect of stent design [34] and stent implantation configuration [35] using time resolved Digital Particle Image Velocimetry (DPIV), where changes in stent design affected the WSS on the wall. Data from CFD models by LaDisa et al. [36-39] suggest that stent geometry may cause local alterations in WSS, which have been associated with neo-intimal hyperplasia and subsequent restenosis. The result obtained using three-dimensional CFD models suggest that changes in vascular geometry after stent implantation are important determinants of WSS distributions that may be associated with subsequent neo-intimal hyperplasia. However, the models used here do not consider the fluid-structure interactions. Berry et al. [40] carried out a similar study, using flow visualization studies and CFD. All such studies have presented the micro-scale effects of stenting before the wires have been covered with the surrounding tissue. These studies do not pertain to long term stent effects, but to the hemodynamics just after stent implantation. This is significant because observations made in stented arteries in animal studies have indicated a continuous growth of endothelial cells. Yazdani et al. [41] performed DPIV measurements to find the effect of compliance mismatch due to stenting . They found that large compliance mismatch increased the size and the

residence time of the near wall vortex, indicating that the compliance of the stent plays a significant role in post-stent hemodynamics. Thus one of the objectives of this work was to characterize the effect of compliance change, to find the effect of late restenosis.

Effect of Stent Length, Transition Length and Overexpansion

Numerous risk factors have been identified as the cause of stent failure. These predictors can be classified as clinical, procedural, or lesion related. This work is predominantly concerned with the procedural causes of stent failure. Presented below is some of the literature relevant to this work.

Stent Length Effects

Stent placement approaches vary from covering just the zone of maximal obstruction to stenting well beyond the lesion boundaries. Mauri et al.[42] studied the effects of stent length and lesion length on coronary restenosis. They analyzed the angiographic follow-up of 1,181 patients. Stent length exceeded lesion length in 87% of lesions. They found that stent length increased the risk of restenosis independent of the stented lesion length. Kereiakes et al.[43] demonstrated the relative importance of stent length, independent of post-procedural minimal lumen diameter as a key predictor of subsequent in-stent restenosis. They concluded that longer stented segment length correlates with late restenosis. Longer stent length was associated with an increased frequency of late in-stent restenosis. Kobayashi et al.[44] evaluated the relation between stented segment length and restenosis in 725 patients with 1,090 lesions. They found that the minimal lumen diameter was lower when the stent length increased. Restenosis rates were 47% for the long stent group compared to the short stent group (24%). Moreno et al.[45] compared the risk of stent thrombosis after drug-eluting stents (DES) versus bare-metal stents (BMS) and tested the hypothesis that the risk of DES thrombosis is related to stent length. The risk of thrombosis after DES versus BMS was compared, and the relationship between the rate of DES thrombosis and stent length was evaluated. They concluded that the risk of stent thrombosis after DES implantation is related to stent length. Charonko et al[33] studied the effect of various stent parameters on the pressure wave reflections. The parameters studied included the stiffness ratio, stent length and

stent transition length. They found that increasing or decreasing the stent length by amounts up to 50% resulted in an equal change in the percentage of wave reflection. The magnitude of the reflected pressure wave was found to vary linearly with length of the stent being tested.

Stent Transition Length Effects

Berry et al.[46] used finite element analysis to assess the solid mechanical behavior in a stent/artery hybrid structure for a gradual transition of compliance mismatch compared to a baseline stent (Palmaz Stent). In vivo hemodynamics and wall mechanical changes induced by the gradual change in compliance were investigated in a swine model from direct measurements of flow, pressure, diameter, and histology in the stented segment of superficial femoral arteries after 7 days. They found that circumferential stress was also markedly reduced when compliance was changed gradually, compared to Palmaz stent. Charonko et al[33] studied the effect of the transition length effects on pressure wave reflections using a simplified 1D analysis and found that changing the transition length had a relatively small effect on the reflections. Doubling the stiffness transition length to simulate a compliance-matching stent as in Barry et al.[46] led to only a 4.3% decrease in reflections. They concluded that the size of the reflection is relatively unaffected by the transition zone length, and a design that maintains a constant rigidity from end to end will cause only minor changes in pressure effects.

Stent Overexpansion Effects

Stent restenosis in BMS and late thrombosis in DES were shown to be caused by stent under-expansion. Alfonso et al.[47] found that under-expansion was the cause of stent failure in 58% of DES cases and 33% of BMS cases. Romagnoli et al.[48] also stated that suboptimal or incomplete stent expansion is associated with increased restenosis and target vessel revascularization rates and, especially with drug-eluting stents (DES), might also predispose these stents to thrombosis. They highlighted the importance of adequate high-pressure post-dilation to obtain optimal stent expansion to positively affect stent thrombosis and restenosis. From these studies, it was generally

concluded that the artery needs to be over-expanded during stent deployment. A 10% cross-sectional area overexpansion is recommended.

However, based on clinical observations, Hoffmann et al.[49] showed that a more aggressive stent implantation technique is associated with an increase in neointimal hyperplasia. They concluded that tissue proliferation inside and surrounding stents may be related to aggressiveness of the stent implantation technique. Russo et al.[50] studied the effect of increasing balloon-to-artery ratio on neointimal hyperplasia following primary stent placement using a non-atherosclerotic porcine coronary overstretch model to determine if an aggressive approach to coronary revascularisation with oversized balloons is counterproductive. In the porcine models studied, Russo et al.[50] concluded that vessel overexpansion is counterproductive. It should be noted that this study was conducted in young disease free arteries.

Relevance to Hemodynamics

The vascular endothelium shows a variety of responses to local flow conditions. The endothelial cells align with the direction of flow, activate ion channels, and organize internal cytoskeletal structures, to name a few. Certain regions of the arterial wall normally undergo structural remodeling that is characterized by intimal thickening which is hypothesized to represent localized responses to high mechanical forces and shear stress conditions to which these regions are subjected [51]. This is indicative of a biological response of the arterial tissue to local hemodynamic conditions [52-54]. Thus the local shear stress conditions and hemodynamics would affect the endothelial response and thus would lead to neointimal hyperplasia.

Summary

In summary, the influence of the dynamic change in curvature and torsion is shown to influence the local hemodynamics[55] and needs to be considered to accurately predict in-vivo flow conditions in coronary arteries and the performance of prosthesis like stents under these conditions. Thus, the objective of this work is to study the effect of variation of compliance under the influence of dynamic change in curvature and torsion on flow in an idealized helical coronary artery resting on a cylindrical myocardium. It will be

demonstrated that the movement of the artery due to the movement of the myocardium cannot be ignored and needs to be considered to accurately predict the effects of compliance discontinuities such as would be caused by stents in coronary arteries.

In this work, based on the above literature, it is hypothesized that the stent-artery compliance mismatch affects the local hemodynamics, triggering the physiological response of the endothelium, which in turn leads to the formation of neointimal hyperplasia. We investigate the effect of the variation of compliance in stented arteries on the character of the flow and on the near wall hemodynamics.

From the above literature, the effect of various stent deployment strategies becomes apparent. We can conclude that the stent length plays a significant role in determining the post stent clinical outcomes. Thus one of the objects of this work was to look at the detailed fluid dynamics effects of stent length and identify its contributions to abnormal hemodynamics, in a curved artery subject to dynamic changes in geometry. Another object of the current work was to study the effect of transition length and check the hypothesis by Berry et al.[46]. Finally, the effects of the overexpansion of the artery during the placement of the stent will also be studied under the influence of the applied motion.

3. Governing Equations and Methods

Introduction

In order to study the effect of stenting in coronary artery, we need to consider the applied motion due to the motion of the myocardium and also the fluid-structure interaction due to the elastic nature of the arterial walls. The methods used and developed to this end, are discussed in this chapter. The organization of the chapter is as follows. First the overall algorithm and flow chart is presented and then each component of the algorithm is explained in detail.

Algorithm Used in this Work

Fig. 3.1 shows the flow chart of the algorithm used to solve the Fluid-Structure Interaction (FSI) and applied motion problem that needs to be solved for flows in coronary arteries. The overall steps involved are:

1. The initial grid and the initial and boundary conditions are read in. The flow and structural variables are initialized and the time loop is entered to advance the solution in time. Steps 2 through 9 are calculated inside the time loop till the number of time steps required for the specified cycles are completed.
2. The time dependent pulsatile inlet velocity and outlet pressure is applied for that time step. The details of the applied pulsatile boundary conditions are provided in detail in Chapters 4, 5 and 6.
3. The FSI model equation is solved to obtain the deformations at the deforming walls.
4. Transfinite interpolation is applied to transmit the deformations at the walls to the internal grid points and the internal blocks of the multi-block topology.
5. The current and previous volume of the cylindrical heart on which the helical artery rests is calculated based on the applied volume change.
6. The properties of the centerline of the helical artery, namely its coordinates, tangential, normal and binormal vectors are calculated at the current and previous time steps.

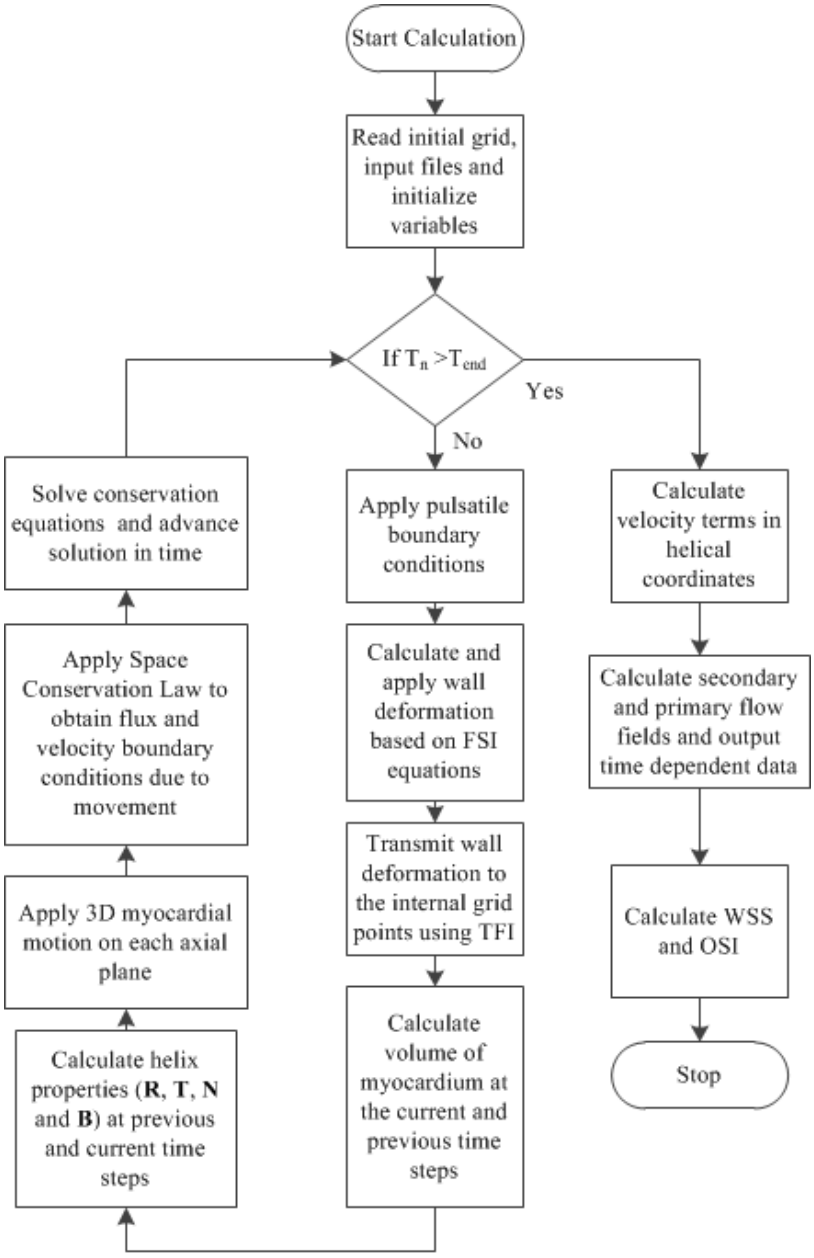

Figure 3.1 Algorithm used to model wall deformations due to FSI and the 3D motion due to the motion of the myocardium in this thesis

7. Based on the above properties, the 3D translation and rotation of each axial plane is calculated and applied.
8. The space conservation law is applied to obtain the movement fluxes and velocities that go into the momentum equation.
9. The conservation equations are solved and the solution is advanced in time.

10. Steps 2 through 9 are repeated till the number of time steps required for the specified cycles are completed.
11. The time dependent flow fields in helical coordinates are calculated and the time averaged wall shear stresses (WSS) is calculated.

The details of the above steps are provided in the following sections, in the order they are invoked in the in-house code GenIDLEST.

Calculation of the Wall Deformations - Fluid Structure Interaction

After the application of the pulsatile boundary conditions, the next step in the algorithm is the calculation of the deformations at the arterial wall. The induced motion (FSI) of the arterial wall under the influence of the fluid forces is solved based on a cylindrical membrane model [56, 57]. The equations shown below pertain to these models.

$$\frac{\partial^2 \phi}{\partial t^2} + \frac{E}{\left(1-\sigma^2\right)R^2}\phi + \frac{C_v}{R^2}\frac{\partial \phi}{\partial t} = \frac{F}{h} \qquad \textbf{3.1}$$

$$\frac{\partial^2 \phi}{\partial t^2} + \frac{E}{\left(1-\sigma^2\right)R^2}\phi - kG\frac{\partial^2 \phi}{\partial x^2} = \frac{F}{h} \qquad \textbf{3.2}$$

Eq. (3.1) was used to study the effect of compliance mismatch in a straight tube and Eq. (3.2) was used to study the compliance mismatch effects in helical tubes. In Eqs. (3.1-3.2), it is assumed that the arterial wall is a thin linear membrane shell and that the wall is loaded in the radial direction, with zero longitudinal displacement and the ratio of the wall material density to the fluid density is one. Here ϕ is the radial displacement, R is the un-deformed radius of the vessel, C_v is the visco-elastic constant, E is the elastic modulus, σ is the Poisson's ratio, h is the wall thickness, G is the shear modulus, k is the Timoshenko shear correction factor [58], and F is the applied radial external force component acting on the shell. The elastic modulus E is non-dimensionalized using the pressure scale $\rho\left(a^*\omega^*\right)^2$, the viscoelastic coefficient is non-dimensionalized using the characteristic scale $\rho\left(a^*\right)^2\omega^*$, the displacement ϕ, the un-deformed radius R of the vessel and the vessel thickness h are non-dimensionalized using the un-deformed radius

at the inlet a^*. The time is non-dimensionalized using the characteristic time scale $1/\omega^*$. Eqs. (3.1) or Eq. (3.2) is solved implicitly and is coupled to the fluid solution using the pressure at the wall as the external force component. The vessel wall is assumed to be stationary initially and the ends of the vessel wall are assumed to have zero deformation (tethered) at all times.

Transfinite Interpolation

A key ingredient of the algorithm to account for moving boundaries is the implementation of a dynamic mesh that responds to structural movement at the boundaries. This is carried out using an ALE approach. After finding the deformation the of walls, one-, two- and three-dimensional TFI is carried out to transmit the edge deformation into the volume grid. One-dimensional TFI is first applied to each edge, for example for an edge (low west edge) it is given by

$$\Delta\overrightarrow{x_{i,1,1}} = \left(1-\alpha_{i,1,1}\right)\Delta\overrightarrow{x_{1,1,1}} + \alpha_{i,1,1}\Delta\overrightarrow{x_{i\max,1,1}} \qquad \textbf{3.3}$$

where α is the control function that preserves the initial grid distribution and is computed for a given direction as

$$\alpha_{i,1,1} = {s_{i,1,1}}/{s_{i\max,1,1}} \qquad \textbf{3.4}$$

Here s is the arc length that is computed as

$$s_{i,j,k} = s_{i-1,j,k} + \sqrt{\left(x_{i,j,k}-x_{i-1,j,k}\right)^2 + \left(y_{i,j,k}-y_{i-1,j,k}\right)^2 + \left(z_{i,j,k}-z_{i-1,j,k}\right)^2} \qquad \textbf{3.5}$$

Following the edge interpolation, the surfaces and volumes are interpolated. The details of the approach is available in Gopalakrishnan et al [59], along with various studies used to validate the moving grid methodologies implemented in the code. Based on the requirements of the current study, the ALE method is well suited. This technique has also been applied successfully to simulate flapping flight with application to micro-air vehicles and to study compliance effects in coronary arteries [55, 59-61].

Cylindrical Heart Volume Change and Properties of Helical Artery Centerline

To study the effect of dynamic change in arterial geometry due to myocardial motion, a simplified coronary artery resting on a cylindrical heart is modeled. The

maximum height and radius of the heart was set to 0.09m and 0.03m respectively, with the radius of the helical tube being 0.0015m. The heart rate was set to 60 beats/min. The time varying contraction and expansion of this mock heart is modeled as a cosine function for the initial study (Chapter 5). For the subsequent studies the volume change is modeled as shown in Fig. 3.2. Once the volume is obtained for a given time instant, the height and radius of the cylinder is known, by assuming that the ratio of cylinder height and radius remain the same through the cardiac cycle, in this study 3.

$$V_{cyl} = \pi r_{cyl}^2 h_{cyl} = 3\pi r_{cyl}^3 \quad \textbf{3.6}$$

From the height and radius of the cylinder, the properties of the helical artery can be computed as explained in the paragraphs below. A helix can be completely defined using its curvature and torsion, as defined in Eqs (3.7-3.8) below.

$$\kappa = \frac{\alpha}{\alpha^2 + \beta^2} \quad \textbf{3.7}$$

$$\tau = \frac{\beta}{\alpha^2 + \beta^2} \quad \textbf{3.8}$$

In Eqs (3.7-3.8) ‘α’ is the radius of the cylinder on which the helix rests and ‘β’ is the circumferential raise of the helix (if ‘h’ is the height of the cylinder, then $\pi\beta = h$). In order to understand the physical meaning of curvature and torsion, consider a rectangular sheet, with height h and a width of $2\pi\alpha$. Consider three lines drawn on this surface – a horizontal line drawn end to end at an arbitrary height, a vertical line drawn end to end at an arbitrary horizontal position and a diagonal of the rectangle. If the sheet is rolled into a cylinder by joining the vertical edges, the vertical line will still be vertical and is analogous to a helix that has only torsion, with a value of $1/\beta$. The horizontal line will be from a circle, whose curvature is $1/\alpha$. The diagonal would form a helix with the curvature and torsion as defined in Eqs. (3.7) and (3.8). These three lines form the limiting cases for curvature and torsion for a given cylinder.

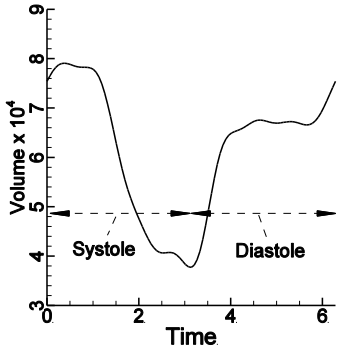

Figure 3.2 Variation of the volume of the cylinder with time

As stated above, the coronary artery is modeled as a helical tube. Thus it becomes important to define the properties of a helix and the helical coordinate system that arises from such a definition. In helical coordinates, *s* is the axial coordinate (arc length), θ is the angular coordinate and *r* is the radial position with respect to the helical curve representing the center. For all the results presented in this work, *s* varies from 0 to π (half a helix), θ varies from –π to +π and *r* varies from 0 to 1. In the current framework, the origin of the coordinate system is located at the center of the lower face of the cylindrical heart as shown in Fig. 3.3. In the current study, the centerline helical curve position vector *R* is defined as

$$\overrightarrow{R(s)} = \alpha\cos(s)\,x + \alpha\sin(s)\,y + \beta s\hat{z} \qquad \textbf{3.9}$$

Thus the coordinate of the centerline at s = 0, π/2 and π are R(α, 0 ,0), R(0,α,h/2) and R(-α, 0, h/2) respectively as shown in Fig. 3.3. The tangential, normal and binormal vectors of the helical centerline are define as shown below.

$$\begin{aligned}\overrightarrow{T(s)} &= \frac{1}{\sqrt{\alpha^2+\beta^2}}\frac{d\vec{R}}{ds}\\ \overrightarrow{N(s)} &= \frac{d\vec{T}}{ds}\\ \overrightarrow{B(s)} &= \overrightarrow{T(s)}\times\overrightarrow{N(s)}\end{aligned} \qquad \textbf{3.10}$$

Using the centerline coordinate, tangent, normal and binormal, we can define any point in this coordinate system as shown in Eq. (3.11)

$$\vec{x} = \overrightarrow{R(s)} + r\cos\theta\overrightarrow{N(s)} + r\sin\theta\overrightarrow{B(s)} \qquad \textbf{3.11}$$

Eq. (3.11) is used to define the grid of the helical tube at any given instance of the cardiac cycle and helical coordinate position.

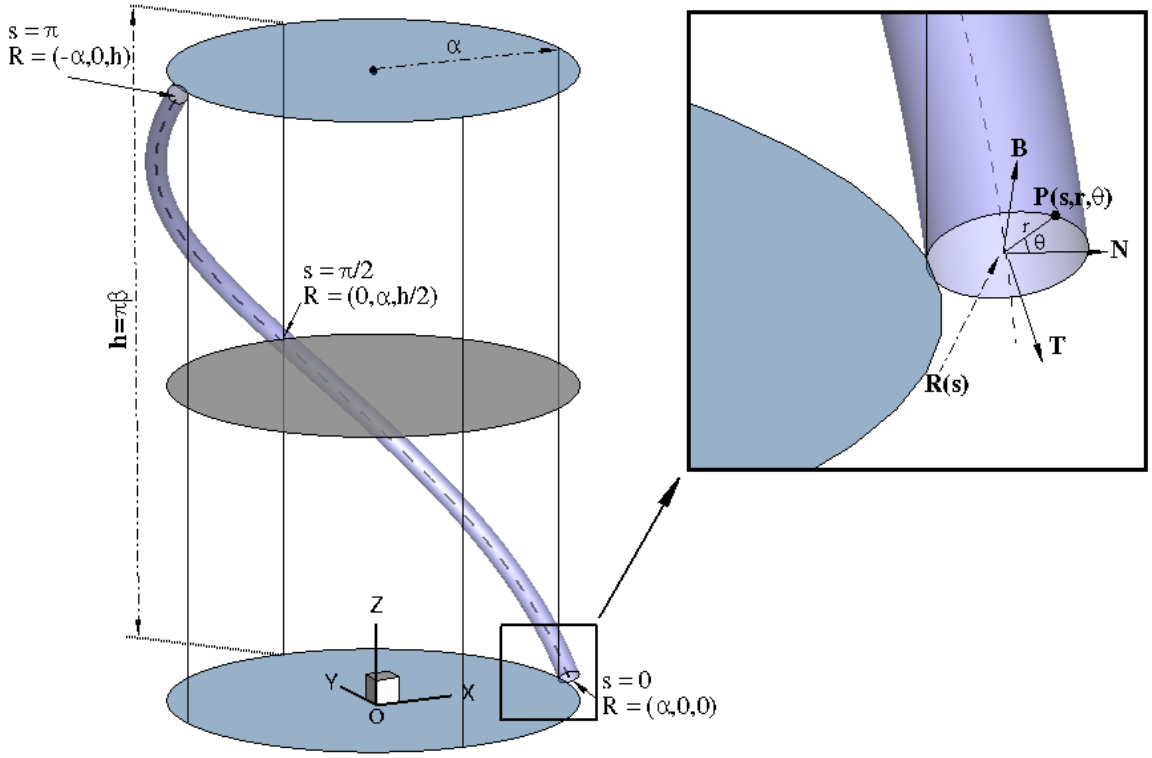

Figure 3.3 Helical Coordinate system used in the current work

Application of 3D Motion of the Helical Tube Due to the Myocardium

Once the properties of the helical centerline of the artery are known at the previous and current time step, the next step is to transform the grid points based on the cylinder volume change. Points on each *s* plane at a given instant in time needs to be transformed to the new *s* plane at the next time instance as is shown in Fig. 3.4. This is done in the following steps.

1. The properties of the helical centerline (*R, T, N* and *B* as defined in Eqs (3.9-3.10) are computed at the previous time step and the current time step
2. The translational movement is computed as the algebraic difference between the current and previous helical position R, as shown in Eq. (3.12)

$$\overrightarrow{x_{trans}} = \vec{x} + \overrightarrow{R^n} - \overrightarrow{R^{n-1}} \qquad \textbf{3.12}$$

3. The intersection vector ($\vec{v}$) between the *s* plane at the current time step and the *s* plane at the previous time step is computed as the normalized vector cross product of the tangent vectors (T) at the two time steps. This vector is the vector about which the points on the previous *s* plane will be rotated
4. The angle (φ) between the two planes is computed. If this angle is less than 10^{-9}, pure translation is assumed and the new position of the points on s plane are set to the translated coordinates as shown in Eq. (3.12)
5. If the angle between the planes is greater than 10^{-9}, the translated points $\overrightarrow{x_{trans}}$ are rotated about the new centerline R_n as shown below, where v_x, v_y and v_z are the components of the intersection vector.

$$\overrightarrow{x_n} = \begin{bmatrix} \left\{R_x^n\left(v_y^2+v_z^2\right)-v_x\left(R_y^n v_y+R_z^n v_z-v_x x_{trams,x}-v_y x_{trams,y}-v_z x_{trams,z}\right)\right\}\left(1-\cos\varphi\right)+ \\ x_{trams,x}\cos\varphi+\left\{-R_z^n v_y+R_y^n v_z-v_z x_{trams,y}+v_y x_{trams,z}\right\}\sin\varphi \\ \left\{R_y^n\left(v_x^2+v_z^2\right)-v_y\left(R_x^n v_x+R_z^n v_z-v_x x_{trams,x}-v_y x_{trams,y}-v_z x_{trams,z}\right)\right\}\left(1-\cos\varphi\right)+ \\ x_{trams,y}\cos\varphi+\left\{-R_x^n v_z+R_z^n v_x-v_x x_{trams,z}+v_z x_{trams,x}\right\}\sin\varphi \\ \left\{R_z^n\left(v_y^2+v_x^2\right)-v_z\left(R_y^n v_y+R_x^n v_x-v_x x_{trams,x}-v_y x_{trams,y}-v_z x_{trams,z}\right)\right\}\left(1-\cos\varphi\right)+ \\ x_{trams,z}\cos\varphi+\left\{-R_y^n v_x+R_x^n v_y-v_y x_{trams,x}+v_x x_{trams,y}\right\}\sin\varphi \end{bmatrix} \quad \textbf{3.13}$$

6. The above steps are repeated for all time steps

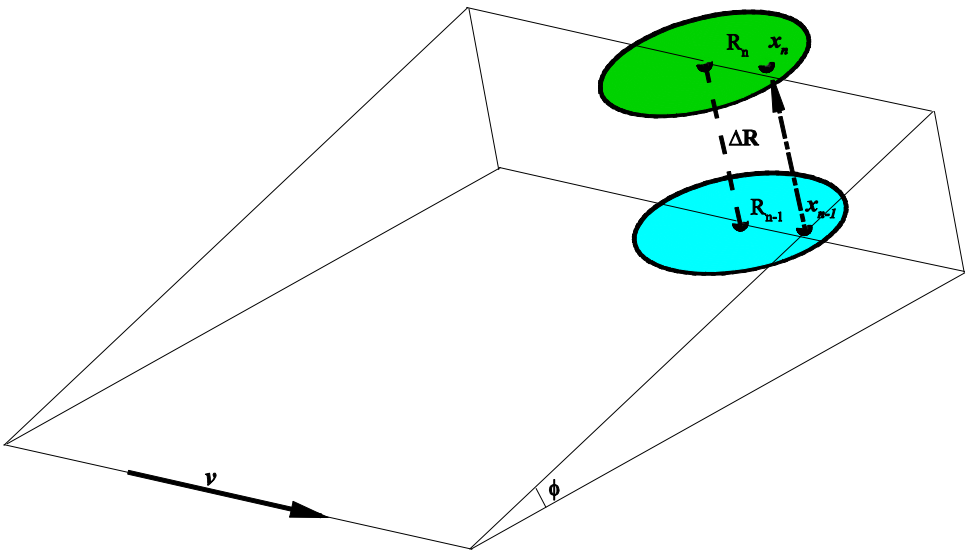

Figure 3.4 Rotation of a point from s-plane at time level n-1 to s-plane at time level n

Space Conservation Law

Once the new grid is obtained, the next step is the calculation of new grid metrics. This is followed by the application of the space conservation law (SCL) to obtain the movement fluxes and velocities. The satisfaction of SCL condition is explained by using a two-dimensional control area as shown in Fig. 3.4. The dotted and solid lines represent the cell faces at time level n and n+1, respectively. The shaded area represents the area swept by the east face. The swept volume is calculated for the 2D case based on a triangularization method as shown below.

$$\partial V = \frac{1}{2}\left(\overrightarrow{x_{00-10}} \times \overrightarrow{x_{00-11}}\right) + \frac{1}{2}\left(\overrightarrow{x_{00-11}} \times \overrightarrow{x_{00-01}}\right) \qquad \textbf{3.14}$$

The grid movement flux is obtained as shown below.

$$\sqrt{g}U_g^p = \frac{\partial V^p}{dt} \qquad \textbf{3.15}$$

For three-dimensional control volume, the satisfaction of SCL is an extension to the method described above, where the volume swept by the faces is used to find the fluxes. Now the three-dimensional volume is computed by dividing the cell into 24 tetrahedrons by connecting the cell center point to the vertices and to the centers of cell faces.

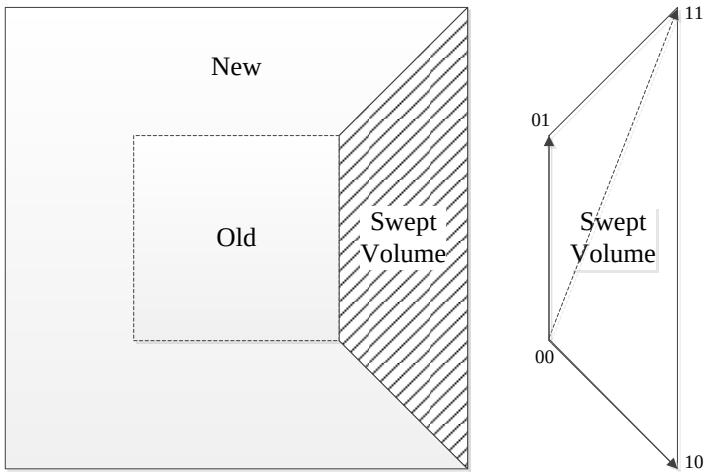

Figure 3.5 Application of SCL Condition

Flow Solver

After the grid movement fluxes are obtained, the next step is the advancement of the fluid solution with time, by solving time dependent, incompressible Arbitrary

Lagrangian-Eulerian (ALE) based space, continuity and momentum equations with constant properties in a generalized coordinate system. The SCL condition (Eq. (3.15)) is obtained as discussed in the previous section. The equations are non -dimensionalized using a^*, the artery radius for the length scale, $1/\omega^*$ for the time scale, $a^*\omega^*$ as the velocity scale, and $\rho\left(a^*\omega^*\right)^2$ as the pressure scale. The physical space ($\vec{x}$) is transformed to a computational space ($\vec{x}=\vec{x}\left(\vec{\xi}\right)$) using a boundary conforming transformation. Thus, the non-dimensionalized incompressible Navier-Stokes equations are of the form:

$$\frac{\partial}{\partial t}\left(\sqrt{g}\right)-\frac{\partial}{\partial \xi_j}\left(\sqrt{g}U_g^j\right)=0 \qquad \textbf{3.16}$$

$$\frac{\partial}{\partial \xi_j}\left(\sqrt{g}U^j\right)=0 \qquad \textbf{3.17}$$

$$\frac{\partial}{\partial t}\left(\sqrt{g}u_i\right)+\frac{\partial}{\partial \xi_j}\left(\left(\sqrt{g}U^j-\sqrt{g}U_g^j\right)u_i\right)=\frac{\partial}{\partial \xi_j}\left(\sqrt{g}\left(\overrightarrow{a^j}\right)_i p\right)+\frac{\partial}{\partial \xi_j}\left(\frac{1}{\Omega^2}\sqrt{g}g^{ik}\frac{\partial u_i}{\partial \xi_k}\right) \qquad \textbf{3.18}$$

The above Eqs. (3.16-3.18) are written in tensor notation where Ω is the Womersley number (defined as $\Omega=\sqrt{\frac{\rho\omega^*}{\mu}}a^*$), $\overrightarrow{a^i}$ is the contravariant basis vector, $\sqrt{g}$ is the Jacobian of the transformation, g^{ij} is the contravariant metric tensor, $\sqrt{g}U^j$ is the contravariant flux vector, $\sqrt{g}U_g^j$ is the contravariant flux vector due to grid movement, u_i is the Cartesian velocity vector and *p* is the pressure. It can be observed that the square of the Womersley number plays the role of the Reynolds number. With these modifications, the conservation equations for space, mass and momentum are discretized with a conservative finite-volume formulation on a multi-block body-fitted mesh using a second-order central difference scheme on a non-staggered grid topology. A projection method is used for time integration. Temporal advancement is performed in two steps, a predictor step, which calculates an intermediate velocity field, and a corrector step, which

calculates the updated velocity at the new time step by satisfying discrete continuity. Detailed information can be found in Tafti et al.[62-66] .

Post Processing and Calculation of Primary and Secondary Flow Fields

The final step in the algorithm is the calculation of the primary and secondary flow fields and the calculation of the hemodynamic parameters. This is done as follows. The Cartesian velocities can be cast in terms of the helical coordinates as shown below.

$$
\begin{aligned}
u_s &= -\frac{a}{\sqrt{a^2+b^2}}\sin(s)u + \frac{a}{\sqrt{a^2+b^2}}\cos(s)v + \frac{b}{\sqrt{a^2+b^2}}w \\
u_r &= \left(\sin\theta\cos(s) + \sqrt{a^2+b^2}\tau\cos\theta\sin(s)\right)u + \\
&\left(\sin\theta\sin(s) - \sqrt{a^2+b^2}\tau\cos\theta\cos(s)\right)v + \left(\sqrt{a^2+b^2}\kappa\cos\theta\right)w \\
u_\theta &= \left(\cos\theta\cos(s) - \sqrt{a^2+b^2}\tau\sin\theta\sin(s)\right)u + \\
&\left(\cos\theta\sin(s) + \sqrt{a^2+b^2}\tau\sin\theta\cos(s)\right)v + \left(-\sqrt{a^2+b^2}\kappa\sin\theta\right)w
\end{aligned}
\qquad \textbf{3.19}
$$

The secondary stream function in the r-θ plane is written as shown below in helical coordinates.

$$
\psi = -r\left(\begin{array}{l}\left(\sin\theta\cos(s) + \dfrac{\tau}{\sqrt{\kappa^2+\tau^2}}\cos\theta\sin(s)\right)u \\ +\left(\sin\theta\sin(s) - \dfrac{\tau}{\sqrt{\kappa^2+\tau^2}}\cos\theta\cos(s)\right)v + \dfrac{\kappa}{\sqrt{\kappa^2+\tau^2}}\cos(s)w\end{array}\right) \qquad \textbf{3.20}
$$

Here κ and τ are the curvature and torsion, as defined in Eqs (3.7-3.8). The forces in helical tube flows can be summarized as shown below in terms of the Dean number (Dn) and Germano number (Gn).

$$
\begin{aligned}
&F_{inertial} \propto \rho U^2 \\
&F_{centrifugal} \propto \rho U^2 \kappa \\
&F_{twisting} \propto \rho U^2 \tau \\
&F_{viscous} \propto \frac{\mu U}{D} \\
&Gn = \frac{F_{twisting}}{F_{viscous}} \quad \mathrm{Re}_D = \frac{F_{inertial}}{F_{viscous}} \quad Dn^2 = \frac{F_{inertial}}{F_{viscous}}\frac{F_{centrifugal}}{F_{viscous}} = \mathrm{Re}_D^2\,\kappa
\end{aligned}
\qquad \textbf{3.21}
$$

The wall shear stress (WSS) and the oscillatory shear index are calculated as shown below.

$$WSS = \frac{1}{\Omega^2}\frac{\partial u_s}{dr}$$

$$OSI = 0.5\left(1 - \frac{\left|\int_0^T \tau_w dt\right|}{\int_0^T |\tau_w| dt}\right) \quad \textbf{3.22}$$

Validation of FSI Methodology

The FSI methodology used was validated using two studies. The first study was to validate the fluid dynamics calculations for pulsatile flow conditions for a rigid vessel using the analytical solution due to Womersley[67]. The applied pressure gradient was of the form in Eq. (3.23).

$$\frac{\partial P}{\partial x} = B\cos(t) \quad \textbf{3.23}$$

Here B is the non-dimensional amplitude of the oscillation and in this example takes a value of 62.77. The inlet and outlet are made periodic based on the fully developed assumption inherent in the Womersley analytical solution. The fluid density is taken as 1060 kg/m^3, the dynamic viscosity is set as 4.876x10^{-3} kg/ms, with the vessel radius as 1.5x10^{-3} m and the frequency of oscillation equal to 1 Hz. Thus, the Womersley parameter is set to 1.7531. The comparison of the velocity profile at a given time is shown in Fig. 3.2a. It can be seen that there is an excellent agreement between the analytical solution and the obtained numerical solution, with the maximum error being 3%. Similar results were obtained for all other times as well. The comparison of the variation of flow rate with time in the axial direction for the numerical solution and the analytical solution also showed good agreement between the two.

To validate the fluid-structure interaction model and the developed procedure, simple sinusoidal flow conditions were applied to a straight tube for Navier Equations. The applied boundary velocity and the pressure profiles are shown in Eq. (3.24) below. The material properties applied are listed in Table 3.1. It should be noted that the parameters

used for this validation are not based on physiological conditions, but are used only for the validation of the FSI methodology.

Table 3.1 Wall properties used for the validation case

Parameter	Value
Vessel Radius (m)	0.0125
Vessel Length (m)	0.07
Fluid Kinematic Viscosity(m^2s^{-1})	4.9E-6
Fluid Density (kgm^{-3})	1060
Young's Modulus (Pa)	8.28E+07
Wall thickness(m)	0.00125
Wall Density (kgm^{-3})	1060
Wall Viscosity coefficient (Pa.s)	1.0E+03

$$P_{out}^{*} = \left(1123.834 + 1019.415\sin\left(\omega^{*}t^{*} - 8.8943\times10^{-3}\right)\right)Pa$$
$$V_{out}^{*} = \left(0.03927 + 0.02668\sin\left(\omega^{*}t^{*}\right) + 0.01140\sin\left(\omega^{*}t^{*}\right)\right)m/s \quad \textbf{3.24}$$

The analytical results due to Zamir[68] are used for validating the simulation. There was excellent agreement between the numerically obtained deformation and the analytical deformation, with the maximum error being around 2%. A comparison of the velocity profiles is shown in Fig. 3.2b, which again shows good agreement between the numerical and the analytical results.

Based on these validations, it is established that the method used in this work is accurate in predicting the fluid flow resulting from time varying pressure and velocity boundary conditions representative of cardiovascular systems. It also establishes the coupling between the internal flow and structural deformation representative of compliant arteries. The same grid resolutions used in the validation studies is used in the actual simulations under physiologically relevant conditions.

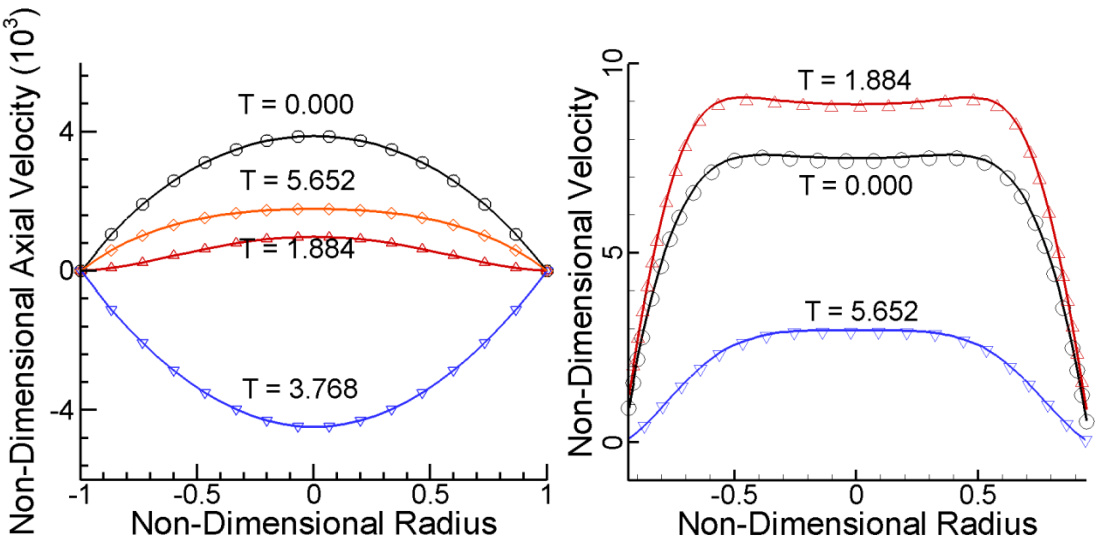

(a) (b)

Figure 3.6 (a) Comparison of analytical solution due to Womersley and the current numerical solution at T = 0.000, 1.884, 3.768 and 5.652 time units. (a) Comparison of analytical solution due to Zamir[68] and the current numerical solution at T = 0.000, 1.884 and 5.652 time units. The symbols are due to the analytical solution and the solid lines are due to the current numerical solution.

Validation of Large Scale External Applied Motion

Santamarina et al. [69] had measured experimentally the velocity profiles using pulsed Doppler ultrasound velocimeter in a time varying curved planar tube. The geometrical parameters used in the experiment are listed in Table 3.2. Here the deformation parameter (ε) is defined as the ratio of amplitude of the change in radius of curvature and the mean radius of curvature; the Reynolds number is based on the mean velocity and the Womersley parameter (defined using the frequency of curvature change) as the time scale. The velocity data from this experiment is used to validate the methodology used in this study. In the experiment, the deformation of the tube was produced using a motor coupled through a crank-piston linkage to a carriage that slides on two rails. The crank-piston linkage converts the rotary motion of the motor to a cosine wave form, as shown in Eq. (3.25). The resulting waveform was used in the computational model, along with the other parameters listed in Table 3.2.

Table 3.2 Experimental parameters for validation

Tube radius/Curvature radius	Deformation Parameter (ε)	Reynolds Number	Womersley Parameter based on curvature change frequency
0.043	0.26	300	4.2

The comparison of the experimental results from [69] and the numerical study is shown in Fig. 4, at 8a from the inlet at four times during the cycle. The numerical results fall well within the limits of experimental uncertainty. The large excursions of velocity near the walls seen in the experimental results might be due to reflection errors. Similar results were obtained at the other locations from the inlet as presented in [69]. Thus, it was concluded based on these validation results that the moving boundary methodology developed and used in this work is accurate in predicting the tube wall movement and the associated fluid dynamics of the artery system studied. It should be noted that the grid resolution in the radial direction used for the validation studies is the same as that used for the actual simulations in the current study.

$$R(t) = R_{mean}\left[1+\varepsilon\cos(\omega t)\right] \qquad \textbf{3.25}$$

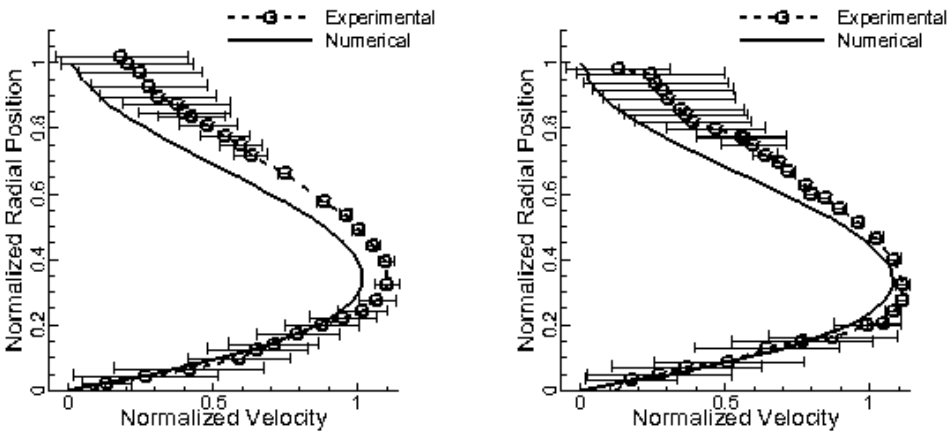

(a) (b)

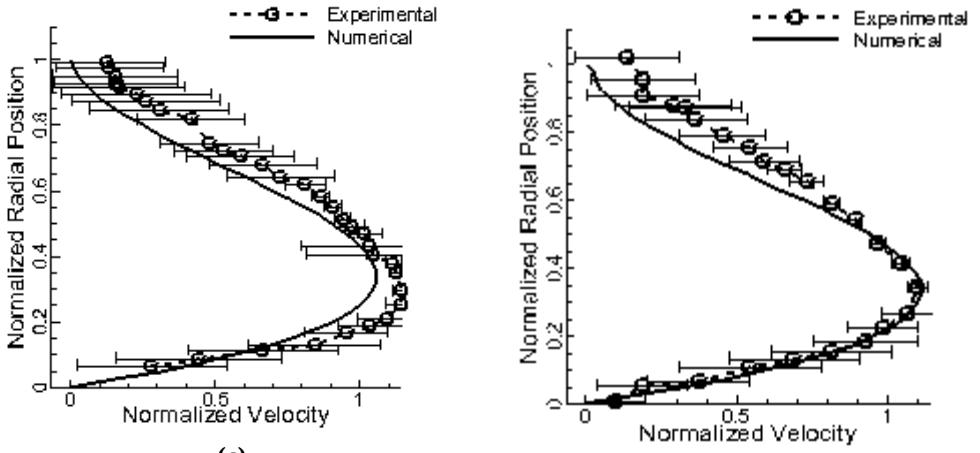

Figure 3.7 Comparison of numerical results with experimental velocity profiles at 8a from the inlet. (a) at 0.04T (b) at 0.28T (c) at 0.49T (d) at 0.73T

4. Hydrodynamic Effects of Compliance Mismatch in Stented Arteries

Introduction

Stent design profoundly influences the post-procedural hemodynamic and solid mechanical environment of the stented artery. However, despite their wide acceptance, the incidence of stent late restenosis is still high[70], and it is most prevailing at the proximal and distal ends of the stent. In this chapter, we focus our investigation on the localized hemodynamic effects of compliance mismatch due to the presence of a stent in an artery. The compliance mismatch in a stented artery is maximized at the proximal and distal ends of the stent. Hence, it is our objective to understand and reveal the mechanism by which changes in compliance contribute on the generation of non-physiological wall shear stress. Such adverse hemodynamic conditions could have an effect on the onset of restenosis. Three-dimensional, spatiotemporally resolved Computational Fluid Dynamics (CFD) simulations of pulsatile flow with Fluid-Structure Interaction (FSI) were carried out for a simplified coronary artery with physiologically relevant flow parameters. A model with uniform elastic modulus is used as the baseline control case. In order to study the effect of compliance variation on local hemodynamics, this baseline model is compared to models where the elastic modulus was increased by two, five and ten fold in the middle of the vessel. The simulations provided detailed information regarding the recirculation zone dynamics formed during flow reversals.

Boundary Conditions

To study the effect of compliance change on hemodynamics, a simplified straight coronary artery is used. The computational grid consists of ten blocks, each having 69360 cells. The applied representative inlet velocity waveform and the outlet pressure waveform corresponding to observed pulse waveforms for healthy resting conditions are shown in Fig. 4.1 [71]. The peak flow rate corresponds to the diastolic phase and the reversal in flow corresponds to the systole, typical for coronary flows.

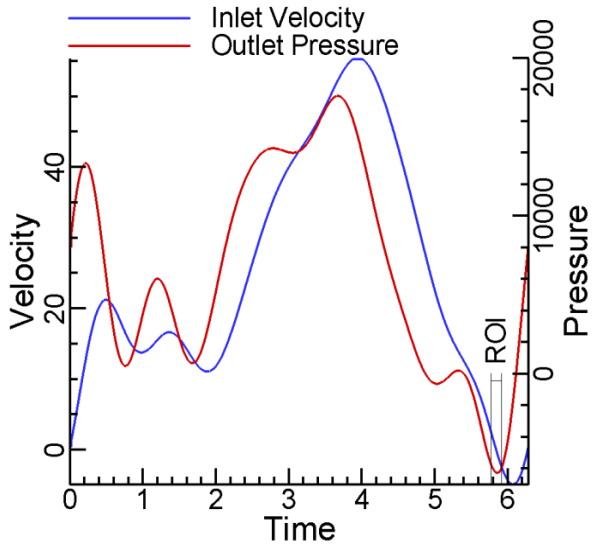

Figure 4.1 Applied coronary artery inlet velocity and outlet pressure waveforms with the region of interest (ROI) indicated

The vessel is modeled with an exponential taper, which is shown in Eq. (4.1).

$$r(x) = r_{in} e^{\left(\log\left(\frac{r_{out}}{r_{in}}\right)\frac{x}{L}\right)} \qquad \textbf{4.1}$$

The taper used is as suggested by Olufsen et al.[72]. The inlet radius of the coronary artery geometry used was set to 1.5mm and the outlet was set to 1.37mm with the total length of the vessel being 8.4mm. The arterial wall thickness was set to 10% of the radius and the Young's modulus was set to 1.15MPa for the normal unstented vessel that was used as the baseline case to study the effect of the compliance change on hemodynamics. Other relevant properties are listed in Table 4.1. The Womersley number for this study is 1.7531 and the maximum Reynolds number based on vessel diameter is 340. The values used fall within observed physiological variations due to various biological factors. The peak velocity for this Reynolds number is 55.4 units and the near wall grid resolution is $8x10^{-3}$ units. The resolution of the boundary layer plays an important role in accurately calculating the wall shear stresses. For the current study, the near wall resolution needed to maintain a y^+ of 1 is 0.019 units, which is more than two times higher than the used near wall grid resolution. The temporal descretization used for the calculations was 1e-4 units, selected to maintain the CFL number less than 0.1. Compared to the similar studies [56, 73-77], the grid spacing used in this study is at least two times smaller. Thus, the grid independency of the solution obtained is established.

Table 4.1Wall properties used for the base line unstented case

Parameter	Value
Vessel Inlet Radius (m)	0.00150
Vessel Outlet Radius (m)	0.00137
Vessel Length (m)	0.00840
Fluid Kinematic Viscosity(m^2s^{-1})	4.9E-6
Fluid Density (kgm^{-3})	1060
Young's Modulus (Pa)	1.15E+06
Wall thickness(m)	1.5E-04
Wall Density (kgm^{-3})	1060
Wall Viscosity coefficient (Pa.s)	1.0E+03

Vernhet et al. [78] observed that after three months the compliance values at the stented section were smaller than surrounding unstented tissue by a factor of 5-6 times. Thus to study the effect of compliance mismatch, the Young's Modulus was changed in the middle section of the vessel to values 2, 5, and 10 times the baseline value. The ratio of the elastic modulus along the length of the vessel to the baseline value is shown in Fig. 4.2.

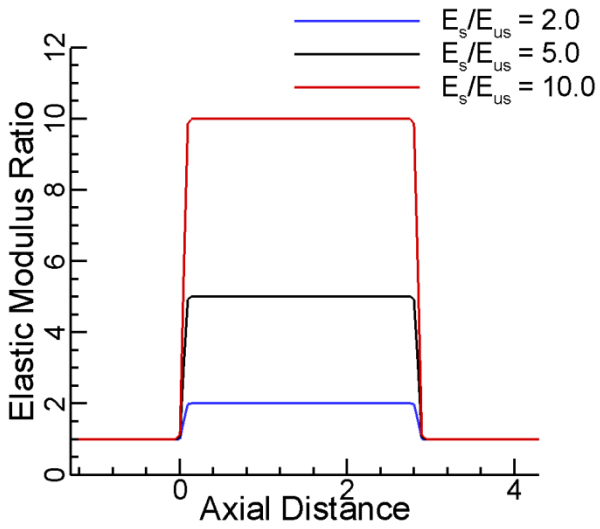

Figure 4.2 Change in compliance due to stent effects that is applied to the stented cases, as compared to the unstented base line case.

In order to prevent sudden jumps in compliance, an exponential curve fit was used, as seen in Fig. 4.2 and as shown in Eq. (4.2), where constant 'a' takes values of 1,4 and 9 for Young's Modulus ratio of 2,5 and 10 respectively. All the other properties remain unchanged as listed in Table 4.1. To make sure that the results obtained are repeatable, all

calculations were run at least for three cycles. It should be also noted that the proximal location of the stent is located at axial coordinate 0.0 and the distal end is located at 2.8.

$$E(x)=\begin{cases}1+\dfrac{a}{\left(1+e^{-90(x-0.046667)}\right)}, x\le 1.4\\ 1+\dfrac{a}{\left(1+e^{-90(x-2.846667)}\right)}, x>1.4\end{cases} \quad \textbf{4.2}$$

Results

For the baseline unstented vessel, it was seen that the pressure does not vary much from the outlet pressure. Similar observations were made by Tezduyar et al.[79]. The pressure variation from the outlet value at the sections away from the outlet is higher during the diastolic phase of the cycle, because the velocity is highest during this part of the cycle. The stented cases show similar pressure and velocity trends. It was seen that the variation of the radial displacement follows the variation of the pressure with time. Due to the increase in elastic modulus at the middle section for the stented cases, the wall is stiffer at this section. This leads to proportionally smaller wall deformation with respect to the increase in elastic modulus than the unstented base line case. This reduced deformation would affect the near wall flow field and thus the wall shear stresses. A similar variation of radial displacement with axial distance was obtained for all the test cases, with the displacement following the variation in pressure along the length of the vessel.

Comparison of Stented and Unstented Compliance Effects – Flow Characterization

The flow characterization in a stented artery depends on the flow waveform, pulsatility and the compliance variation between the stented and unstented section. Vortex formation has been shown to occur due to the compliance mismatch between the stented and unstented sections of the artery[41]. To understand the effects of the compliance mismatch on the local hemodynamics, the time evolution of the vortices are presented in this section using instantaneous streamlines. When the velocity decelarates and reverses direction, the flow is unstable with possible separation and shearing of the near wall fluid layers. Thus the results in this section focus on the time in the vicinity of a flow reversal that occurs at T = 5.838. Here the flow changes direction from the positive, forward

direction to the negative, reverse direction (Fig 4.1). Similar results can be expected for the second flow reversal at the end of the cycle, when the flow changes back to the positive direction. Figs. 4.3 – 4.4 are focused at the distal end of the stent and the time intervals between the shown flow fields are $\Delta T = 0.03$, starting at $T = 5.768$, except for panels labeled (c) and (d).

The transient boundary layer thickness is defined as:

$$\delta = \frac{1}{\Omega} \qquad \textbf{4.3}$$

The unsteady boundary layer thickness for the current study, based on Eq. (4.3) is 0.5704. The general flow characteristics are similar for all the cases studied, but with distinct differences with respect to the size and residence times of the recirculation zones observed. As the flow decelerates, the pressure gradient changes and becomes adverse. This adverse upstream pressure gradient acts on the flow with time. Since the kinetic energy of the fluid is less at the wall, the flow reverses first near the wall, leading to the formation of shear layers (Fig. 4.3a, 4.4a). As the flow decelerates further, the shear layer destabilizes near the distal end of the stented region and begins to roll in a spiral motion resembling a recirculation zone (Fig. 4.3b, 4.4b). Eventually, a circumferential recirculation zone is formed at the distal end (Fig. 4.3d, 4.4c). As the flow changes direction, the recirculation zone formed migrates to the center of the vessel due to the growth of the near wall shear layer. The recirculation zone eventually diffuses into the main flow, leading to the complete reversal of the flow.

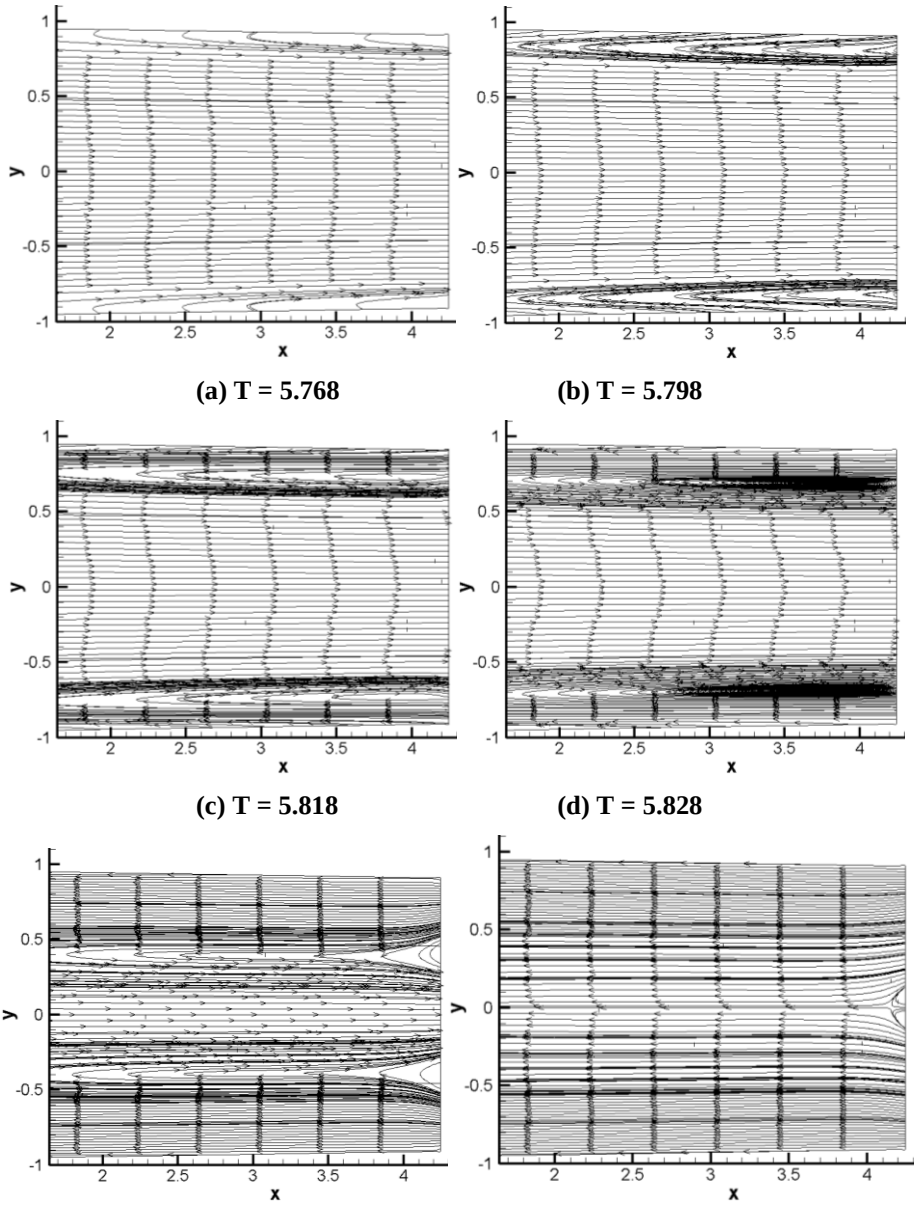

(a) T = 5.768 **(b) T = 5.798**

(c) T = 5.818 **(d) T = 5.828**

(e) T = 5.858 **(f) T = 5.888**

Figure 4.3 Flow field evolution at the distal end located at 2.8 units, starting from T = 5.768 for the unstented vessel.

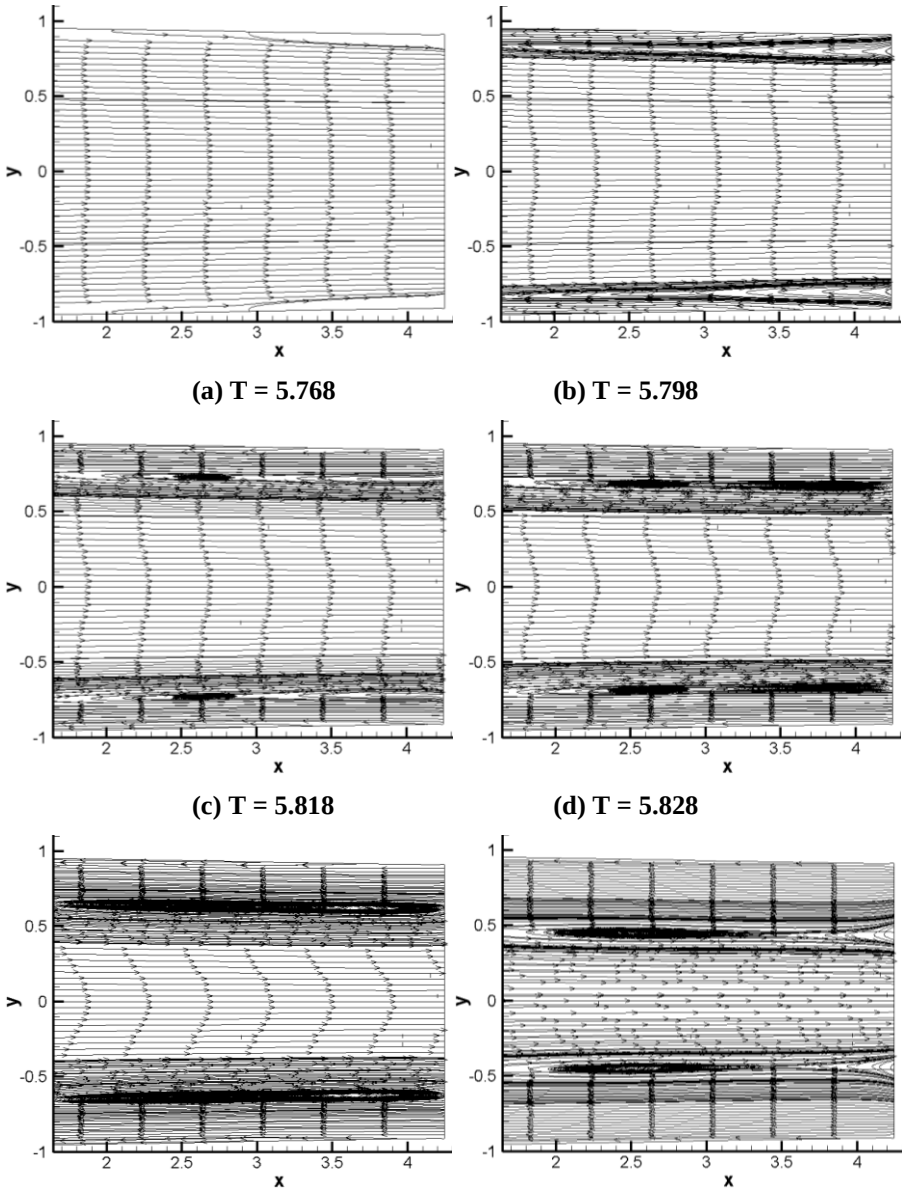

(a) T = 5.768 **(b) T = 5.798**

(c) T = 5.818 **(d) T = 5.828**

(e) T = 5.858 **(f) T = 5.888**

Figure 4.4 Flow field evolution at the distal end located at 2.8 units, starting from T = 5.768 for the stented vessel with Es/Eus = 10.0.

Comparing the flow characteristics for the different compliance cases, the following observations are made:

- The recirculation zone forms earlier as the stiffness increases, as seen from Fig. 4.4c, compared to Fig. 4.3d
- The recirculation zone size increases with stiffness, as seen from Fig. 4.4d and 4.4e, compared to Figs. 4.3d, 4.3e.
- The recirculation zone dissipation rate is inversely proportional to the stiffness and the residence time is proportional to the stiffness. For the unstented case, the recirculation zone formed is dissipated much earlier as seen in Figs. 4.3e and 4.3f, compared to Figs. 4.4e, 4.4f. Based on the observed snapshots of the flow field, an approximate increase of 50% in residence time was seen.
- The shearing of the fluid layers near the wall is more persistent for the stented cases, delaying complete flow reversal.
- The longer residence time of the recirculation zone might increase platelet residence time near wall and alter near wall shear stresses

Yazdani et al.[41] obtained similar results. Thus compliance mismatch dominates the local flow field, indicating that the mechanical properties of the stent affects the local hemodynamics.

Comparison of Stented and Unstented Compliance Effects – Hemodynamic Parameters

The variation of the wall shear stress (WSS) with the axial distance is shown in Fig. 4.5a. It can be seen that there is a clear increase in WSS at the locations where the elastic modulus changes from the uniform compliance value to the higher value. This is mainly due to the fact that the vessel does not deform as it would if the compliance was the same throughout, leading to the increase in the axial velocity near the wall. This effect is reversed at the end of the higher compliance section, due to the fact that the vessel expands more after the stent, leading to a decrease in axial velocity. The change in WSS in the stented vessels with respect to the unstented vessel is as high as 9% at the entrance to the stent where the elastic modulus ratio changes.

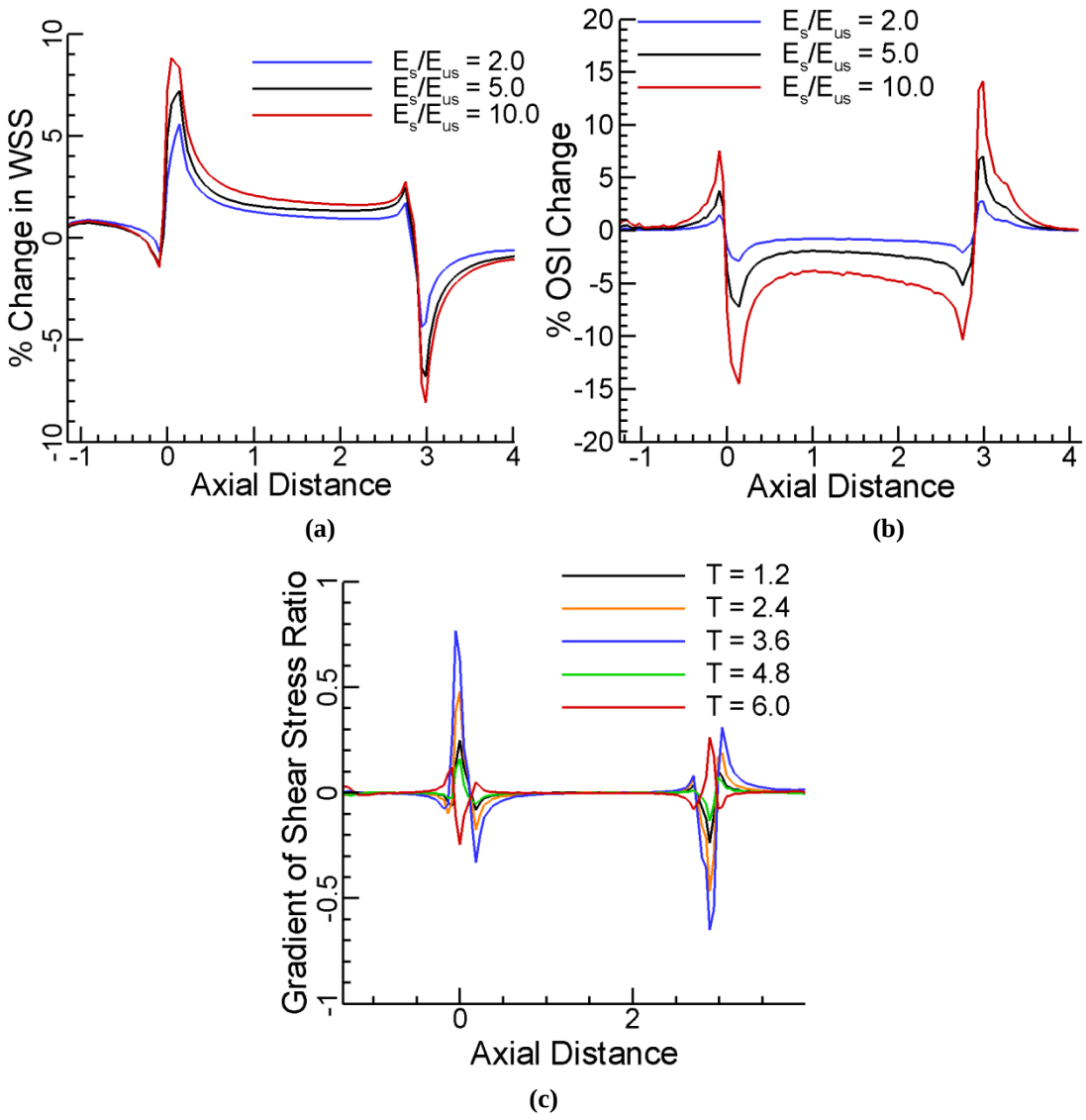

Figure 4.5 (a) Percentage change in time averaged WSS with respect to the unstented vessel (b) Percentage change in OSI of the stented vessel with respect to the unstented vessel (c) Gradient of shear stress ratio vs. axial distance at different times, when the velocity peaks

The Oscillatory Shear Index (OSI) is defined in Eq. (4.4). The variation of the percentage change in OSI along the length of the vessel with respect to the unstented vessel is shown in Fig. 4.5b. The percentage change is more pronounced at the points where there is a jump in elastic modulus at the entrance and exit to the stented section, with a change as high as 15% when compared to the unstented vessel.

$$OSI = 0.5\left(1 - \frac{\left|\int_0^T \tau_w dt\right|}{\int_0^T |\tau_w| dt}\right) \qquad \textbf{4.4}$$

The gradient of the shear stress ratio, (defined as the instantaneous ratio of the axial gradient WSS of the stented vessel to the unstented vessel) along the length of the vessel is shown in Fig. 4.5c for five different times for E_s/E_{us} = 5.0. It can clearly be seen that the axial gradient of wall shear stress ratio moves away from zero exactly at the location where the compliance changes from the nominal value to the higher value used to simulate the effect of a stent. For times T = 1.2, 2.4, 3.6 and 4.8, the flow is still in the positive direction, from the inlet to the outlet. For T = 6.2, the flow is in the negative direction. For the times when the flow is in the positive direction, the gradient of the shear stress ratio increases at the entrance of the stent as the wall shear stress increases (Fig. 4.5a). This value then drops to zero as we move away from the discontinuity, followed by a decrease of the gradient of wall shear stress ratio at the exit of the stent, as the wall shear stress decreases. A reverse trend is seen for T = 6.2. Again as seen in the above results, there is a significant change in the shear stress gradient at the entrance and exit of the stent where the elastic modulus changes value from that at the inlet, indicating that this change in compliance causes major changes in local hemodynamics that may influence restenosis.

The variation of the percentage change in pressure is shown in Fig. 4.6a. Even though the pressure does not change significantly from the unstented to the stented vessel, it is observed from Fig. 4.6b that the change in pressure gradient from the stented to the unstented case is quite significant and is as high as 90% at the entrance to the stent, where the compliance changes from the uniform value.

Discussion

The above results demonstrate that the change in compliance due to the presence of the stent causes changes in residence times and the size of the recirculation zones at the proximal and distal ends of the stent. Changes also in the near wall shear stresses was seen at the discontinuity of compliance, as manifest in changes of WSS, OSI and WSSG.

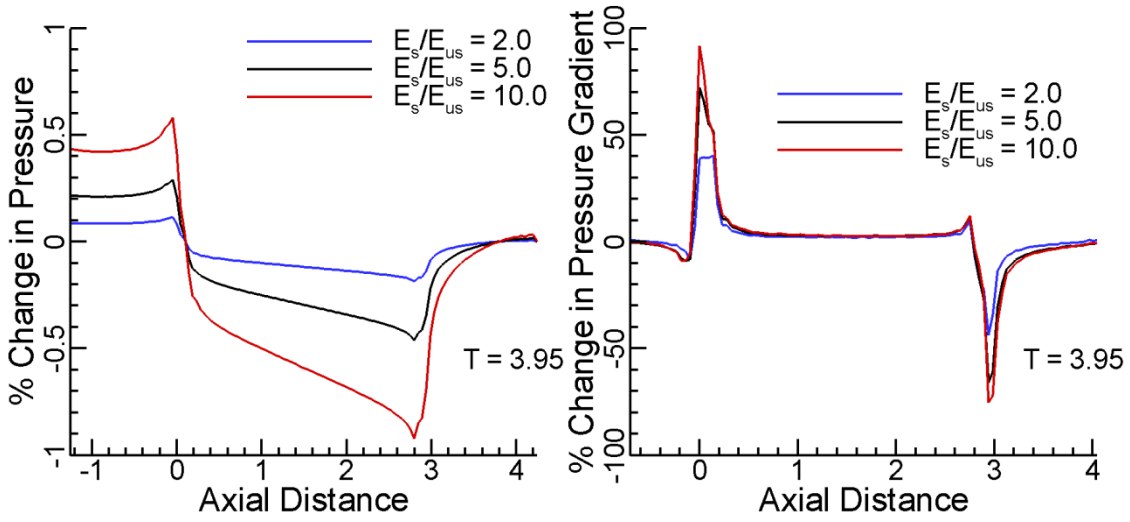

(a) **(b)**

Figure 4.6 (a) Percentage change in pressure and (b) Change in Pressure Gradient between the stented vessel and the unstented vessel

Vorticity Flux Density

In trying to understand the physical mechanism responsible of these changes, the relationship between pressure gradient and vorticity flux is presented here. The role of vorticity (curl of velocity vector) in explaining the fluid dynamic phenomena is well established, starting with the work by Lighthill [80], who pointed out that solid boundaries act as distributed sources of vorticity. He was also the first to define a term for vorticity production called vorticity flux density, defined as shown below in Eq. (4.5).

$$\nu\left(\frac{\partial\omega}{\partial y}\right)_w \qquad \textbf{4.5}$$

Lighthill also pointed out that the vorticity flux is directly related to the pressure gradient at the wall, although the vorticity transport equation does not contain the pressure gradient term explicitly. If the momentum equation is written for a stationary wall, at the wall:

$$-\frac{1}{\Omega^2}\left(\frac{\partial\omega_z}{\partial y}\right)_w = \frac{\partial p}{\partial x} \qquad \textbf{4.6}$$

Here, p is the pressure at the wall and ω is the transverse component of vorticity. In the above equation, all the components of velocity at the stationary wall are zero. Extending the above to a wall with radial displacements, it can be seen that only the wall normal velocity is non-zero, thus the axial momentum equation in cylindrical coordinates at the moving wall reduces to Eq. (4.7).

$$-\frac{1}{\Omega^2}\left(\frac{1}{r}\frac{\partial}{\partial r}(r\omega_\theta)\right)_w = \left(\frac{\partial p}{\partial x} + v_r\frac{\partial u}{\partial r}\right) - \frac{1}{\Omega^2}\frac{1}{r}\left(\frac{\partial}{\partial r}\left(r\frac{\partial v_r}{\partial r}\right)\right) \qquad \textbf{4.7}$$

In the above equation, the dominant term is the pressure gradient, which is on average three orders higher compared to the other terms for this study. The time-averaged variation of the vorticity flux ratio with respect to the unstented case (Eq. (4.7)) is shown in Fig. 4.7a.

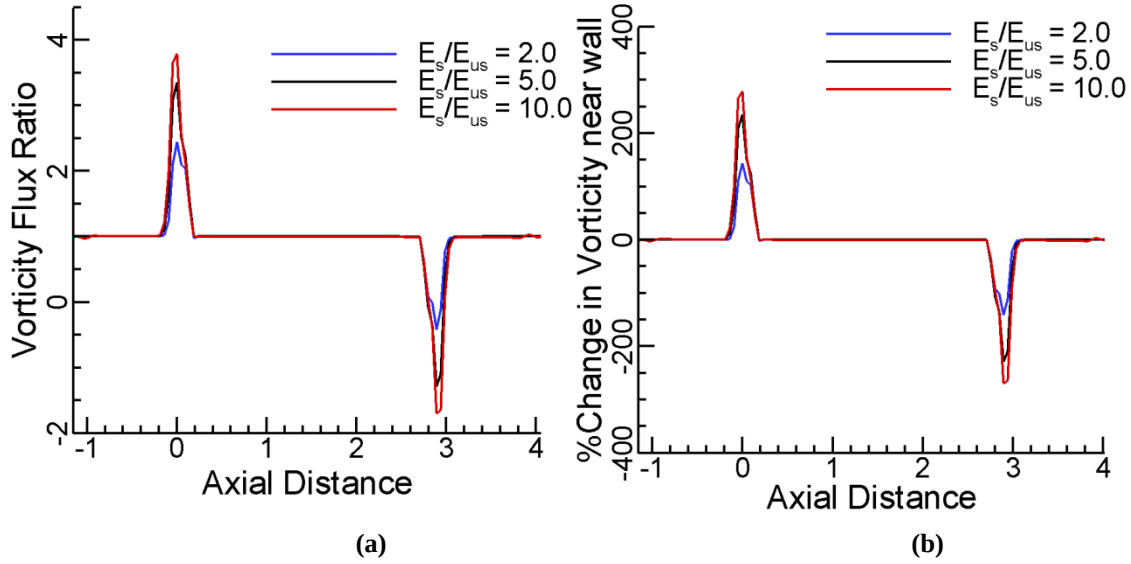

(a) **(b)**

Figure 4.7 (a) Time averaged Vorticity flux density Ratio versus Axial Distance (b) Time averaged vorticity change near wall with respect to the stented and unstented vessels

It is seen that the vorticity flux is more pronounced at the compliance discontinuities, similar to the discontinuities in pressure gradient seen in Fig 4.6b. This shows that pressure gradient is the cause of vorticity discontinuities near the wall. The wall shear stress is related to the vorticity at the wall as shown in Eq. (4.8), thus pointing to a relationship between the pressure gradient and the wall shear stress through vorticity.

$$\omega_w \times n = \Omega^2 \tau_w \qquad \textbf{4.8}$$

Here ω_w is the wall vorticity vector and n is the wall normal unit vector. The vorticity change shed from the wall and propagated in the radial direction away from the wall is obtained using a first order approximation as shown in Eq. (4.9).

$$\left(\frac{1}{r}\Delta\left(r\omega_\theta\right)\right)_w = -\Omega^2\left[\left(\frac{\partial p}{\partial x}+v_r\frac{\partial u}{\partial r}\right)-\frac{1}{\Omega^2}\frac{1}{r}\left(\frac{\partial}{\partial r}\left(r\frac{\partial v_r}{\partial r}\right)\right)\right]\Delta r \qquad \textbf{4.9}$$

Here Δr is the distance of a point in the flow from the wall and $\Delta\omega_{\theta\ is}$ the change in vorticity shed into the flow. For the near wall points, the obtained change in vorticity for the stented cases with respect to the unstented values is shown in Fig. 4.7b for time averaged values. It can be seen that the proximal end of the stent acts as a source and the distal end of the stent acts as a sink of vorticity. Thus from the above discussion (vorticity flux production due to the pressure gradient), it can be seen that the vorticity produced due to the presence of the stent, would directly affect the wall shear stress and influence endothelial response.

Stent Authority

Figure 7a shows the variation of the time averaged peak difference in pressure gradient at the proximal location with stent stiffness relative to that of the vessel. From the inspection of the plot, the variation appears as a hyperbolic tangent, with pressure gradient difference being zero for the unstented vessel and asymptotically reaching a maximum value as the stiffness increases. This was similar to observations made by Charonko et al. [33], who looked at pressure reflections using 1D analysis for different stent stiffness values. Following Charonko et al. [33], a non-dimensional number referred to as stent authority is defined as shown in Eq. (14)

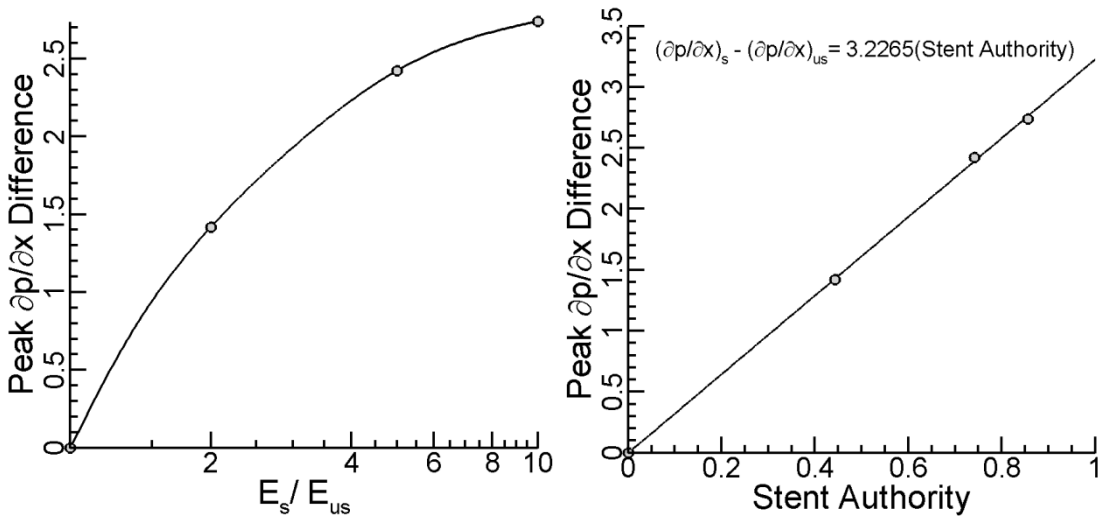

Figure 4.8 (a) Time averaged peak pressure gradient difference at the proximal end versus stent stiffness ratio (b) Peak pressure gradient difference at the proximal end versus stent authority.

$$SA = \tanh\left(\log\left(b\left(\frac{E_s}{E_{us}} - 1\right) + 1\right)\right) \qquad \textbf{4.10}$$

From Eq. (4.10), the stent authority takes a value of zero when the stiffness ratio becomes one and it takes a value of one when the stiffness ratio tends to infinity[33]. For the data presented in Fig 4.8a, the parameter *b* was calculated using a curve fit to be 1.9953 versus 2.198 by Charonko et al. [33]. As can be seen in Fig. 4.8b, applying Eq. (4.10) to the difference in peak pressure gradient at the proximal end resulted in a linear relationship between stent authority and the peak pressure gradient difference. The stent authority provides a measure of the peak pressure gradient difference at the proximal location for a given discontinuity in compliance, providing a quick prediction of this quantity for a given stent stiffness. For the present study, the resulting proportionality constant was 3.226 of stent authority versus 3.46 from Charonko et al. [33].

Significance of the Simulation Results Presented in this Chapter

The vascular endothelium shows a variety of responses to local flow conditions. The endothelial cells align with the direction of flow, activate ion channels, organize internal cytoskeletal structures, monolayers divide in the presence of turbulent flows, to name a few[51, 52]. Certain regions of the arterial wall normally undergo structural remodeling

that is characterized by intimal thickening which is hypothesized to represent localized biological responses to high mechanical forces and shear stress conditions to which these regions are subjected to [51, 52]. Kamiya et al. [53, 54] applied optimization techniques to demonstrate that the response of the endothelium to varying shear conditions was to maintain a constant wall shear stress within a narrow region of 10-20 dyne/cm^2**.** WSS values outside this range can trigger neointima formation and proliferation of smooth muscle cells thickening the vascular wall in an attempt to restore wall shear stress within physiological values.

Thus, it can be concluded that local hemodynamics, especially shear stress distributions and gradients play a critical role in understanding the physiological response of the endothelium, leading to stenosis and other pathological conditions found at sites of compliance mismatch and discontinuity. Here we emphasize some of the results shown in Fig. 4.6. In Fig. 4.6a, the axial pressure distribution and the corresponding changes are shown. Seemingly very little change (~1%) results from the presence of the compliance transition. However, the effect of the compliance transition is clearly shown with sharp discontinuities in the pressure at the entrance and the exit of the stent. As Fig. 4.6 reveals, that small change in pressure results in more than 90% change in the local pressure gradients with a corresponding increase in the WSS and OSI. This large increase in pressure gradient leads to an increase in the local velocity gradients near the transition region, and therefore increased vorticity flux generated there as seen in Fig. 4.7, directly affecting the wall shear stresses seen (Eq. (4.8)). The variation of the WSS, OSI and WSSG along the length of the vessel revealed discontinuities at the transition regions as indicated by the pressure gradient. If we are to use the hypothesis by Lei et al. [81] where they state that sites of large magnitude of shear stress gradients are prone to lesions, arteriosclerosis and endothelial response through intimal thickening, the conclusion to be drawn would be that the start and end of the compliance mismatch or discontinuity are sites that would lead to intimal thickening. Various studies in the literature also implicate factors like WSS and OSI. From the results presented these factors also show that sites of compliance mismatch would lead to an intimal thickening.

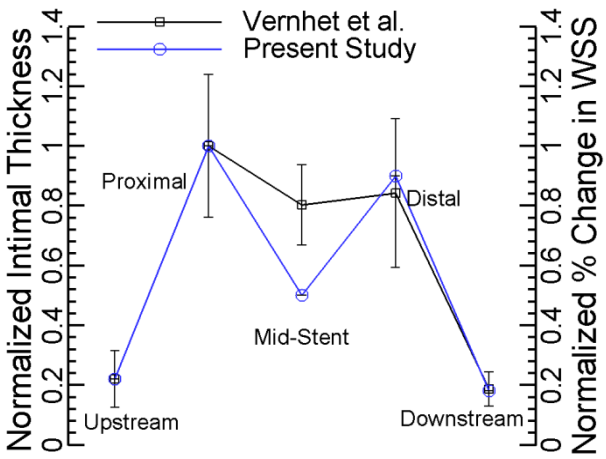

Figure 4.9 Variation of Intimal Thickness based on histological measurements due to Vernhet et al[78], in 10 animals and the absolute percentage change in WSS from the present study. Both the plots are normalized by the maximum value, which occurs at the proximal location.

Histological measurements of the intimal thickness made at three months after stenting in animal models by Vernhet et al [78] in 10 animals is shown in Fig. 4.9. The stents were placed under normal dilation conditions during the experiments. From these measurements, corresponding to long-term stenting effects in humans, the intimal layer thickness is markedly different in the stented section when compared upstream and downstream of the stent. Within the stented region itself, the proximal and the distal regions show higher intimal thickness, supporting the conclusions made in this chapter, that the sites with compliance mismatch are more prone to intimal thickening, due to adverse hemodynamic effects. For example, the change in WSS is highest in the proximal region, followed by the distal region and the mid-stent region in the present study, as shown in Fig. 4.9. As would be expected, the current model used in this study predicts that the pressure gradient and the vorticity flux discontinuities at the proximal and distal ends decreases as the stent compliance approaches that of the vessel wall. This suggests that it would be better to design a stent that is as compliant as possible, without loss of required functionality as supported by clinical research.

Limitations of the Work Presented in this Chapter

The present study is subject to several assumptions, simplifications and limitations that are discussed below. First, the effect of the stent deployment strategy and the post stent injury caused to the artery that would contribute to restenosis is not considered. However,

the objective of the current study was to isolate the effects of the change in compliance due to the presence of an idealized stent on the flow and on the hemodynamic parameters that have been implicated in stenosis. This study does not consider the effect of changes in mechanical stresses in the vessel wall that might be important and affect remodeling. However, this effect is compounded by the combined hemodynamic changes, and literature suggesting that changes in hemodynamics would affect stenosis is extensive. Yet, if and how compliance mismatch affects the local hemodynamics is unresolved. The present study aims to help understand this effect. The wall model used to calculate the radial deformations due to the fluid flow is a modified version of the model of independent rings, with an additional term to model the viscoelastic behavior of the wall. Only the radial deformation term is considered, due to the fact that the radial forces (pressure) dominate the other fluid stress components by at least two orders in magnitude, and thus would contribute to a larger extent to the flow disturbances due to the presence of the stent. This model has been used extensively in the literature [56, 73-77] and has been shown to agree with experiments. This model predicts the wall shear stress accurately and can thus be used as a good predictor of local hemodynamic function. An exponential transition of the elastic modulus is used, as indicated in Fig. 4.2. Care was taken to make sure that the elastic modulus transition was continuous and smooth. It is acknowledged that the transition used in the current study might be less gradual than in reality and this might cause some over prediction of the parameters presented in this paper.

Conclusion

Three-dimensional CFD calculations have been performed for pulsatile flow with fluid-structure interaction in a simplified coronary artery, using physiologically relevant flow waveforms, with the objective of studying the effect of compliance variation on the local hemodynamics. The elastic modulus was changed from the baseline case to a value that is 2, 5 and 10 times higher in the middle of the vessel and the effect of this change on the hemodynamics was investigated. It is seen that as the relative stiffness increases, the size and the residence times of the recirculation zones, the change in pressure gradient, WSS and OSI increase. This increase is more dominant at the compliance discontinuities, at the

proximal and distal ends of the stent. The change in pressure gradient at the discontinuity was as high as 90% and the corresponding changes in WSS and OSI calculated were 9% and 15%, respectively. We have demonstrated that these changes are attributed to the physical mechanism associating the pressure gradient discontinuities to the production of vorticity (vorticity flux) due to the presence of the stent. Subsequently, these pressure gradient discontinuities and augmented vorticity flux affect the wall shear stresses. Following Charonko et al.[33], a scaling parameter was also defined called stent authority (Eq. (4.10)) for the peak difference in pressure gradient at the proximal end. This parameter can be used to find the peak pressure difference for a given relative stent stiffness.

5. Effect of Dynamic Change in Curvature and Torsion on Pulsatile Flow in Rigid Helical Tube

Introduction

The effect of motion of the coronary artery due to the motion of the myocardium is not studied extensively. In this chapter, we focus our investigation on the localized hemodynamic effects of dynamic changes in curvature and torsion. It is our objective to understand and reveal the mechanism by which changes in curvature and torsion contribute towards observed wall shear stress distribution. Such adverse hemodynamic conditions could have an effect on circumferential intimal thickening. The results suggest that changes in curvature and torsion cause critical changes in local hemodynamics, namely altering the local pressure and velocity gradients and secondary flow patterns. WSS varies by a maximum of 22% when curvature changes, by 3% when torsion changes and by 26% when both curvature and torsion change. OSI varies by a maximum of 24% when curvature changes, by 4% when torsion changes and by 28% when both curvature and torsion change. We will in this chapter, demonstrate that these changes are attributed to the physical mechanism associating the secondary flow patterns to the production of vorticity (vorticity flux) due to the wall movement.

Boundary Conditions

In order to study the effect of the curvature and torsion, a simplified coronary artery in the form of a helix resting on a cylindrical heart is used. The maximum height and radius of the heart was set to 0.09m and 0.03m respectively, with the radius of the helical tube being 0.0015m. This is shown schematically in Fig. 5.2, at time levels indicated by T = 0.0. The heart rate was set to 60 beats/min. The time varying contraction and expansion of this mock heart can be modeled as a cosine function. This applied cosine wave form is a simplification of the volume variation of the left ventricle, with the first half of the cycle representing the systole and the second half of the cycle representing the diastole. The curvature and torsion of a helix is defined as shown in Eqs (5.1-5.2) below.

$$\kappa = \frac{\alpha}{\alpha^2 + \beta^2} \qquad \textbf{5.1}$$

$$\tau = \frac{\beta}{\alpha^2 + \beta^2} \qquad \textbf{5.2}$$

In Eqs (5.1-5.2) ‘α’ is the radius of the cylinder on which the helix rests and ‘β’ is the circumferential raise of the helix (if ‘h’ is the height of the cylinder, then $2\pi\beta = h$). In order to understand the physical meaning of curvature and torsion, consider a rectangular sheet, with height h and a width of $2\pi\alpha$. Consider three lines drawn on this surface – a horizontal line drawn end to end at an arbitrary height, a vertical line drawn end to end at an arbitrary horizontal position and a diagonal of the rectangle. If the sheet is rolled into a cylinder by joining the vertical edges, the vertical line will still be vertical and is analogous to a helix that has only torsion, with a value of $1/\beta$. The horizontal line will be from a circle, whose curvature is $1/\alpha$. The diagonal would form a helix with the curvature and torsion as defined in Eqs. (5.1) and (5.2). These three lines form the limiting cases for curvature and torsion for a given cylinder.

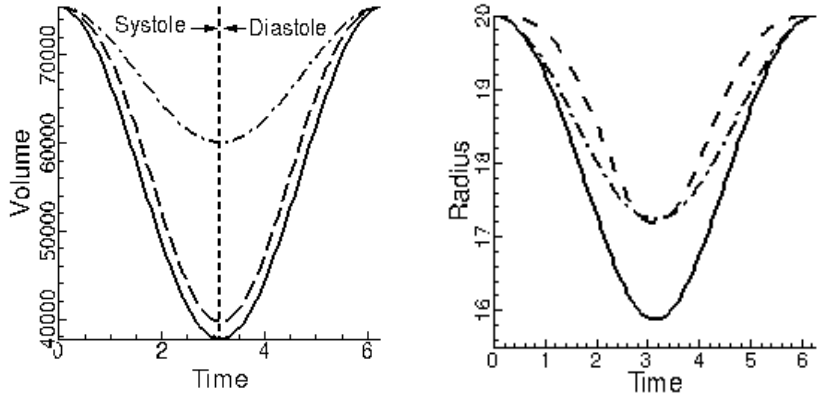

(a) **(b)**

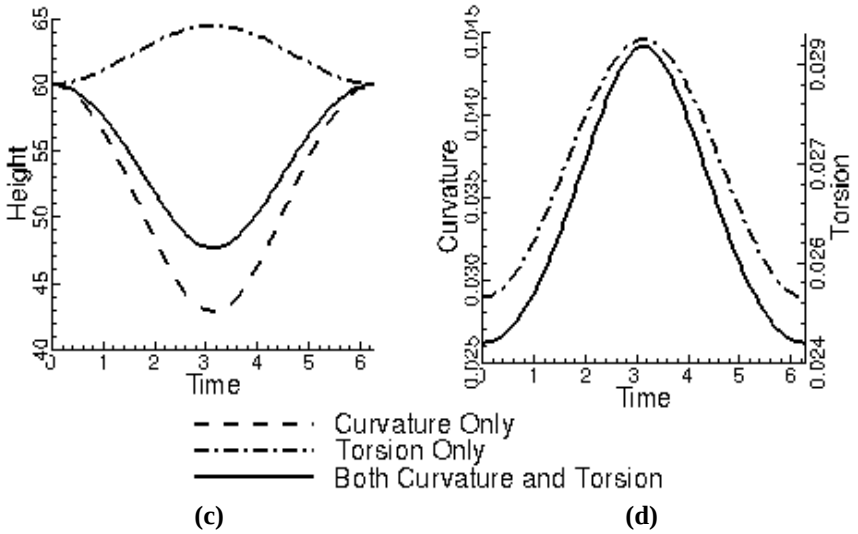

Figure 5.1 Modes of motion: (a) Change in volume of cylindrical heart (b) Change in radius of cylindrical heart (c) Change in height of cylindrical heart. (d) Corresponding change in curvature and Torsion.

In order to investigate the influence of the time dependent change in curvature and torsion of the CA, three different modes of motion are studied. First, the volume of the cylindrical heart is changed as a function of time, holding the ratio of the cylinder radius and height constant. In this mode, both the curvature and torsion of the helix change with time. The other two modes of motion are to change curvature only, holding the torsion constant, and to change torsion only, holding the curvature constant. It should be noted that during these modes of motion, the arc length of the helical tube is preserved, by changing the number of turns of the helix. The change in volume, radius and height of the cylindrical heart is shown in Figs. 5.1a – 5.1c. The corresponding change in curvature and torsion are shown in Fig. 5.1d. The change in volume of the cylinder and the corresponding change in shape of the helix are shown in Fig. 5.2 at six time levels of one half of the cycle for all the three modes of motion. The grid on the surface of the cylinder is shown to indicate the relative motion of the helix on the surface of the cylinder with time. It should be noted that the length of the helix is constant for all modes of motion. The location of a representative plane on which the results in the following sections are shown and the normal vector from this plane to the centerline of the cylinder is also shown in Fig. 5.2.

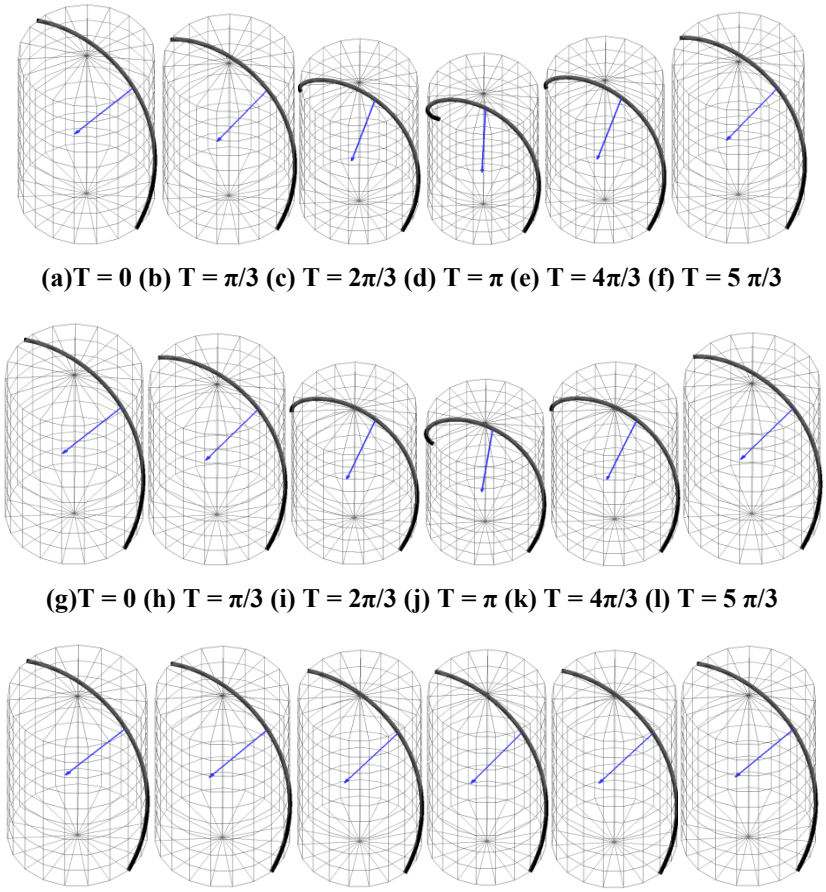

(a)T = 0 (b) T = π/3 (c) T = 2π/3 (d) T = π (e) T = 4π/3 (f) T = 5 π/3

(g)T = 0 (h) T = π/3 (i) T = 2π/3 (j) T = π (k) T = 4π/3 (l) T = 5 π/3

(m)T = 0 (n) T = π/3 (o) T = 2π/3 (p) T = π (q) T = 4π/3 (r) T = 5 π/3

Figure 5.2 Change in helix shape with time at five time levels. Curvature and torsion changes for (a) through (f), curvature changes for (g) through (l) and torsion changes for (m) through (r). Torsion for (g) through (l) is constant at 0.02497 and curvature is 002615, 0.02940, 0.03819, 0.04407, 0.03790 and 0.02940 respectively. The curvature for (m) through (r) is 0.02615 and the torsion is 0.02497, 0.02591, 0.02789, 0.02888, 0.02783 and 0.02591 respectively. For (a) through (f), both curvature and torsion changes with the values from (g) through (r).

The applied representative inlet velocity waveform and the outlet pressure waveform corresponding to observed pulse waveforms for healthy resting conditions are shown in Fig. 4.1 [71]. The applied pulsatile flow combined with the change in volume (Fig. 5.1a) provides a realistic correlation with actual flow conditions experienced by an idealized left main coronary artery. The other parameters pertinent to this study are listed in Table 5.1. The walls of the helical tube are considered to be non-compliant. It should be noted that all the values shown in figures and tables in this work are expressed in non-dimensional terms using the characteristic scales described in this section.

Table 5.1 Properties used for the flow simulation

Parameter	Value
Tube Radius (m)	0.0015
Tube Length (m)	0.1303
Fluid Kinematic Viscosity(m^2s^{-1})	4.6E-6
Fluid Density (kgm^{-3})	1060
Womersley Parameter	1.7531

The Womersley number for this study is 1.7531 and the maximum Reynolds number based on tube diameter is 340. The values used fall within observed physiological variations due to various biological factors. The peak velocity for this Reynolds number is 55.4 units and the near wall grid resolution is 8e-3 units. The temporal discretization used for the calculations was 1e-4 units, selected to maintain the CFL number less than 0.1. Compared to similar studies [56, 73-75, 77, 82] , the grid spacing used in this study is at least two times smaller. The applied velocity and pressure boundary conditions are shown in Fig. 4.1. The convergence criteria for the pressure and momentum equations is set to 10^{-6} at each time step.

Table 5.2 Grid independency study

Level	Number of Cells	Average Shear Stress	%Change
Coarse	153600	13.2639	6.704
Intermediate	256000	14.0761	0.99
Fine	460800	14.2169	0.0

Grid Independency

To check grid independency, three grid levels were tested (coarse, intermediate and fine) where the number of cells in the radial direction was increased by factors of 2 and 4. The inlet velocity waveform and pressure waveform shown in Fig. 4.1 and a static geometry at the start of the cycle, with cylindrical radius of 20 units and circumferential raise of 60 units were used. The fine level was used as the baseline. A difference of less than 1% (Table 5.2) was seen in the area averaged shear stress between the coarse and fine grid levels, thus the intermediate grid level was selected for this study.

Results

In defining the effects of torsion and curvature on flow, it is useful to define the Dean Number and Germano number[83] as shown in Eqs. (5.3) and (5.4).

$$Dn = \mathrm{Re}_D \, \kappa^{0.5} \tag{5.3}$$

$$Gn = \mathrm{Re}_D \, \tau \tag{5.4}$$

In the above equations, the Reynolds number is defined based on tube diameter and the applied mean flow velocity at the inlet. Here the Dean Number is a measure of the centrifugal forces and the Germano Number is a measure of twisting forces. The Dean number is a direct measure of the product of the centrifugal forces and the inertia forces, normalized by the viscous forces or the effect of the curvature on the flow. Similarly, the Germano number is a direct measure of the ratio of the twisting forces to the viscous forces or the effect of the torsion on the flow. A third non-dimensional number was defined by Liu et al.[83] for large Dean Numbers, as shown in Eq. (5.5).

$$\gamma = \frac{Gn}{Dn^{1.5}} \tag{5.5}$$

The above parameter defines the relative importance of centrifugal forces to the twisting forces. When the above parameter is large, the contribution of centrifugal forces on the flow is relatively less important.

Parameters Studied

To study the effect of the dynamic change in curvature and torsion, first the flow characteristics in the stationary helical tube with the curvature fixed at 0.02615 and the torsion at 0.02497 is presented, that correspond to the curvature and torsion at the start of systole. This is followed by the presentation of a comparison of flow characteristics of a moving helical tube for all three modes of motion studied in this work (Fig. 5.2). It should be noted that in Figs 5.5 -5.10, the inner wall is the side of the helix that is in contact with the cylindrical heart at all instances and the wall diametrical opposite to the inner wall is termed as the outer wall. The inner wall is located at the lower end of the vertical axis of Figs 5.5-5.10 and the outer wall is the upper end, as shown in the inset in Figs 5.5-5.7. The same convention is applicable to Figs. 5.8-5.10.

In the following paragraphs, results from four sets of simulations are presented – stationary helical tube subject to pulsatile flow, change in curvature, change in torsion, and change in both curvature and torsion. For each of these simulations, the following parameters are tracked.

- Axial velocity
- Pressure
- Secondary Stream function
- Wall Shear Stress and Oscillatory Shear Index

The organization of the following sections is as follows. First the results for the baseline pulsatile flow in a stationary helical tube are presented. This is followed by the comparison of the flow field for the three modes of motion with each other and the stationary case. Finally the effect of this motion on Wall Shear Stress and Oscillatory Shear Index are presented. It should be noted that Figs. 5.5-5.10 and Fig. 5.11 show representative values of the parameters presented on a plane at the middle of the helical tube (44a). The location of this representative plane and the normal vector from this plane to the centerline of the cylinder is shown in Fig. 5.2.

Pulsatile Flow in a Stationary Helical Tube

In this section, the flow characteristics of pulsatile flow in the helical tube fixed at the start of the cycle is presented, with the aim to isolate the effect of the pulsatile boundary conditions on flow. Fig.5.3 shows the variation of the axial velocity profile at six time levels through the cycle, at 44a from the inlet, where 88a is the total length of the helical tube. The corresponding value of the parameter γ is given below each of the figures. The γ parameter for this stationary helix changes purely due to change in Reynolds number, isolating the effects of pulsatile flow. At the start of the cycle, T = 0.0, when γ is the highest, due to the relatively smaller effects of centrifugal forces, the velocity profile is symmetrical. As γ decreases, the velocity profile tends to move towards the outer wall due to the increased effects of centrifugal forces, as seen in Fig. 5.3b compared to Fig. 5.3c. A further decrease in γ leads to the maximum velocity moving further towards the outer wall and creating a flatter maximum velocity profile (Fig. 5.3d, Fig.

5.3e). This flattening of the parabolic profile increases as the effects of the centrifugal forces increase.

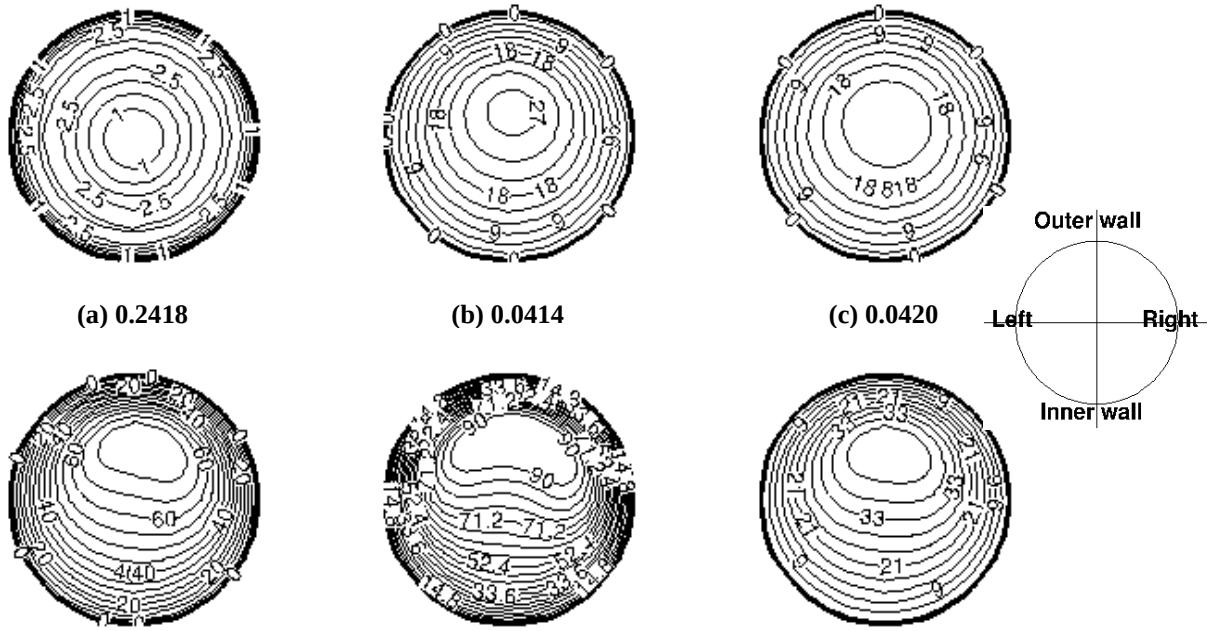

(a) 0.2418 **(b) 0.0414** **(c) 0.0420**

(d) 0.0238 **(e) 0.0215** **(f) 0.0396**

Figure 5.3 Variation of axial velocity profile at 44a from inlet of helical tube at six time values (a) T = 0.0 (b) T = 1.05 (c) T = 2.1 (d) T = 3.15 (e) T = 4.2 (f) T = 5.25. The values below the figures are the non-dimensional parameter γ as defined in Eq. (13). The helical tube is stationary.

Fig. 5.4 shows the variation of pressure at 44a from the inlet of the helical tube. The values shown are obtained by setting the centerline pressure to zero. It is seen that the value of pressure away from the center increases as γ decreases, reaching a maximum at T = 4.2. When γ is large, the pressure isobar lines are horizontal but bent at the inner and outer walls. When the centrifugal forces are higher (for small γ) the pressure lines vary sharply in the horizontal direction and negligibly in the vertical direction. Similar observations were made by Liu et al. [83].

A decrease in cross-plane pressure difference at higher γ values indicates a corresponding decrease in secondary flow effects due to centrifugal forces. This is seen in Fig.5.5, which shows the contours of the stream function with time. This stream function is defined only in the r-θ (2D cross-sectional coordinates) at that instant in time.

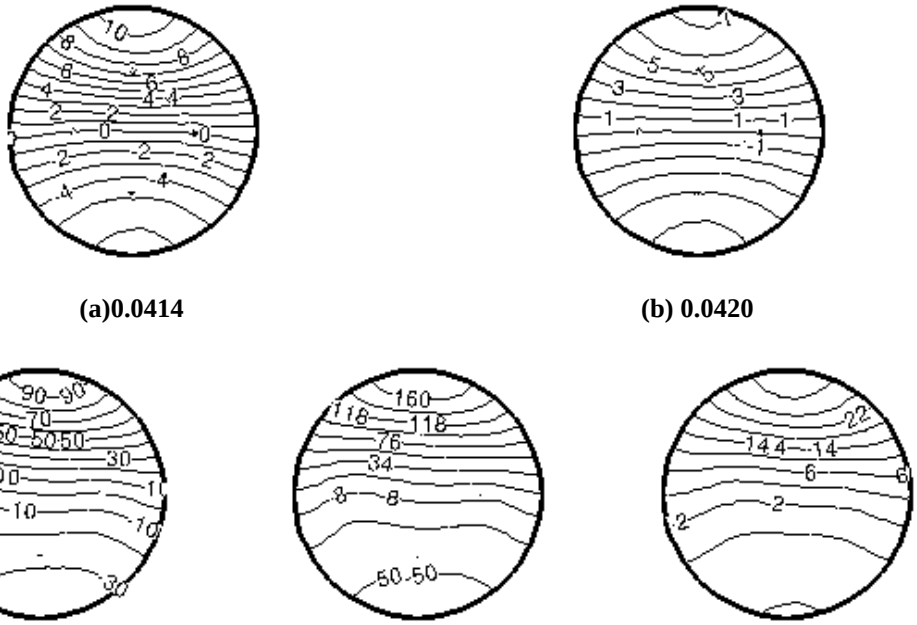

Figure 5.4 Variation of pressure at 44a from inlet of helical tube at six time values (a) T = 1.05 (b) T = 2.1 (c) T = 3.15 (d) T = 4.2 (e) T = 5.25. The values below the figures are the non-dimensional parameter γ as defined in Eq. (13). The helical tube is stationary.

When γ is large, the secondary stream lines are symmetrical, with the dividing line of the two vortices being vertical. As seen in Fig.5.5a, the flow consists of a pair of counter-rotating helical vortices, placed symmetrically with respect to the plane of symmetry. This secondary flow pattern is known to form due to the centrifugally-induced pressure gradient, driving the slow moving fluid near the wall inside and the faster fluid from the center to the outside. When the Reynolds number is small, the secondary flow induced by the centrifugal forces due to the curvature is small. With the decrease in γ parameter, the secondary and axial boundary layers develop. Similar observations were made by Yamamoto et al. [84]. It is also seen that the secondary streamlines become denser near the wall and sparser near the center of the flow as Reynolds number increases or as γ decreases.

(a) 0.2418 **(b) 0.0414** **(c)0.0420**

(d) 0.0238 **(e) 0.0215** **(f) 0.0396**

Figure 5.5 Secondary flow patterns at 44a from inlet of helical tube at six time values (a) T = 0.0 (b) T = 1.05 (c) T = 2.1 (d) T = 3.15 (e) T = 4.2 (f) T = 5.25. The values below the figures are the non-dimensional parameter γ as defined in Eq. (13). The helical tube is stationary.

From these observations, the importance of the γ parameter is seen. Figs. 5.3-5.5 represent the isolated effects of the pulsatile flow conditions. These observations are used below to compare and contrast the effects of the applied motion on the flow and their corresponding hemodynamic implications.

Pulsatile Flow in a Moving Helical Tube

It should be noted that all the figures presented in this section do not include the flow parameter at the start of the cycle, due to the fact that the behavior is similar to the stationary case, presented above.

Fig. 5.6 compares the axial velocity profiles at 44a from the inlet of the helical tube at five time levels for all three modes of motion studied in this work. The γ parameter is the smallest at all times when the curvature changes and is the highest when the torsion changes. A decrease in γ parameter moves the velocity profile towards the outer wall.

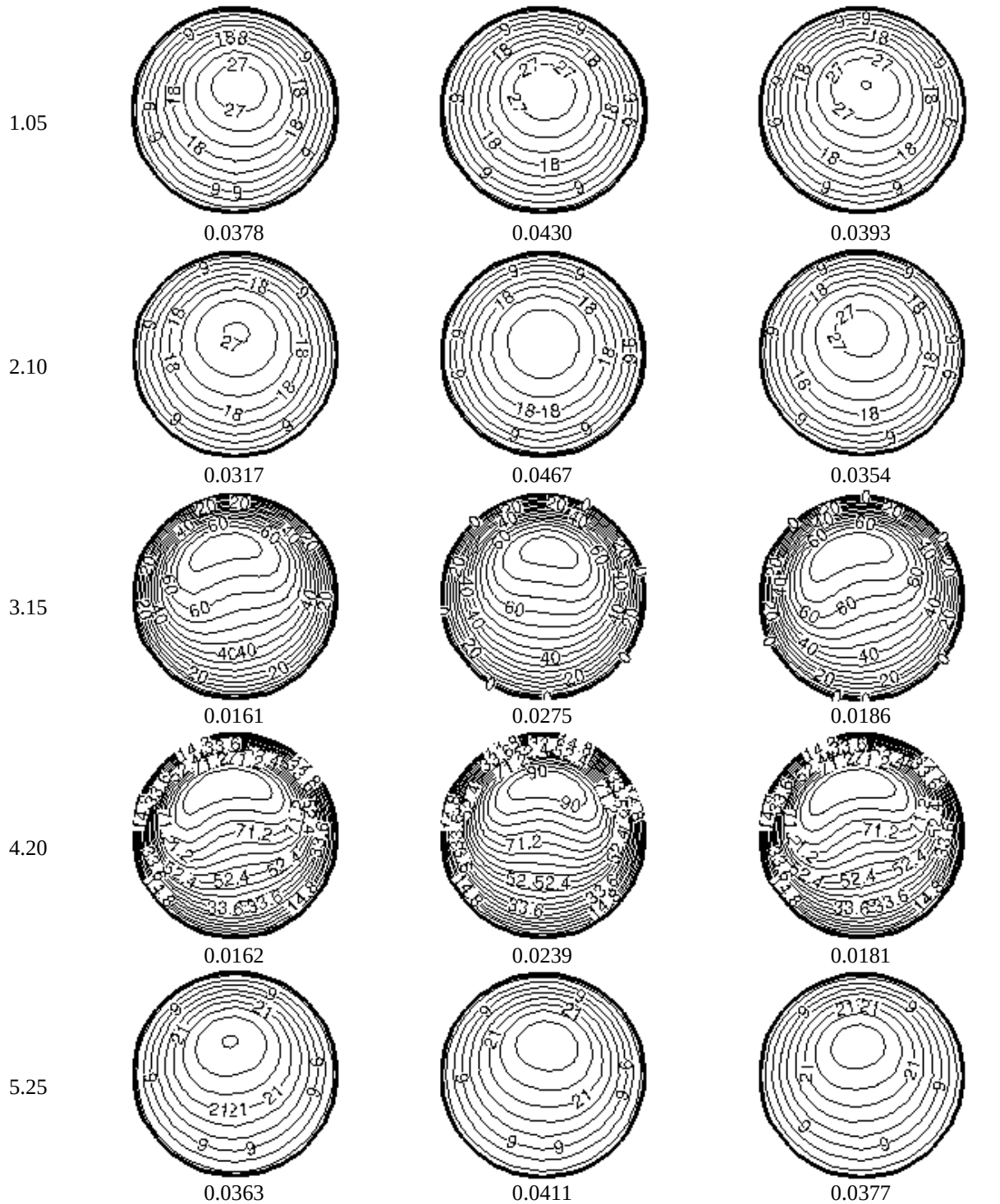

Figure 5.6 Comparison of axial velocity profiles at five time levels at 44a from inlet. The corresponding γ parameter is shown below each figure

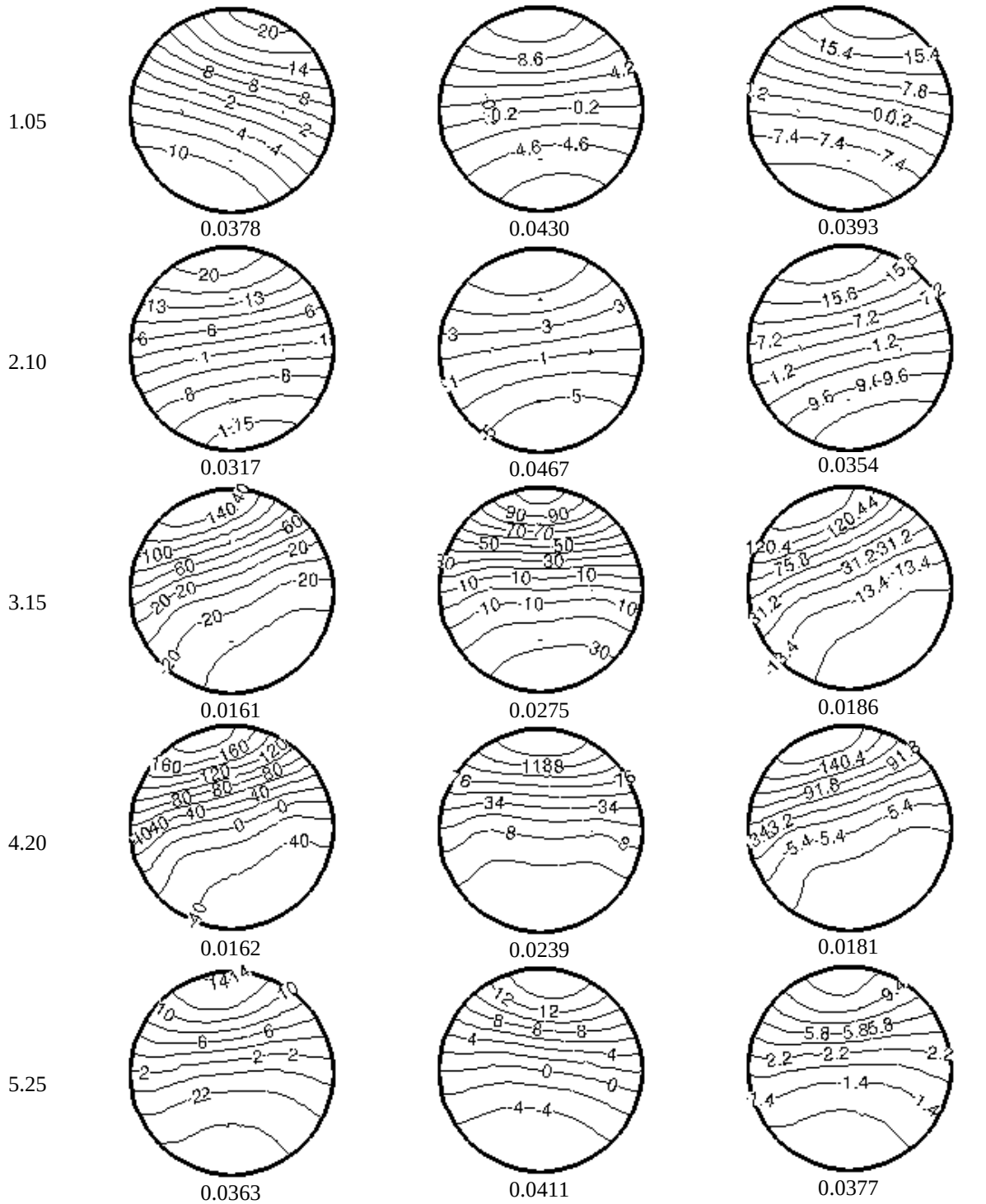

Figure 5.7 Comparison of pressure distribution at five time levels at 44a from inlet. The corresponding γ parameter is shown below each figure.

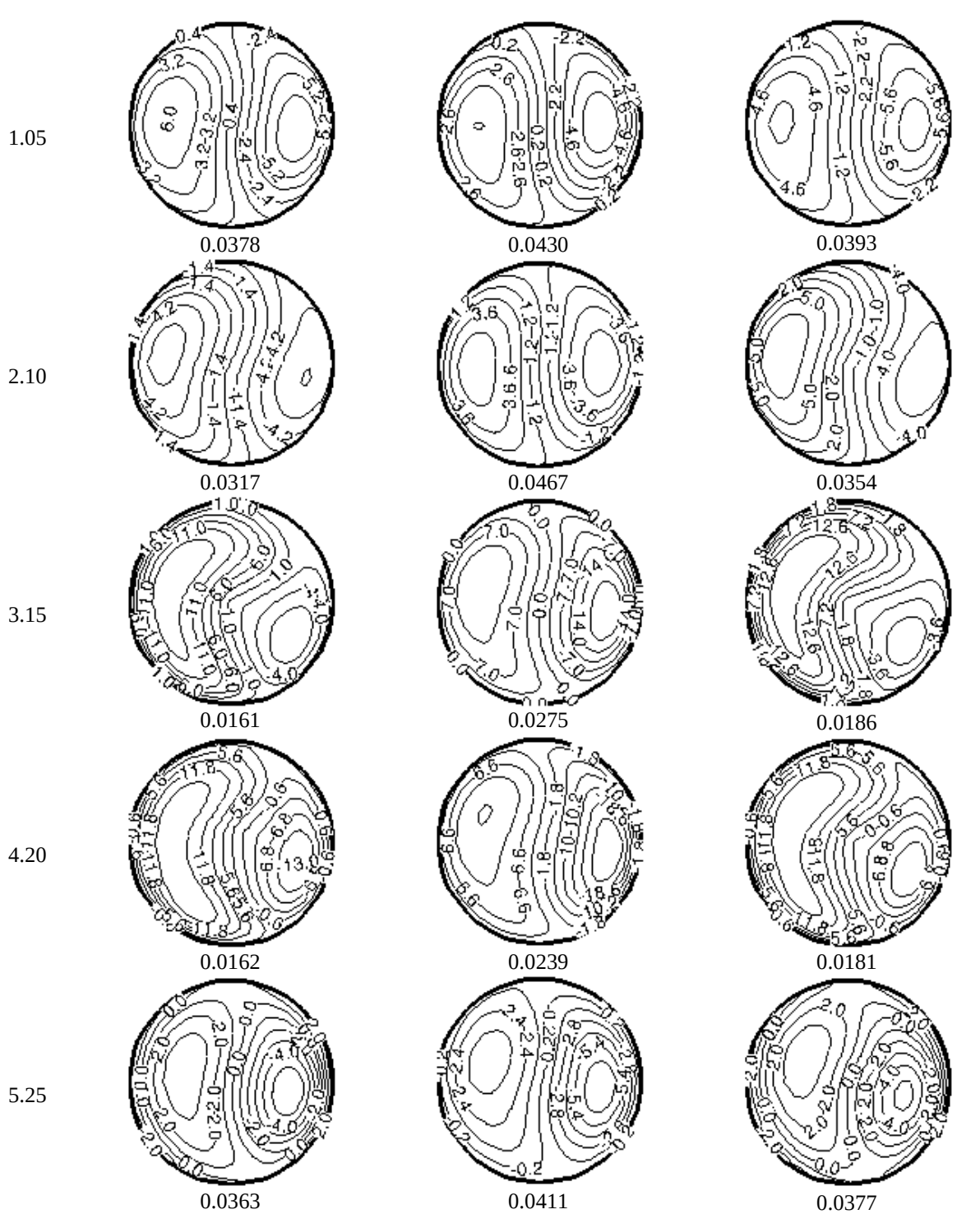

Figure 5.8 Comparison of stream function contours at five time levels at 44a from inlet. The corresponding γ parameter is shown below each figure.

At T = 1.05, the axial profile is similar to the stationary case for all modes of motion, due to the similar values of the γ parameter, with a maximum velocity of 27 units. At T = 2.1, the axial velocity is higher when the curvature changes compared to the stationary case (Fig. 5.3c) and when torsion changes. The relatively increased effect of curvature leads to this higher axial velocity profile. The velocity profile is more parabolic when only the curvature changes, compared to the other two modes of motion. Similar increased effects of centrifugal forces are seen at other time levels, where the parameter γ is lower than the stationary case. With increasing curvature (or decreasing γ), the velocity profile moves closer to the wall and becomes flat. For the modes of motion where the curvature changes, the velocity profile is rotated about the vertical axis due to the dynamic movement of the helical tube. When γ is large, the flow is dominated by the twisting forces, leading to more symmetrical axial velocity and secondary flow distributions. When γ is small, the flow is dominated by the centrifugal forces, leading to asymmetrical axial velocity profiles. These changes in axial velocity profiles with γ affect the variation of wall shear stress along the circumference of the tube, as shown in the sections that follow.

Fig. 5.7 shows the comparison of cross-plane variation of pressure, with the pressure at the center of the plane set to zero. It is seen that the value of pressure away from the center increases as γ decreases, the maximum being for T = 4.2, as seen for the stationary case. The pressure isobar lines are horizontal but bent at the inner and outer walls as with the stationary case. It is seen that for all time levels the pressure differential levels are higher towards the outer wall. The effects of the rotation of the flow due to the dynamic motion of the helical tube are seen with the rotation of the vertical axis of the pressure at different time levels shown, as the curvature changes (columns 1 and 3). At the time levels shown, the cross plane values are higher when the curvature changes and lowest when the torsion change. In fact, the pressure values are lower than the stationary case, when the torsion changes. When torsion changes, due to the larger γ parameter values, and thus increased twisting forces and reduced centrifugal forces, the pressure difference is smaller than the other modes of motion. It can be seen that torsion change

tends to reduce the cross plane pressure gradients, as evident when comparing the stationary case (Fig. 5.4) and the change in torsion (second column, Fig. 5.7). Clearly, the motion of the helical tube affects the cross-plane pressure difference.

Fig. 5.8 compares the contours of the secondary stream function values for all three modes. In all plots of secondary stream functions, when the stream function levels are same, the normal fluid flow rate represented by this stream function is the same. Thus stream function contours that are densely packed indicate higher fluid transport in the normal direction. Also a higher stream function value indicates higher secondary flow strength and a positive value indicates a counter clockwise rotating flow.

At T = 0.0, as seen with the stationary case, the two vortices are symmetrical for all modes of motion. At T = 1.05, the secondary flow pattern is similar to the stationary case, but the vortex strength is higher due to the increased centrifugal forces, indicated by higher values of stream function, when the curvature changes (columns 1 and 3). At T = 2.1, γ decreases with curvature change and increases with torsion change. The decrease in γ with change in curvature leads to a decrease in symmetry of the two vortices. A further decrease of γ leads to the formation of a dominant vortex. As the γ parameter decreases, boundary layers develop on the wall, with the fluid entering the boundary layers near the outer wall and leaving near the inner wall. An increase in Dean Number or decrease in γ parameter, the circumferential velocity increases, leading to more fluid being transported into the boundary layers at the outer wall. This leads to the thinning of the boundary layer near the outer wall and thickening of the boundary layers near the inner wall. Also, the location of maximum circumferential velocity moves nearer to the outer wall. The two vortices become skewed by the adjustment of the secondary boundary layer, as seen in column 1 and 3, rows 3 and 4. It should also be noted that the secondary stream function values are higher at all times compared to the stationary case and the stream lines corresponding to the dominant vortex are positive when the curvature changes.

As seen from Fig. 5.5 and Fig. 5.8, at large γ values, the circumferential velocity is high at both the left and right sides and the two vortices are symmetrical. When the torsion changes, it is seen that the streamlines are denser than the stationary case, indicating

higher fluid transport. As the torsion increases, the effect of the twisting forces increases, thus even though the centrifugal forces are not dominant, the secondary flow strength still increases. For high γ values, the circumferential velocity term is dominated by the twisting forces, thus if the torsion effects are strong enough, the secondary flow pattern will become swirl-like. At T = 2.1, when both curvature and torsion changes, the positive stream function values are higher and the negative stream function values are lower, than when curvature changes, indicating an increase of the counter-clockwise rotating secondary flow strength and a decrease of the clockwise rotating secondary flow strength. This effect is seen to a greater extent at T = 3.15 and T = 4.2. This point to the effects of the twisting forces, that tend to offset the effects of the change in centrifugal forces. This conclusion agrees qualitatively with that of Liu et al. [83], who concluded that the centrifugal velocities depend on the opposing effects of twisting and curvature.

Effect of Dynamic Change in Curvature and Torsion on Hemodynamic Parameters

Variation of time averaged wall shear stress (WSS) as defined in Eq. (5.6) with respect to the stationary helical tube, along the circumference is shown in Fig. 5.9, at six axial positions from the inlet. This change in WSS with respect to the stationary case is the polar radial distance from the center of each plot. The corresponding maximum and minimum percentage change in WSS with respect to the stationary helical tube, for all three moving helical tubes is shown in Table 5.3.

$$WSS = \frac{1}{\Omega^2}\left(\frac{\partial v_s}{\partial r}\right) \qquad \textbf{5.6}$$

$$OSI = 0.5\left(1 - \frac{\left|\int_0^T \tau_w dt\right|}{\int_0^T |\tau_w| dt}\right) \qquad \textbf{5.7}$$

The WSS values are higher at or near the outer wall compared to the inner wall, due to skewing of the axial velocity profiles caused by the centrifugal forces, for all modes of motion studied in this work, including the stationary helical tube. This points to the

prominent effect of curvature on the flow, as evident from the low values of the γ parameter (<1), for all cases in the current study. Also, it is noticed that the difference in wall shear stress values at all locations is higher when the curvature changes, either individually or in conjunction with the torsion. It is also seen that with increasing distance from the inlet, the location of the maximum and minimum WSS rotates counterclockwise, with an increase in the maximum and minimum WSS difference. This points to the localized dynamic rotation effects due to the motion.

Table 5.3 Maximum and minimum percentage change in time averaged WSS with respect to the stationary helical tube

Position	Curvature Only		Torsion Only		Curvature and Torsion	
	Minimum	Maximum	Minimum	Maximum	Minimum	Maximum
18a	-5.76	11.03	-0.32	0.66	-4.27	12.59
32a	-7.17	11.16	-0.36	0.46	-6.36	13.75
44a	-8.71	12.55	-1.30	1.22	-8.69	15.98
58a	-10.74	15.59	-2.04	1.76	-11.29	19.50
70a	-12.60	18.88	-2.73	2.24	-14.05	23.03
84a	-14.49	22.16	-3.22	2.78	-16.67	26.45

Table 5.4 Maximum and minimum percentage change in OSI with respect to the stationary helical tube

Position	Curvature Only		Torsion Only		Curvature and Torsion	
	Minimum	Maximum	Minimum	Maximum	Minimum	Maximum
18a	-12.05	9.63	0.50	3.48	-11.31	8.65
32a	-12.22	12.22	0.91	3.03	-12.69	11.68
44a	-13.11	14.12	1.33	2.44	-14.56	14.59
58a	-15.68	17.19	0.76	2.97	-17.26	18.51
70a	-18.16	20.90	0.31	3.57	-20.15	23.52
84a	-20.61	24.33	-0.26	4.28	-22.87	28.15

The oscillatory shear index (OSI) is defined in Eq. (5.7) [85]. The circumferential variation of OSI at six locations is shown in Fig. 5.10. The corresponding maximum and minimum percentage change in OSI with respect to the stationary helical tube, for all three moving helical tubes is shown in Table 5.4. For all modes of motion, the OSI is higher at or near the inner wall compared to the outer wall. As the distance from the inlet increases, the location of the maximum and minimum OSI values rotates

counterclockwise, as with WSS (Fig. 5.9). Thus, the movement of the helical tube with change in torsion or curvature or both leads to changes in WSS and OSI. WSS changes by a maximum of 22% when curvature changes, by 3% when torsion changes and by 26% when both curvature and torsion changes. OSI changes by a maximum of 24% when curvature changes, by 4% when torsion changes and by 28% when both curvature and torsion changes.

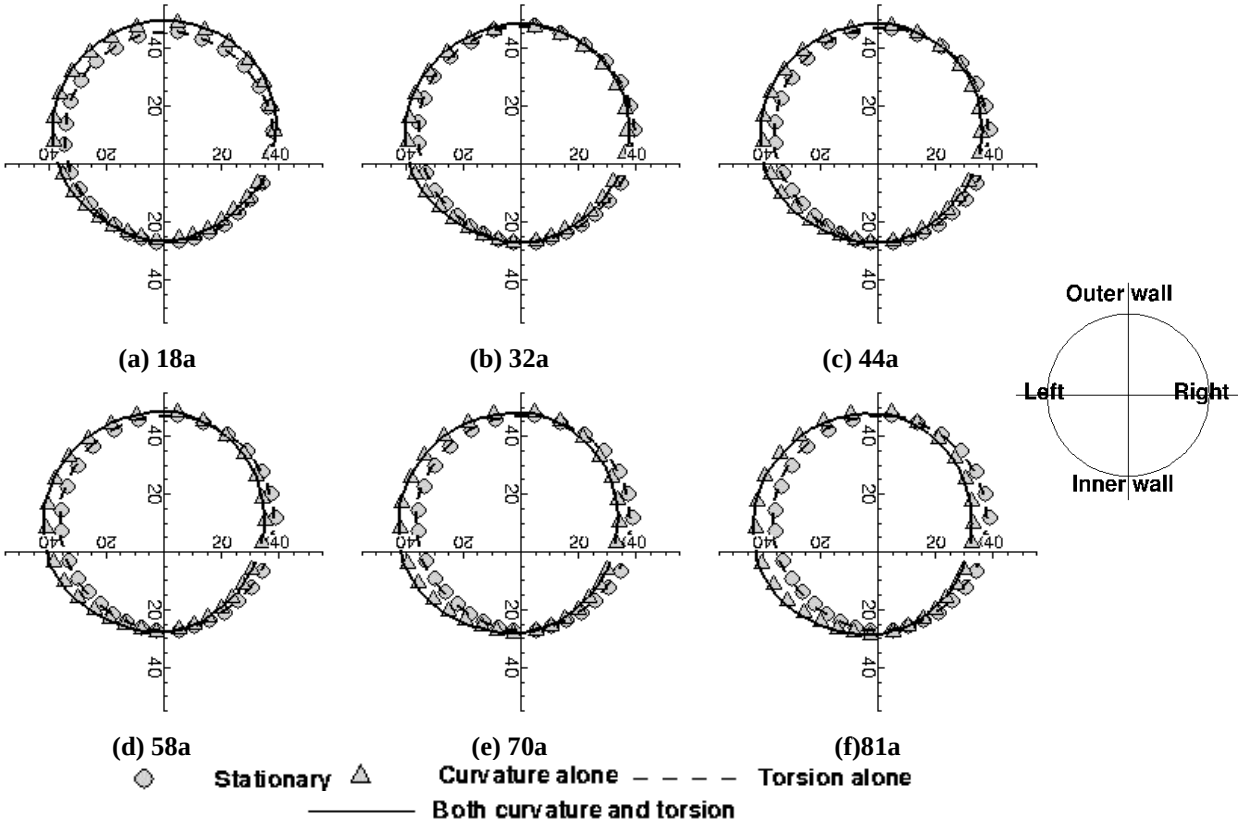

Figure 5.9 Change in time averaged WSS with respect to the stationary helical tube.

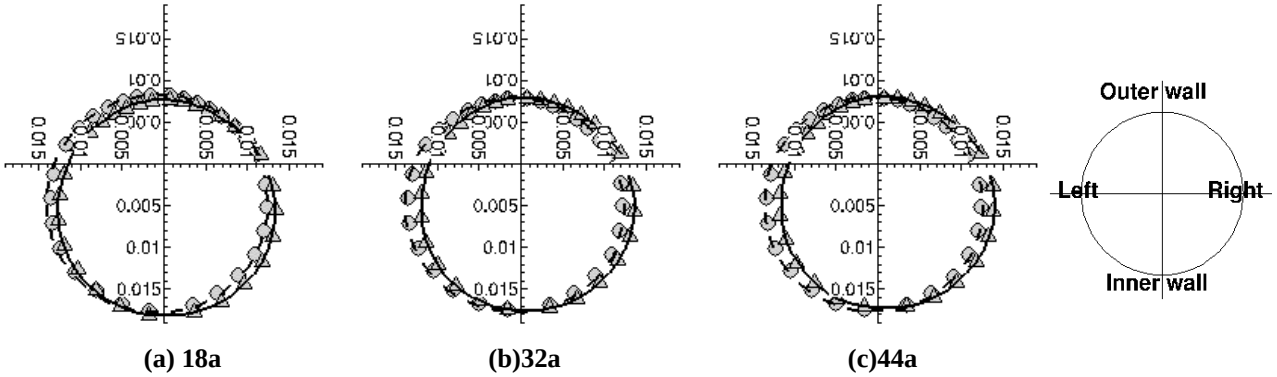

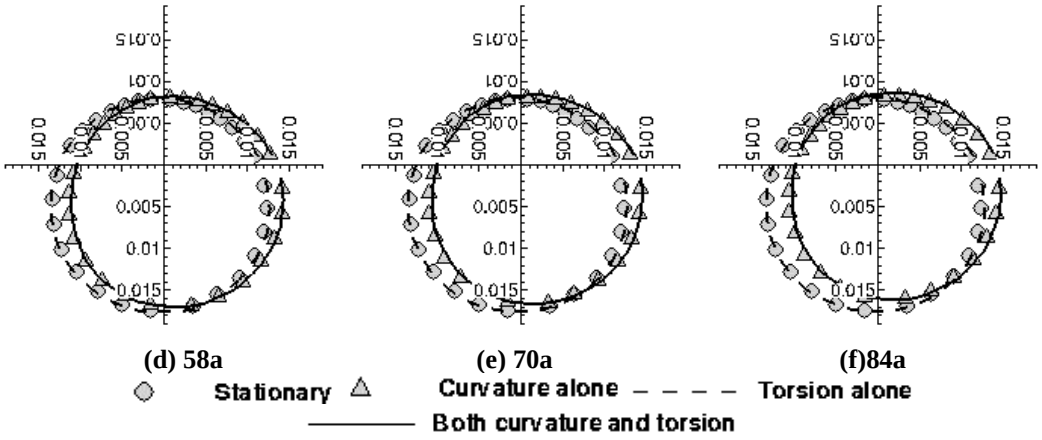

Figure 5.10 Change in OSI with respect to the stationary helical tube.

Discussion

The above results demonstrate that the change with time in curvature and torsion, either independently or together, due to the movement of the helical tube causes changes in axial velocity and secondary flow patterns. Changes in the cross plane pressure difference are found to be affected by both curvature and torsion. It is also found that the hemodynamic parameters are affected by the dynamic change in curvature and torsion, with curvature playing a dominant role.

Relevance to Hemodynamics

From the extensive studies available in the literature [51-54], it can be concluded that local non-uniform hemodynamics triggers abnormal biological events. Here, we highlight the observed variations in WSS and OSI shown in Figs. 5.9 and 5.10. The wall shear stress at all locations and for all modes of motion is higher at the outer wall and smaller on the inner wall. As the distance from the inlet increases, the WSS becomes higher on the left wall compared to the right wall, due to shifting of the axial velocity profile caused by secondary flow vortices, when the curvature changes. This is a consequence of the increased centrifugal forces. A change in torsion leads to a higher WSS compared to the stationary helical tube. It is known[53, 54] that a lower WSS values lead to intimal thickening and this corresponds to observed wall thickness values being higher at the inner wall of curved arteries, which correspond to the values obtained in this study.

The OSI values are higher on the inner wall than the outer wall for all locations and for all modes studied. As the distance from the inlet increases, the OSI becomes higher on the right wall compared to the left wall, due to shifting of the axial velocity profile caused by secondary flow vortices, when the curvature changes.

Physical Mechanism – Vorticity Production at the Wall Due to Motion

In trying to understand the physical mechanism responsible for changes in flow patterns and the relationship between secondary flow patterns and WSS, the source of vorticity or vorticity flux density is used. The role of vorticity (curl of velocity vector) in explaining the fluid dynamic phenomena is well established, starting with the work by Lighthill [80], who pointed out that solid boundaries act as distributed sources of vorticity. Extending Eqs (4.5-4.6) to moving helical tubes, with a nontrivial finite wall velocity, we write the orthogonal axial velocity momentum equation in terms of the vorticity components in the radial and circumferential directions, at the wall, shown in Eq. (5.8).

$$\underbrace{-\frac{1}{\Omega^2}\left(\frac{1}{r}\frac{\partial \omega_r}{\partial \theta}-\frac{\partial \omega_\theta}{\partial r}\right)}_{\text{Vorticity flux density}}=\underbrace{\frac{\partial v_s}{\partial t}}_{\text{Unsteady term}}$$
$$+\underbrace{\left(\frac{v_s}{\left(1+\kappa r\sin\theta\right)}\frac{\partial v_s}{\partial s}+v_r\frac{\partial v_s}{\partial r}+\frac{v_\theta}{r}\frac{\partial v_s}{\partial \theta}\right)+\frac{\kappa v_s}{\left(1+\kappa r\sin\theta\right)}\left(v_r\sin\theta+v_\theta\cos\theta\right)}_{\text{Convective term}} \qquad \textbf{5.8}$$
$$+\underbrace{\frac{1}{\left(1+\kappa r\sin\theta\right)}\frac{\partial p}{\partial s}}_{\text{Pressure gradient}}-\underbrace{\frac{1}{\Omega^2}\left(\frac{\partial}{\partial r}\left\{\frac{\partial v_s}{\partial r}+\frac{\kappa v_s}{\left(1+\kappa r\sin\theta\right)}\sin\theta-\frac{1}{\left(1+\kappa r\sin\theta\right)}\frac{\partial v_r}{\partial \theta}\right\}\right)}_{\text{Diffusion term}}$$

In the above equation, the left hand side is defined as the vorticity flux density at the wall. The radial and circumferential vorticity components are defined in Eq. (5.9).

$$\omega_r=\frac{1}{r\left(1+\kappa r\sin\theta\right)}\left(\frac{\partial}{\partial \theta}\left(\frac{v_s}{1+\kappa r\sin\theta}\right)-\frac{\partial}{\partial s}\left(rv_\theta\right)\right)$$
$$\omega_\theta=\frac{1}{\left(1+\kappa r\sin\theta\right)}\left(\frac{\partial}{\partial s}\left(v_r\right)-\frac{\partial}{\partial r}\left(\frac{v_s}{1+\kappa r\sin\theta}\right)\right) \qquad \textbf{5.9}$$

In Eq. (5.8), all the terms other than the pressure gradient term are based on the wall movement velocities. For the different modes of motion studied the combined wall

movement velocity terms and the pressure gradient term are of the same order of magnitude.

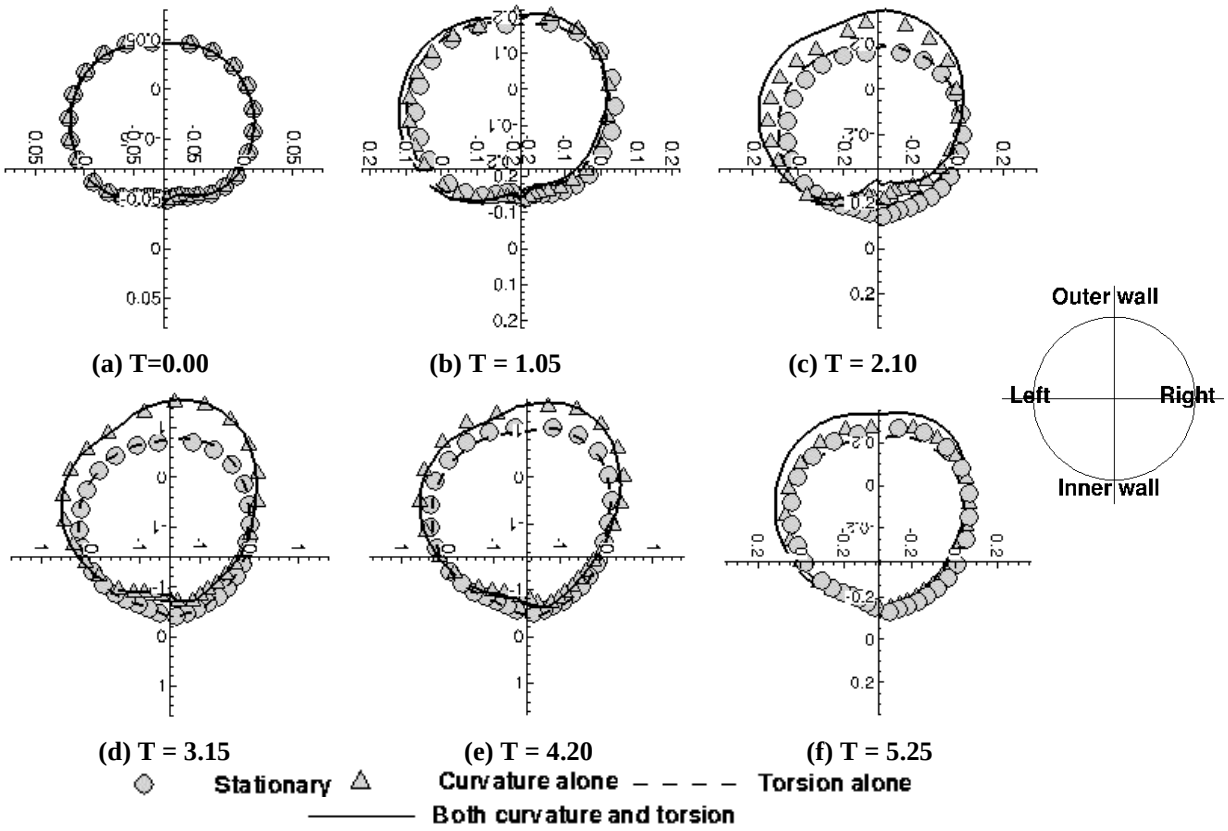

Figure 5.11 Variation of Vorticity Flux at 44a, at (a) T = 0.0 (b) T = 1.05 (c) T = 2.10 (d) T = 3.15 (e) T = 4.20 (f) T = 5.25.

The variation of vorticity flux density at the wall, at 44a from the inlet of the helical tube at six instances in time is shown in Fig. 5.11. At the start of the cycle, the vorticity flux distribution is symmetrical about the vertical axis, with positive maximum and negative minimum vorticity flux occurring at the outer and the inner walls. Comparing the vorticity flux density at the wall (Fig. 5.11a) with the secondary flow patterns presented in the previous section (Fig. 5.8, row 1), it becomes apparent that the vorticity flux density provides a means to explain the observed flow patterns. It should also be noted that the γ parameter for all the modes studied in this work at the start of the cycle are identical (γ = 0.2418).

At T = 1.05, vorticity flux is negative for all modes at the inner wall. It is also seen that the vorticity flux density is higher on the left side of the vertical axis, as indicated by the higher area between the curve to the left and the vertical axis. A change in curvature

leads to a decrease in vorticity flux on the right side of the vertical axis and a seemingly corresponding increase in vorticity flux on the left side of the vertical axis. This shift of the vorticity flux to the left further increases when both the helical tube curvature and torsion changes. When torsion changes, the vorticity flux density values is higher than the stationary helical tube. It is also seen that the line connecting the maximum and minimum vorticity fluxes, which corresponds to the direction of the centrifugal forces, rotates clockwise. This rotation is larger when the curvature changes .This corresponds well with the observed secondary flow patterns, where the vortex strength on the left of the vertical axis is higher than on the right for all modes of motion. As indicated by the stream function values in Fig 5.8 (column 3, row 1), the vortex strength is higher for all modes studied in this work on both sides of the vertical axis when both the curvature and torsion change.

At T = 2.1, for the stationary helical tube and for the motion with change in torsion, the vorticity flux density is symmetrical about the vertical axis. The vorticity flux density is higher by about 10% for the case with torsion change. The maximum and minimum vorticity flux density line rotates further clockwise when the curvature changes, and the vorticity flux density distribution is dominant on the left side of the vertical axis. These observed vorticity flux density distributions explain well the symmetrical secondary flow patterns (Fig. 5.6c, Fig. 5.8 row 2) for high γ parameter values and skewed flow patterns for low γ parameter values. Similar conclusions can be drawn by comparing vorticity flux density distributions at the other times presented in Fig. 5.11 and the secondary flow patterns in Fig 5.8.

Vorticity Flux Density and WSS

The wall shear stress is related to the vorticity at the wall as shown in Eq. (5.10), thus pointing to a relationship between the secondary flow patterns and the wall shear stress through vorticity.

$$\omega_w \times n = \Omega^2 \tau_w \qquad \textbf{5.10}$$

Here ω_w is the wall vorticity vector and n is the wall normal unit vector. Fig 5.12 shows the time averaged wall vorticity flux density at six locations from the inlet for all the cases studied in this work. Comparing these values with the observed WSS and OSI values(Fig. 5.9 and 5.10), we see that the left dominance of the secondary flow patterns affect the shear stress distributions on the wall, leading to a higher WSS and OSI values on the left side of the vertical axis. It can be seen that the outer wall acts as a source and the inner wall of the helix acts as a sink of vorticity. Thus from the above discussion (vorticity flux production and secondary flow patterns), it can be seen that the vorticity produced due to the movement of the helical tube, would directly affect the wall shear stress and influence endothelial response.

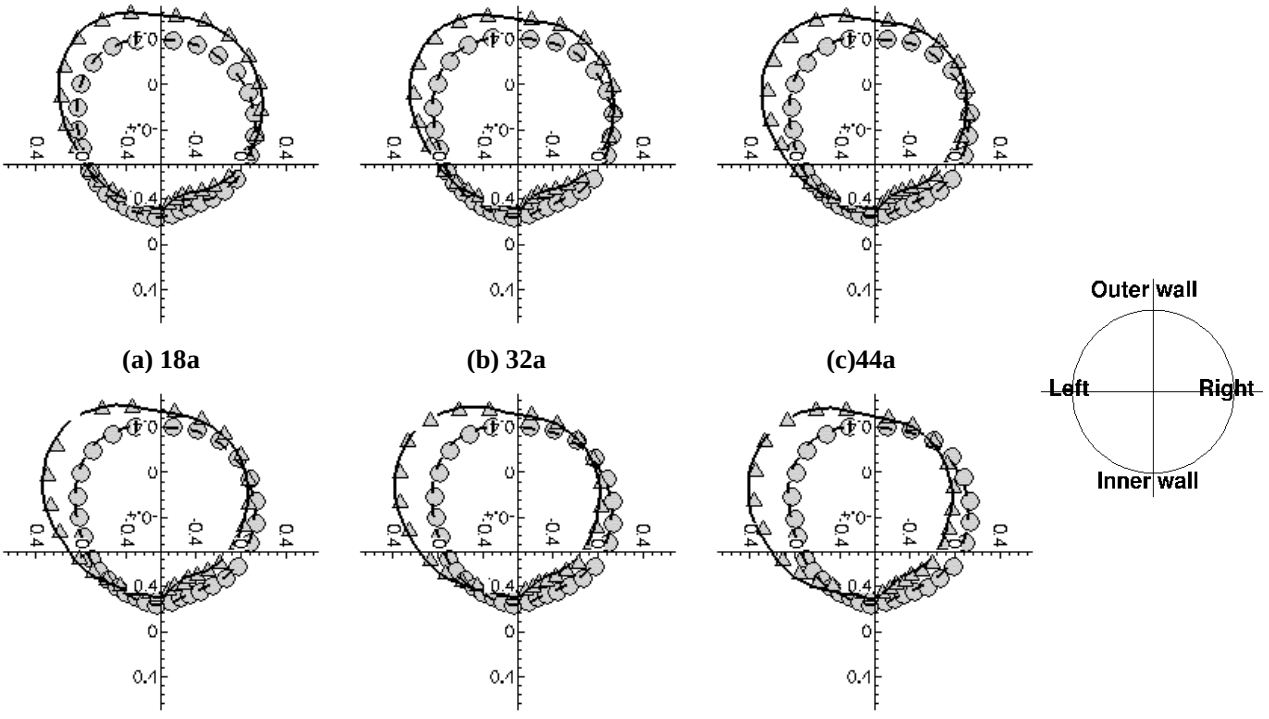

(a) 18a **(b) 32a** **(c)44a**

(d) 58a **(e) 70a** **(f) 84a**

Figure 5.12 Variation of time averaged Vorticity Flux.

Effect of Change in Curvature and Torsion

From the definition of the γ parameter (Eq. (5.11)), it can be concluded that when γ is large, the twisting forces dominate, leading to a swirl like flow and when γ is small, the centrifugal forces dominate leading to a two vortex torus like flow[83]. The increase in torsion tends to lead to a flow that is less affected by vorticity flux density at the wall, as seen in Figs 5.11 and 5.12. The vorticity flux density for the motion with change in torsion does not change much when compared to the stationary case (10%), where the curvature remains the same for both the cases. As seen from Eq. (5.10), shear stress depends directly on the vorticity vector (or the vorticity flux density), thus the hemodynamic effects (WSS and OSI) due to the change in curvature are dominant when compared to torsion change. Hence, it is concluded that the vorticity flux density plays an important role in explaining physical mechanisms that lead to the observed secondary flow patterns.

Conclusion

Three-dimensional CFD calculations have been performed for pulsatile flow with moving wall boundaries in simplified coronary arteries, using physiologically relevant flow waveforms, with the objective of studying the effect of change of curvature and torsion on the local hemodynamics. The curvature and torsion of the stationary helical tube, which is used as the baseline case was set to 0.0262 and 0.025 respectively. Three modes of motion were studied. The first mode was to change the curvature, the second mode was to change the torsion and the third mode of motion was to change both curvature and torsion. This change in curvature and torsion was effected to mimic the movement of an idealized heart on which the simplified artery rests. It was observed that the changes in observed flow patterns can be explained by the time dependent γ parameter. When γ is large, the flow is dominated by the twisting forces, leading to more symmetrical axial velocity and secondary flow distributions. When γ is small, the flow is dominated by the centrifugal forces, leading to asymmetrical axial velocity profiles. Secondary flow patterns exhibit a dominant vortex on the left side of the vertical axis. The movement of the helical tube with change in torsion or curvature or both leads to changes in WSS and OSI. WSS changes by a maximum of 22% when curvature changes, by 3% when torsion

changes and by 26% when both curvature and torsion changes. OSI changes by a maximum of 24% when curvature changes, by 4% when torsion changes and by 28% when both curvature and torsion changes. We have demonstrated that these changes are attributed to the physical mechanism associating the secondary flows to the production of vorticity (vorticity flux) due to the wall movement. Subsequently, these secondary flow patterns and augmented vorticity flux density affects the wall shear stresses.

6. Hemodynamic Effects of Compliance Mismatch in Moving Coronary Arteries

Introduction

The effect of compliance mismatch in stented arteries, under the influence of motion of the coronary artery due to the myocardium is not studied extensively. In this chapter, we study the effects of compliance mismatch under the influence of dynamic changes in curvature and torsion. It is our objective to understand the influence of curvature and torsion changes on stented arteries. A model with deformable walls with uniform elastic modulus is used as the baseline control case. In order to study the effect of curvature and torsion variation on stent compliance mismatch, this baseline model is compared to models where the curvature, torsion and both curvature and torsion change, in addition to changes in compliance. The elastic modulus was increased by two, five and ten fold in the stented section for all three modes of motion. The simulations provided detailed information regarding the secondary flow dynamics under the influence of the compliance discontinuities. The compliance discontinuities affect the secondary flow patterns and augmented vorticity flux that in turn affect the wall shear stresses. As a result, this work reveals how changes in curvature and torsion act to modify the near wall hemodynamics of stented arteries.

Boundary Conditions

FSI

The arterial wall thickness was set to 10% of the radius and the Young's modulus was set to 0.6MPa for the normal unstented vessel that was used as the baseline case to study the effect of the compliance change on hemodynamics. Other relevant properties are listed in Table 6.1.

Table 6.1Wall properties used for the base line unstented case

Parameter	Value
Vessel Radius (m)	0.00150
Vessel Length (m)	0.1303
Fluid Kinematic Viscosity(m^2s^{-1})	4.9E-6
Fluid Density (kgm^{-3})	1060
Young's Modulus ,E (Pa)	0.6E+06
Wall thickness(m)	1.5E-04
Wall Density (kgm^{-3})	1060
Shear Modulus	0.2E+06
Timoshenko shear correction factor	1

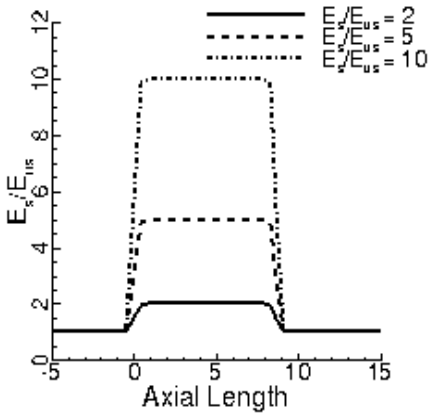

Figure 6.1 Change in compliance due to stent effects that are applied to the stented cases as compared to with the unstented baseline

Vernhet et al.[78] observed that after three months the compliance values at the stented section were smaller than surrounding unstented tissue by a factor of 5-6 times. Thus to study the effect of compliance mismatch, the Young's Modulus was changed in the middle section of the vessel to values 2, 5, and 10 times the baseline value. The ratio of the elastic modulus along the length of the vessel to the baseline value is shown in Fig. 6.1. In order to prevent sudden jumps in compliance, an exponential curve fit was used, as seen in Fig. 1 and as shown in Eq. (6.1), where constant 'a' takes values of 1,4 and 9 for Young's Modulus ratio of 2,5 and 10 respectively. All the other properties remain

unchanged as listed in Table 6.1. To make sure that the results obtained are repeatable, all calculations were run at least for three cycles.

$$\frac{E_s(x)}{E_{us}} = \begin{cases} 1 + \dfrac{a}{\left(1 + e^{-\left[\left\{(x - x_{begin} + x_{trans}/2)/x_{trans}\right\}4\pi - 2\pi\right]}\right)}, & x \le 4.344 \\ 1 + \dfrac{a}{\left(1 + e^{\left[\left\{(x - x_{end} + x_{trans}/2)/x_{trans}\right\}4\pi - 2\pi\right]}\right)}, & x > 4.344 \end{cases} \quad \textbf{6.1}$$

Dynamic Change in Curvature and Torsion

In order to study the effect of the curvature and torsion, a simplified coronary artery in the form of a helix resting on a cylindrical heart is used. The maximum height and radius of the heart was set to 0.09m and 0.03m respectively, with the radius of the helical tube being 0.0015m. The heart rate was set to 60 beats/min. The time varying contraction and expansion of this mock heart can be modeled as shown in Fig. 6.2a. The curvature and torsion of a helix is defined as shown in Eqs (6-7) below.

$$\kappa = \frac{\alpha}{\alpha^2 + \beta^2} \quad \textbf{6.2}$$

$$\tau = \frac{\beta}{\alpha^2 + \beta^2} \quad \textbf{6.3}$$

In Eqs (6.2 – 6.3) ‘α’ is the radius of the cylinder on which the helix rests and ‘β’ is the circumferential raise of the helix (if ‘h’ is the height of the cylinder, then $2\pi\beta = h$). In order to investigate the influence of the time dependent change in curvature and torsion of the coronary artery, three different modes of motion are studied. First, the volume of the cylindrical heart is changed as a function of time, holding the ratio of the cylinder radius and height constant, as shown in Fig. 6.2a. The corresponding change in curvature and torsion is shown in Fig. 6.2b. In this mode, both the curvature and torsion of the helix change with time. The other two modes of motion are to change curvature only, holding the torsion constant, and to change torsion only, holding the curvature constant. The change in volume of the cylinder and the corresponding change in shape of the helix are

shown in Fig. 6.3 at six time levels of one half of the cycle for all the three modes of motion. It should be noted that the length of the helix is constant for all modes of motion.

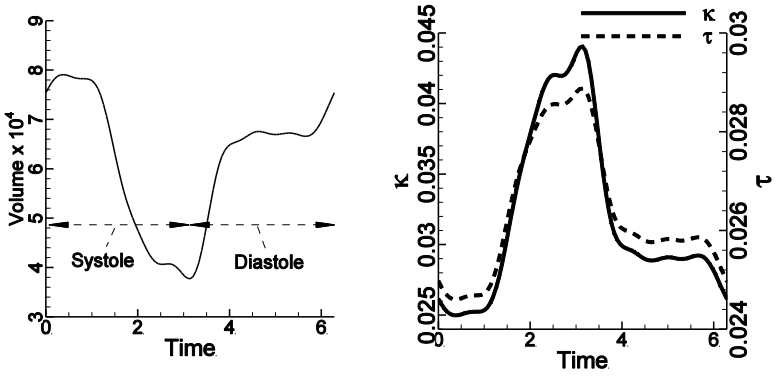

(a) (b)

Figure 6.2 (a) Change in Volume of cylindrical heart (b) Corresponding change in curvature and torsion during the motion of the helical tube resting on the cylindrical heart

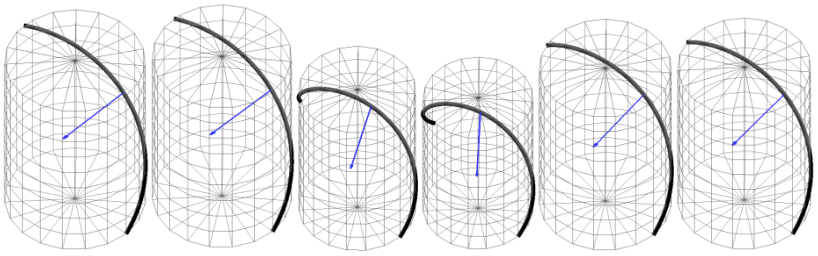

(a)T = 0 (b) T = π/3 (c) T = 2π/3 (d) T = π (e) T = 4π/3 (f) T = 5 π/3

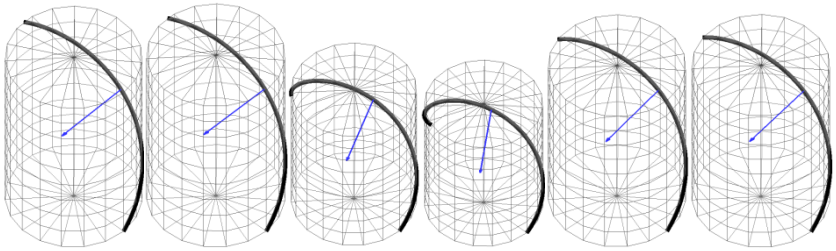

(g)T = 0 (h) T = π/3 (i) T = 2π/3 (j) T = π (k) T = 4π/3 (l) T = 5 π/3

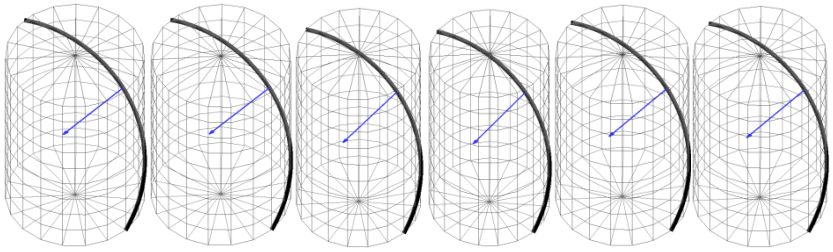

(m)T = 0 (n) T = π/3 (o) T = 2π/3 (p) T = π (q) T = 4π/3 (r) T = 5 π/3

Figure 6.3 Change in helix shape with time at five time levels. Curvature and torsion changes for (a) through (f), curvature changes for (g) through (l) and torsion changes for (m) through (r).

The location of the mid-plane and the normal vector from this plane to the centerline of the cylinder is also shown in Fig. 6.3. The specifics of the applied motion are presented in detail in [86].

Flow Boundary Conditions

The applied representative inlet velocity waveform and the outlet pressure waveform corresponding to observed pulse waveforms for healthy resting conditions are shown in Fig. 4[87]. The applied pulsatile flow combined with the change in volume (Fig. 2a) provides a realistic correlation with actual flow conditions experienced by an idealized left main coronary artery. It should be noted that all the values shown in figures and tables in this work are expressed in non-dimensional terms using the characteristic scales described in the flow solver section. The values used fall within observed physiological variations due to various biological factors. The peak Reynolds number is 191.6 and the near wall grid resolution is 8e-3. The temporal discretization used for the calculations was $5x10^{-4}$, selected to maintain the CFL number less than 0.1. The convergence criteria for the pressure and momentum equations are set to 10^{-6} at each time step. The details of the grid independency and validation studies are detailed in [55, 86]. In Fig. 4, the dots represent the pressure and the gradients represent the velocity at the times of interest in the study.

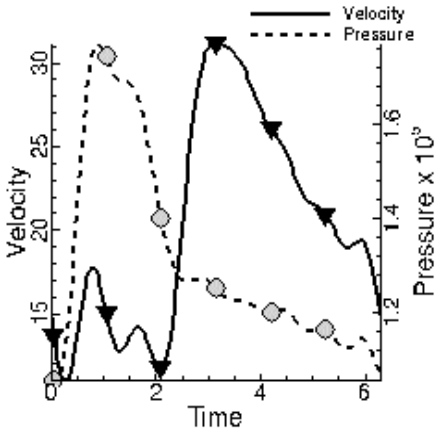

Figure 6.4 Applied coronary artery inlet velocity and outlet pressure waveforms. The velocity and pressure shown are normalized using $a^*\omega^*$ and $\rho\left(a^*\omega^*\right)^2$ as the characteristic scales, respectively. The gradients represent the velocity and the dots represent the pressure at the times of interest.

Results

In order to understand the effects of torsion and curvature on flow, it is useful to define the Dean Number, Germano number and non-dimensional parameter γ [83] as shown in Eqs. (6.4-6.5).

$$Dn = \mathrm{Re}_D \, \kappa^{0.5} \tag{6.4}$$

$$Gn = \mathrm{Re}_D \, \tau \tag{6.5}$$

$$\gamma = \frac{Gn}{Dn^{1.5}} \tag{6.6}$$

In the above equations, the Reynolds number is defined based on tube diameter and the applied mean flow velocity at the inlet. Here the Dean Number is a measure of the centrifugal forces and the Germano Number is a measure of twisting forces. The Germano number is a direct measure of the ratio of the twisting forces to the viscous forces or the effect of the torsion on the flow. A third non-dimensional number was defined by Liu et al.[83] for large Dean Numbers, as shown in Eq (6.6). The above parameter defines the relative importance of centrifugal forces to the twisting forces.

Parameters Studied

In the following paragraphs, results from 12 sets of simulations are presented. This includes the three modes of motion, each subject to elastic modulus variations of 1, 2, 5 and 10. The baseline for each mode is the corresponding unstented counterpart (E_s/E_{us} = 1). For each of these simulations, the following parameters are tracked: axial velocity, pressure, secondary stream function and wall shear stress (WSS).

The primary flow is represented by the axial velocity and is plotted as contour lines in a cross section. For helical tubes, the cross plane pressure difference caused by the centrifugal forces produce a flow perpendicular to the primary flow direction and is

termed as the secondary flow. The secondary flow is represented by contours of stream function obtained from the radial and circumferential velocities. This stream function is defined only in the r-θ (2D cross-sectional) coordinates at that instant in time. A positive value indicates a counter-clockwise rotating vortex and a negative value indicates a clockwise rotating vortex. Also a higher stream function value indicates higher secondary flow strength.

For figures showing flow characteristics in a cross-section, for example in Fig. 5, the inner wall is defined as the side of the helix that is in contact with the cylindrical heart at all instances and the wall diametrically opposite to the inner wall is termed as the outer wall. The other two principle edges are designated as right and left walls, in the counter clockwise direction with respect to the inner wall. The inner wall is located at the lower end of the vertical axis and the outer wall is the upper end, as shown in the inset. Most figures are plotted at T = 3.15 at the peak flow, unless otherwise stated. This is done for brevity and the shown flow field is representative of the flow fields seen at other time levels. Deductions made at T = 3.15 are applicable at other time levels also.

The organization of the following sections is as follows. First the results for the baseline pulsatile flow in a moving unstented helical tube, subject to changes of curvature and torsion are presented to establish flows in such configurations. This is followed by the comparison of the flow field for the three modes.

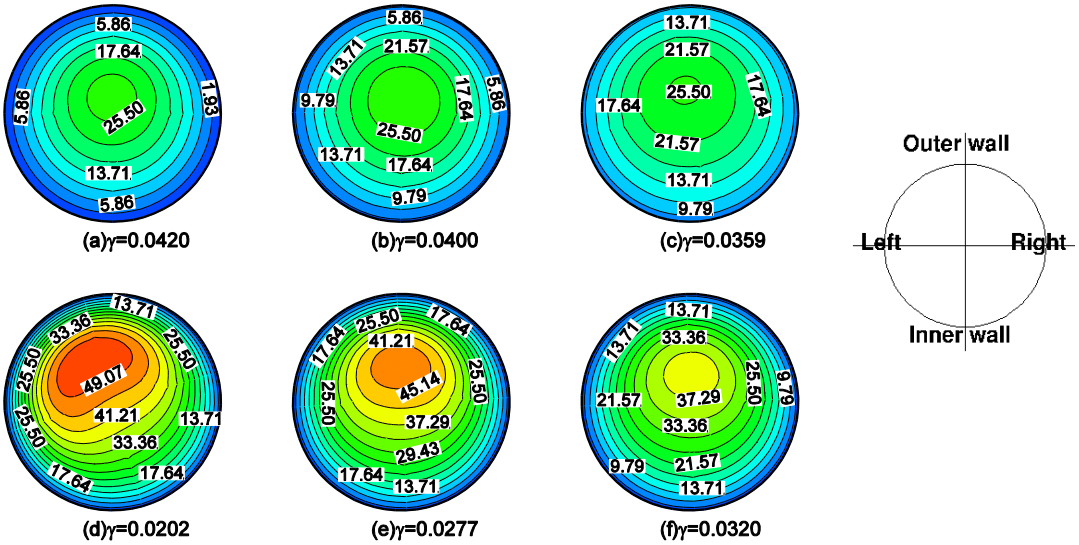

Figure 6.5 Axial velocity profiles at 44a* from the inlet of the helical tube at six time values: (a) T = 0.05 (b) T = 1.05 (c) T = 2.1 (d) T = 3.15 (e) T = 4.2 (f) T = 5.25. The helical tube is unstented. The values below the figures is the non-dimensional parameter γ

Pulsatile Flow in a Moving Unstented Helical Tube

In this section, the flow characteristics of pulsatile flow in the helical tube moving with both the curvature and torsion changing (Fig.6.2b) are discussed, with the aim to isolate the effect of the moving, compliant walls and the effect of the γ parameter. Fig. 6.5 shows the axial velocity profiles at the middle of the helical tube, at $44a^*$ from inlet of the helical tube at six time levels. At T = 0.05, when γ is the highest and the velocity profile is near symmetrical (Fig. 6.5a) due to the relatively reduced effects of centrifugal forces. As γ decreases, the velocity profile moves towards the outer wall due to the increased effects of centrifugal forces. A further decrease in γ moves the maximum velocity further towards the outer wall and creates a flatter velocity profile. This flattening of the parabolic profile increases as the effects of the centrifugal forces increases (Fig. 6.5d). This distribution of axial velocities will affect the wall shear stress magnitudes.

Fig.6.6 shows the contours of stream-function at six instances in time. When γ is large, the stream function contours are near symmetrical, with the dividing line of the two vortices being almost vertical. As seen in Fig.6.6a, the flow consists of a pair of counter-rotating vortices. This secondary flow pattern is known to form due to the centrifugally-induced pressure gradient, driving the slow moving fluid near the inner wall towards the center and the faster fluid from the center to the outside. When the Reynolds number is small, the secondary flow induced by the centrifugal forces due to the curvature is small. With the decrease in γ parameter, boundary layers develop leading to the formation of a dominant counter-clockwise vortex. Similar observations were made by Yamamoto et al. [84] in flow visualization experiments in stationary helical tubes. It is also seen that the secondary streamlines become denser near the wall and sparser near the center of the flow as Reynolds number increases or as γ decreases due to the development of the boundary layers.

Figs. 6.5-6.6 represent the isolated effects of the pulsatile flow conditions and moving boundaries. Also the importance of γ to characterize flows becomes apparent. More detailed analysis of the effect of the movement alone is presented in our previous work Observations similar to those seen in [88] were made for the baseline cases for changes in curvature and torsion alone, which are not shown here for brevity.

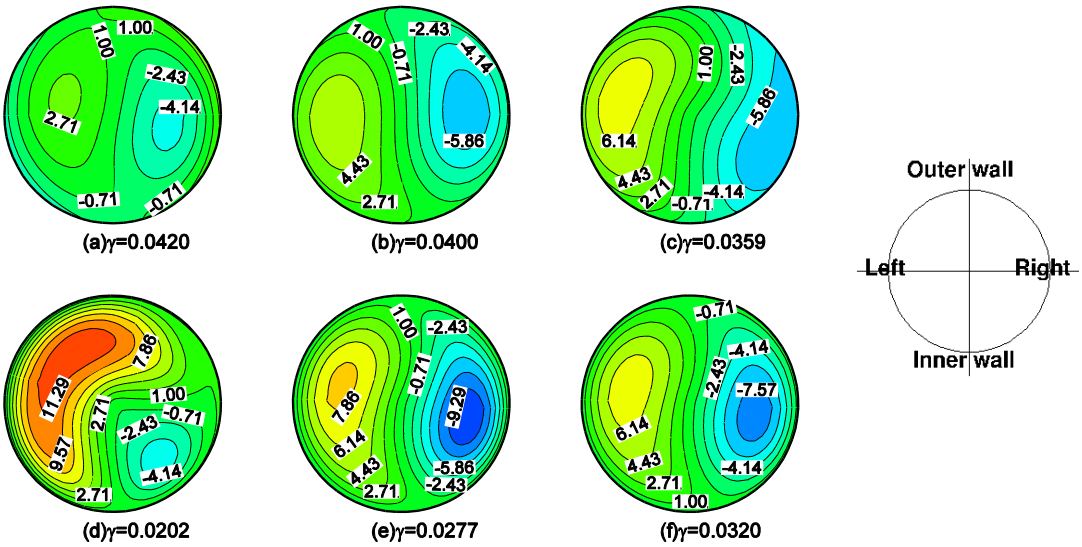

Figure 6.6 Secondary flow patterns at 44a from the inlet of the helical tube at six time values: (a) T = 0.05 (b) T = 1.05 (c) T = 2.1 (d) T = 3.15 (e) T = 4.2 (f) T = 5.25. The helical tube is unstented. The values below the figures is the non-dimensional parameter γ

Comparison of Stented and Unstented Helical Tube Flow Fields

The flow characterization in a stented artery depends on the wave form, pulsatility, elastic modulus variation and the arterial movement. Vortex formation has been shown to occur due to elastic modulus mismatch between stented and unstented sections of the artery, in straight non-moving stented vessels [41, 55].

To understand the effects of elastic modulus variation under the influence of dynamic geometry change, we first present the axial velocity profile for the three modes and for the three elastic modulus levels in Fig. 7 at T = 3.15 and at the mid stent location. The corresponding γ value at T = 3.15 is shown in the leftmost column for all the modes studied. As stated in the preceding section, when γ is higher, the centrifugal forces are less dominant compared to the twisting forces and leads to a more symmetrical flow

field. The γ parameter is the highest at all times when the torsion changes and is the lowest when the curvature changes. When torsion changes (row 1), a centered and near symmetrical axial velocity profile is seen. When curvature changes (row 2), the velocity profile is moved towards the outer wall and becomes flat.

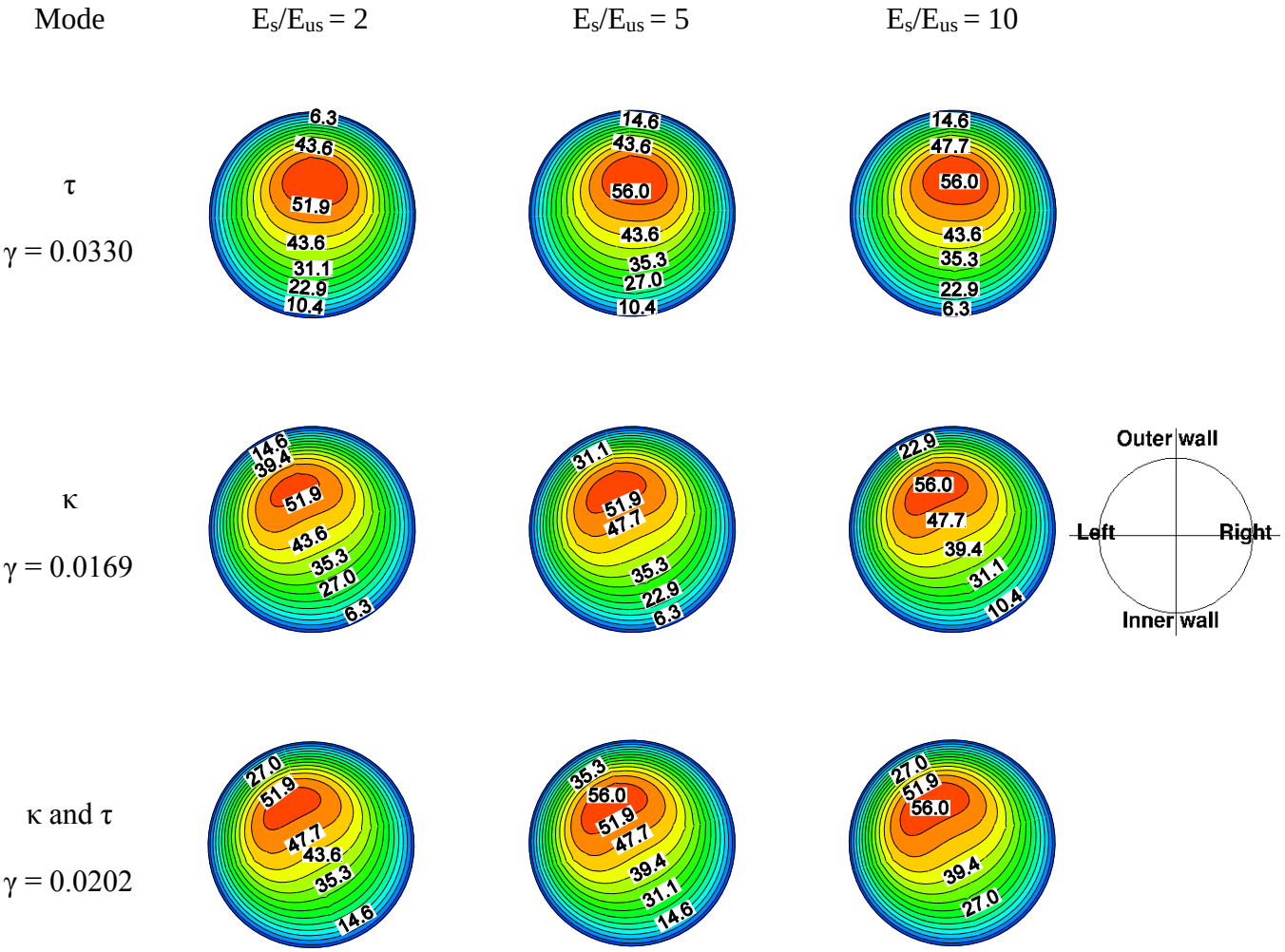

Figure 6.7 Axial velocity profiles in the stented artery at peak flow at T = 3.15 in the mid-stent region (44a*). Deductions made at T = 3.15 are applicable at other time levels.

For the modes of motion where the curvature changes, the velocity profile is rotated about the vertical axis due to the dynamic movement of the helical tube. When both curvature and torsion change (row 3), the flow field is similar to when curvature changes, pointing to the dominant role played by centrifugal forces compared to twisting torsional forces, for the configurations studied in this work. The axial velocities for the stented and unstented helical tubes are similar at the pre-proximal location of the stent. At

the proximal end of the stent, the arterial wall is less compliant. This change in elastic modulus causes the flow to accelerate compared to the unstented vessel and leads to a higher axial velocity values in the stented section, as seen from a comparison of Fig. 6.5d and Fig. 6.7, row 3. This increase in velocity due to the presence of the stent increases with increasing elastic modulus ratio (Fig. 6.7, row 3, column 1 vs. Fig. 6.7, row 3, column 3). For example, for the unstented helical tube subject to changes in curvature and torsion (Fig. 6.5d), the maximum axial velocity is 49.07 units. By comparison, the presence of the stent of elastic modulus ratio of 10 causes the maximum axial velocity to increase to 56.0 units (Fig. 6.7, row 3, column 3). This change in velocity due to the presence of the stents will change the near wall velocities, as seen in Fig. 6.8.

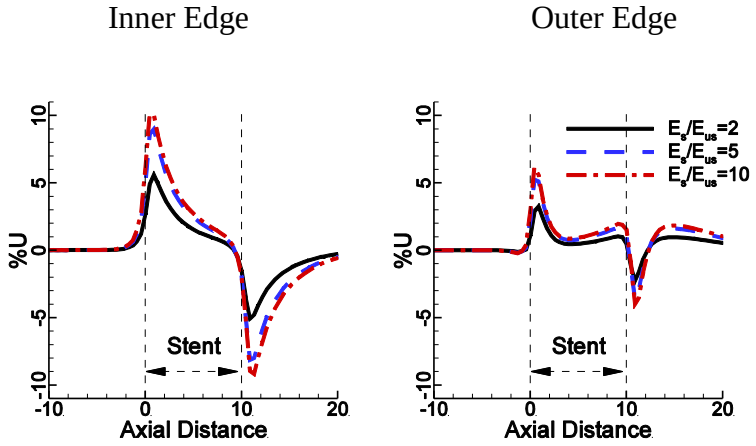

Figure 6.8 Percentage change in near wall time averaged axial velocity profile of stented vessels with respect to the unstented helical tube for changes in elastic modulus and changes in curvature and torsion.

The percentage variation of time averaged near wall axial velocity (%U) with respect to the unstented baseline is shown in Fig. 6.8, for the mode where curvature and torsion change, at the inner and outer edges. %U increases at the proximal location due to the reduced wall deformation in the stented region. %U decreases at the distal end, due to the relative increase in deformations after the stented region. Also the effect of the centrifugal forces become apparent, where the inner wall experiences a higher change in %U compared to the outer wall. With an increase in elastic modulus ratio, %U increases and asymptotes. When E_s/E_{us} = 2, %U changes by 5.6% at the proximal location, compared to 10.1% for E_s/E_{us} = 10. Similar changes were also seen for the other two

modes of motion. These changes in near wall velocities have a direct impact on the wall shear stress distribution.

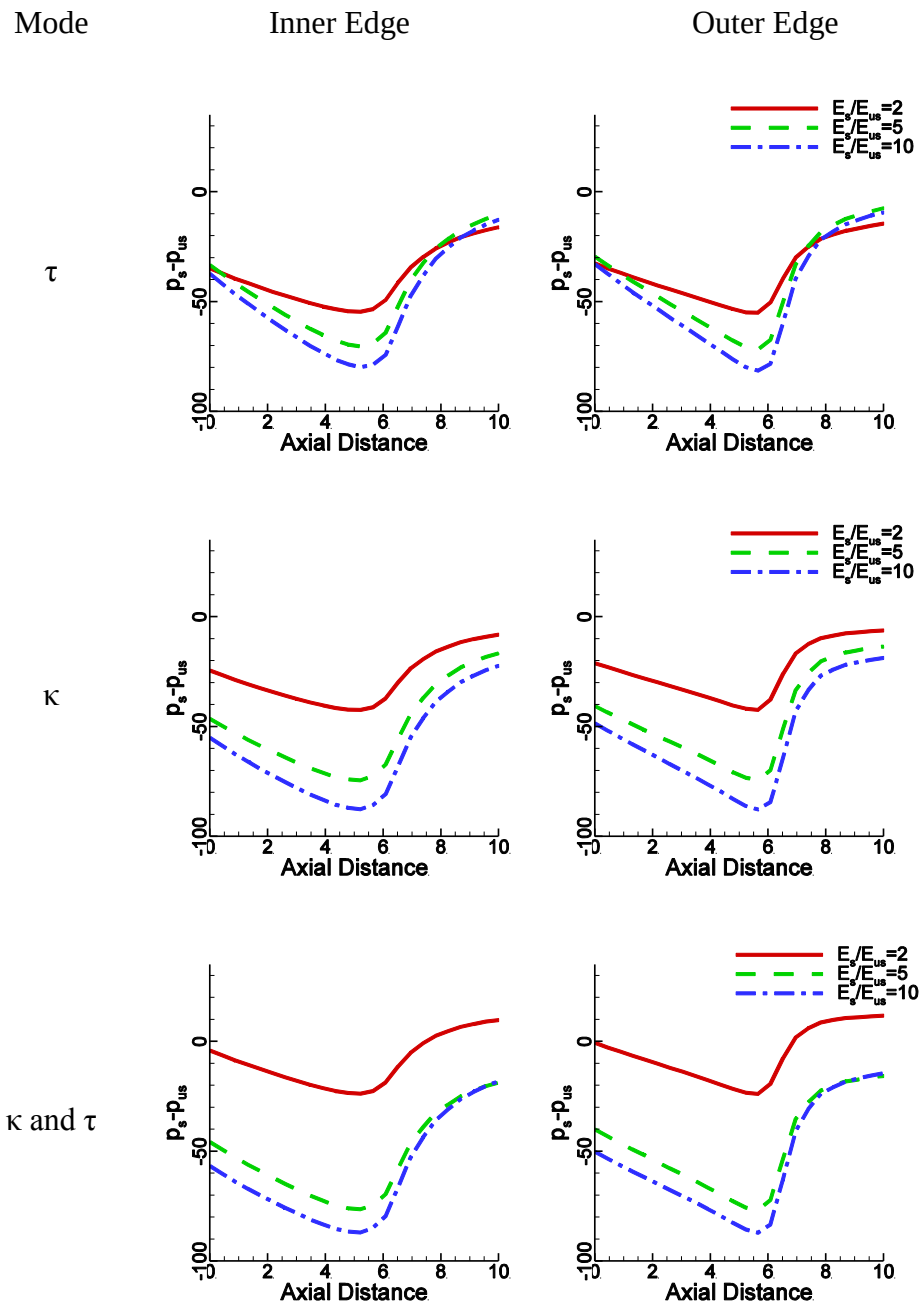

Figure 6.9 Variation of near wall differential pressure at T = 3.15 for all three modes of motion, at the inner and outer edges. The values shown are obtained by taking the difference of the pressure profiles of the stented and unstented arteries.

Fig. 6.9 shows the variation of near wall differential pressure with respect to the unstented baseline for each mode, at T = 3.15 for the three modes studied, on the inner

and outer edges over the length of the stent. At the proximal end of the stent, the elastic modulus discontinuity causes pressure to drop from the unstented value. The pressure tends to return back to the unstented values at the distal end. This is seen for all modes of motion. The differential pressure drop increases with increasing elastic modulus ratio, more so when curvature changes, either independently or with torsion. This drop in pressure is higher at the outer edge and compared to the inner edge. Fig. 6.9 shows the effect of the elastic modulus change and the applied motion on near wall pressure.

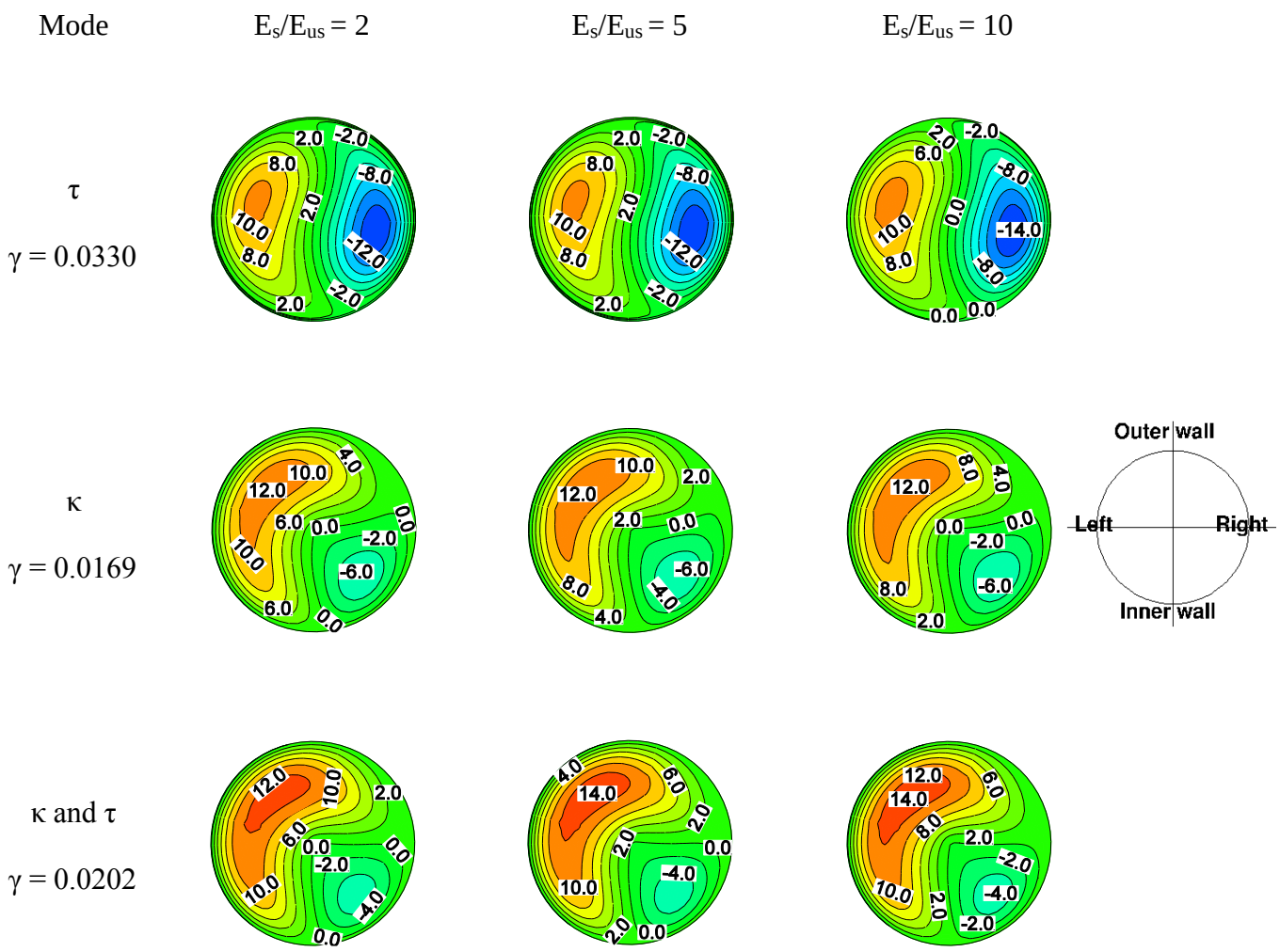

Figure 6.10 Contours of secondary stream function variation in the stented artery at peak flow at T = 3.15, in the mid-stent region (44a*). Deductions made at T = 3.15 are applicable at other time levels.

Fig. 6.10 shows the secondary flow field at the mid-stent location at peak flow (T = 3.15) for the three modes and for the three elastic modulus levels at the mid stent location. The corresponding γ value at T = 3.15 is shown in the leftmost column for all

the modes studied. The γ parameter is the smallest at all times when the curvature changes and is the highest when the torsion changes. Thus the secondary flow field is near symmetrical when torsion changes (Fig. 6.10, row 1) compared to when curvature changes (Fig. 6.10, row 2 and 3). A change in torsion alone also leads to a stronger clockwise rotating vortex on the right side whereas a dominant vortex forms on the left, outer side when curvature changes. As seen from the axial velocity profiles in Fig. 6.7, with an increase in elastic modulus ratio, the strength of the secondary flow field increases. The dominant, counter rotating vortex forms earlier when the elastic modulus ratio is higher with curvature changes (not shown). The observations from Figs. 6.7 and 6.10 for the stented artery can be summarized as follows:

- When γ is large, the flow is dominated by the twisting forces, leading to near symmetrical primary and secondary flow distributions.
- When γ is small, the flow is dominated by the centrifugal forces, the primary and secondary flow fields becomes skewed towards the left outer wall, leading to the formation of a dominant vortex.
- An increase in elastic modulus ratio increases the strength of the primary and secondary flow fields.
- The cross-sectional variation of shear stresses will be affected by the changes to γ parameter with motion and by changes in elastic modulus.

Discussion

The above results demonstrate that changes in elastic modulus in moving helical tubes due to presence of stents lead to changes in local flow patterns, in addition to the differences seen for the various modes of motion studied in this work.

Hemodynamic Parameters

To illustrate the relative importance of torsion and curvature change on the local wall shear stress (WSS), we present in Fig. 6.11 the percentage WSS change, for changes in curvature and torsion independently, with respect to the mode where both curvature and torsion change. The first column is at the proximal end, the second column is at the mid-stent location and the third column is at the distal end of the stent. The stented

helical tube has an elastic modulus ratio of 10.0. The plots show this variation along the circumference, with the inner edge located at 0° and the outer edge located at 180°. WSS is higher on the right side (0° to 180°, counterclockwise) when torsion changes, with respect to the mode where both curvature and torsion change. This is due to the effect of the secondary flow field (Fig. 6.10, row 1, column 3) seen, where a vortex of higher strength forms on the right side. This is in contrast to when both curvature and torsion change, where a dominant vortex forms on the left side. This leads to the relative decrease in WSS on the left side (180° to 360°, counterclockwise) when only torsion changes. When a similar comparison is made for the mode where curvature alone changes, the WSS change is relatively small, pointing to the dominant role played by curvature, compared to torsion, as seen in Figs. 6.7 and 6.10. Similar observations were made in our previous work [88]. From the above, WSS is higher on the left side when curvature changes and is higher on the right side when torsion changes.

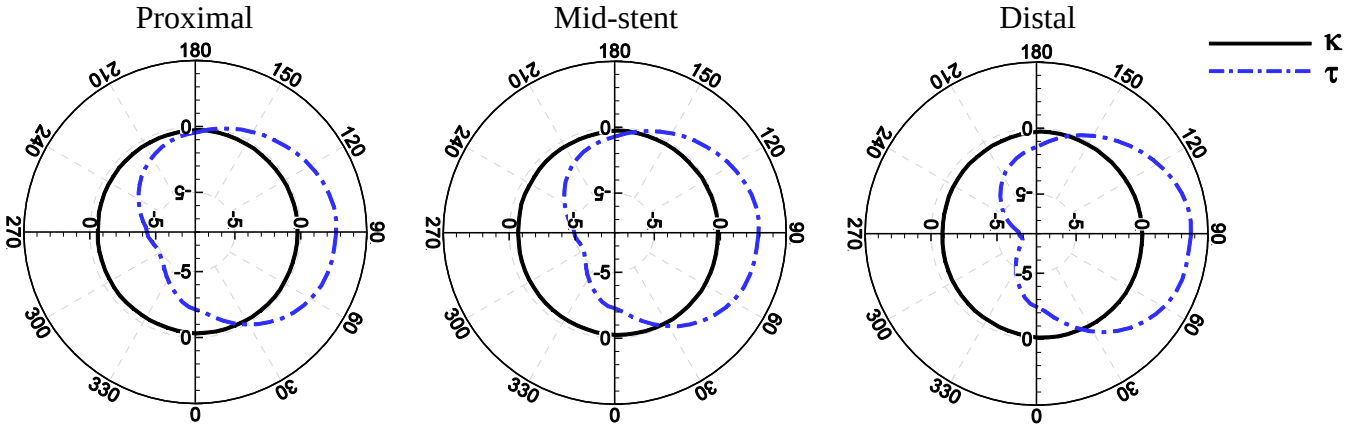

Figure 6.11 Percentage change in WSS for changes in curvature and torsion alone, with respect to the mode where both curvature and torsion change with time. The first column is at the proximal end, the second column is at the mid-stent location and the third column

Fig. 6.12 lists the percentage change of time averaged WSS with respect to the unstented baselines at the inner and outer edges of the helical tube for the mode where both curvature and torsion change. The proximal end of the stent is located at the axial location of 0.0. There is a clear increase in WSS at location where elastic modulus changes. This is mainly due to the decrease in deformation in the stented region accompanied by an increase in axial velocity. This is reversed at the distal end, as the vessel expands more after the stent, leading to a decrease in axial velocity. WSS changes

are the highest at the inner edge and lowest at the outer edge due to the skewing of the axial velocity towards the outer wall, by the centrifugal forces. The WSS change is as high as 15.4% at the inner proximal location for E_s/E_{us} = 10. From the extensive studies available in the literature [51-54], it can be concluded that local non-uniform hemodynamics triggers abnormal biological events. If we use the hypothesis by Lei et al. [81] that sites that experience large gradients in shear stress are prone to lesions, atherosclerosis and endothelial response, the conclusion to be drawn would be that the start and end of the elastic modulus discontinuity would lead to intimal thickening. This effect would be more pronounced at the inner wall than the outer wall and this corresponds to observed wall thickness values being higher at the inner wall of curved arteries [89].

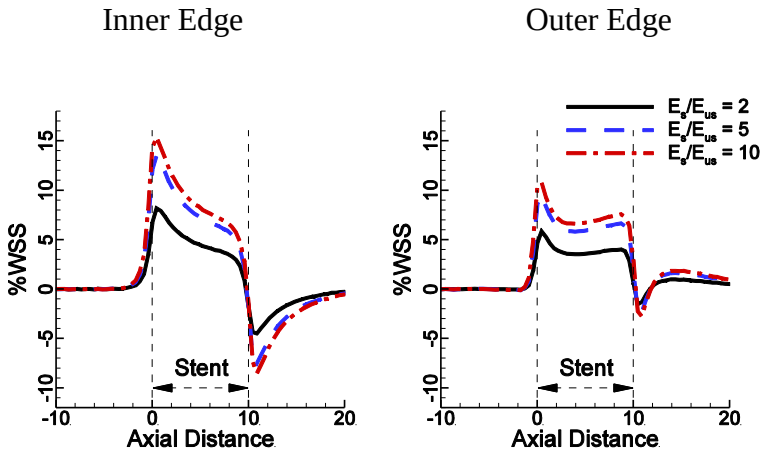

Figure 6.12 Percentage change in time averaged WSS in stented vessels with respect to the unstented vessel at inner and outer edges for changes in curvature and torsion.

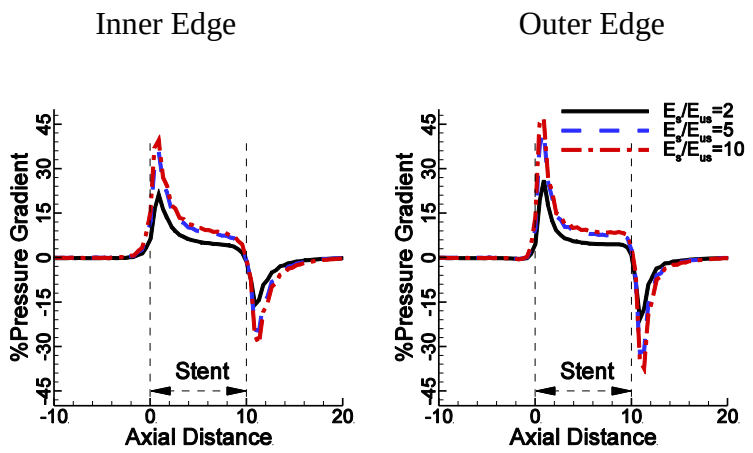

Figure 6.13 Percentage change in time averaged pressure gradient at the wall with respect to the unstented vessel at inner and outer edges for changes in both curvature and torsion.

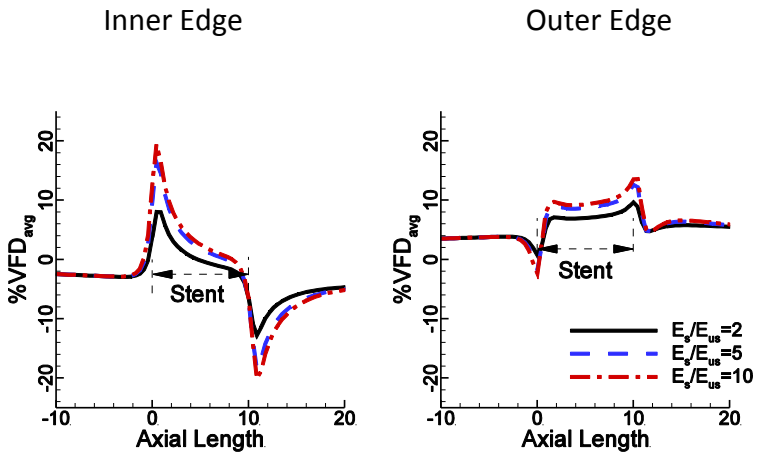

Physical Mechanism – Vorticity Production at the Wall

We defined and developed Vorticity Flux Density in our earlier works [55, 88] to understand the physical mechanism responsible for the observed changes in WSS under the influence of the elastic modulus variation with the movement of the helical tube. This is shown in Eq. (5.8). Vorticity Flux Density provides the relative importance of the pressure gradient and near wall velocity changes due to elastic modulus variation and applied motion. It also contributes to the shear stress at the wall by the following relationship

$$\omega_w \times n = \Omega^2 \tau_w \qquad \textbf{6.7}$$

where ω_w is the wall vorticity vector and n is the wall normal unit vector.

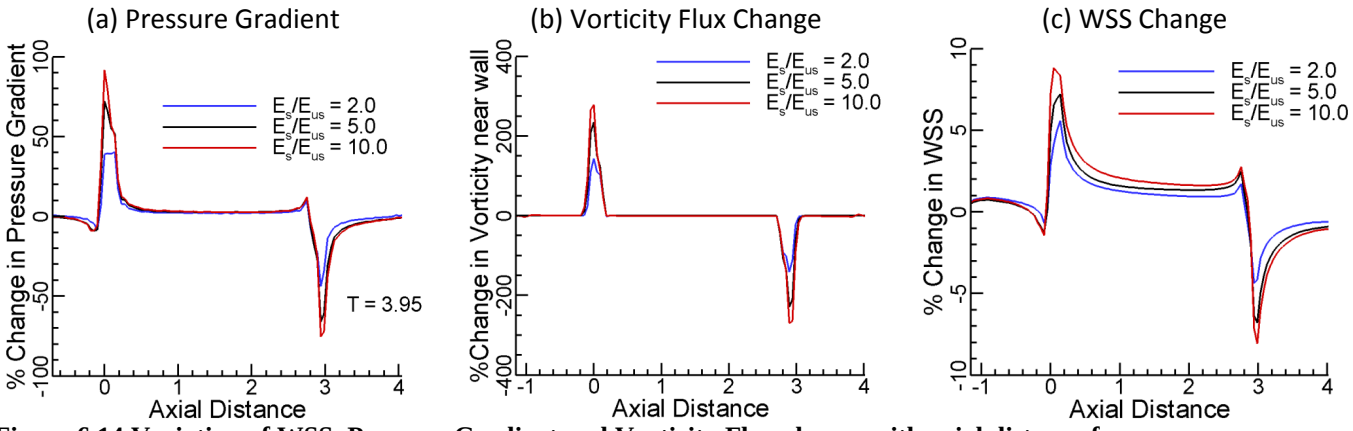

Figure 6.14 Variation of WSS, Pressure Gradient and Vorticity Flux change with axial distance for a straight, non-moving elastic tube subject to pulsatile boundary conditions as per Karri et al. [44] published in [38].

In a stationary stented vessel, since wall velocities are a consequence only of the vessel compliance, the main contribution to the vorticity flux density comes from the pressure gradient at the wall as described by Eq. (5.8). Fig. 6.15 shows the direct relationship between the pressure gradient, vorticity flux density, and the corresponding wall shear stress in a straight non-moving but compliant stented artery. However, curved arteries subjected to three-dimensional motion, exhibit secondary flows which have a large impact on the vorticity flux density as described in Eq. (5.8), which was established in our previous work on a moving unstented curved artery [88]. This effect is further accentuated by the presence of the stent which changes the local flow field by impacting the secondary flow magnitude in the vessel as shown in Figs 6.7 and 6.10. The effect of the stent on vorticity flux density as compared to the baseline unstented curved artery subjected to both curvature and torsional changes shown in Fig. 6.14. What is interesting to note is that the presence of the stent has opposite effects on the inner and outer edge of the vessel. At the proximal end of the stent, VFD increases at the inner edge while decreasing at the outer edge. The trend is opposite at the distal end of the stent. It is further instructive to note that these trends do not directly correlate with changes in the pressure gradient as shown in Fig. 6.13 which plots the differential pressure gradient with respect to the unstented vessel. The pressure gradient shows the same trends at the inner and outer sides of the vessel, which is contrary to the trends seen in the VFD. That leads us to the conclusion that changes in the secondary flow magnitudes due to the presence of

the stent have a non-negligible effect on VFD. As a consequence, WSS variations are no longer symmetric over the periphery of the vessel but show clear differences between the inner and outer walls as seen in Fig. 6.12.

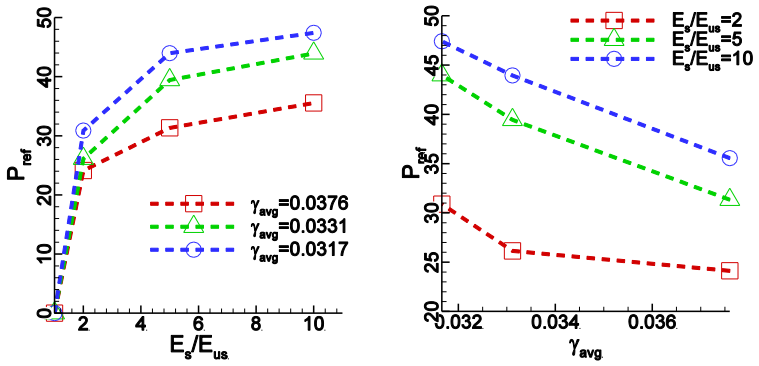

Figure 6.15 Variation of reflected pressure with respect to the unstented baselines. (a) Pref vs. Es/Eus (b) Pref vs. γavg

Pressure Reflection

In addition to WSS, the pressure wave reflection is another measure of adverse changes to local hemodynamics. Flows in compliant vessels propagate in the form of waves and are characterized by pressure wave reflections due to obstacles - in the form of elastic modulus variations due to the presence of stents for the current study. The contribution of pressure wave reflections to coronary artery disease is well known [33, 58, 90]. Peripheral artery stiffening can lead to increased wave reflections and therefore increased pulse pressures and augmented systolic pressures at the aortic root. Weber et al.[58] showed that pressure augmentation due to reflection divided by pulse pressure could be used as a significant predictor of early coronary artery disease. In order to ascertain the effect of the stent, the pressure reflected (P_{ref}) upstream was calculated for the time averaged flow field for all three modes and elastic modulus ratios. The variation of P_{ref} with respect to the elastic modulus ratios was a hyperbolic tangent (Fig. 6.16a), with the P_{ref} asymptotically reaching a maximum as the elastic modulus increases. This is similar to observations made in our earlier work[55]. The variation of P_{ref} with respect to the average γ parameter was an exponential function (Fig. 6.16b). Following [55], we obtain a surface fit for reflection coefficient as shown in Eq. (6.8).

$$P_{ref} = 7.246 \tanh\left(\log\left(1.111\left(\frac{E_s}{E_{us}} - 1 \right) + 1 \right) \right) e^{0.05951/\gamma_{avg}} \quad \textbf{6.8}$$

Eq. (6.8) provides a measure of P_{ref} for a given variation in elastic modulus and average γ parameter, providing a quick prediction of this parameter in helical configurations.

Intimal Thickness

Friedman et al. [86] presented an empirical relationship between the observed shear rates in arterial casts and measured intimal thickness at 163 sites for arterial sections of various ages. They observed that the vessels subject to lower shear rates became thicker in older vessels at a slower rate. The opposite effect was seen in younger vessels, where the vessels become thicker when the shear rates increase. Based on data analysis, the intimal thickness was expressed as shown in Eq. (6.9)

$$\delta(s,T) = h\left(1 + \alpha(s-1)\right) e^{\frac{\beta(1-s)}{s}} \left(1 - e^{\left(-Te^{\left(\frac{\beta(s-1)}{s} \right)} \right)} \right) \quad \textbf{6.9}$$

Here, δ is the intimal thickness, s is the normalized shear rate, T is the biological age parameter of the vessel, h is the thickness of the intimal layer exposed to shear s. The α parameter is the measure of the sensitivity of the uptake process to shear rate and β is the activation energy for the process that retards intimal thickening. Using Eq. (6.9), we calculated the intimal thickness ($\delta_{current}$) using the shear rates obtained from the current simulation results for the unstented helical tube subject to changes in both curvature and torsion. Following [86], α is set to 0.982 and β is set to 1.847. The biological age T is set to 6 units. The normalized intimal thickness thus obtained is shown in Fig. 6.17a by the solid line, for changes in both curvature and torsion. In this figure, the inner wall is indicated by 180° and the outer wall is indicated by 0°. As indicated by the WSS and secondary flow fields presented in the preceding sections, $\delta_{current}$ is more pronounced at the inner wall than at the outer wall. Ojha et al. [89] measured the intimal thickness (δ_{Ojha}) in the right coronary artery for 17 arteries from patients with an average age of 58.

Comparing $\delta_{current}$ and δ_{Ojha} [89] in Fig. 6.17a, an excellent agreement in trend is seen and $\delta_{current}$ lies within the measured variation at all locations.

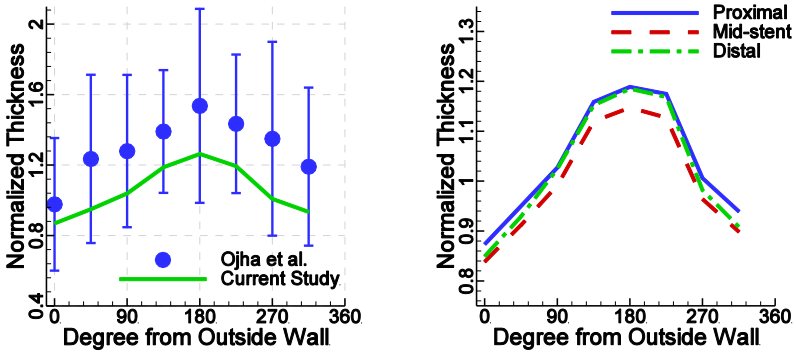

(a) (b)

Figure 6.16 Normalized Intimal thickness calculated based on Eq. (12). (a) Unstented (b) Stented. The values are normalized with the average intimal thickness. The helical tube is subject to changes in both curvature and torsion.

Fig. 6.17b shows the calculated intimal thickness for the stented vessel (E_s/E_{us} = 10) at the proximal, mid-stent and distal locations, for changes in both curvature and torsion. The shear rates obtained from the current computations for the stented helical tube are used in Eq. (6.9) and the other parameters are set the same values as used for the calculation of $\delta_{current}$ .The helical tube is subject to changes in both curvature and torsion. In Fig. 6.17b, the calculated intimal thickness is higher at the inner wall for all three locations. As predicted in our previous work [55], the intimal thickness is higher at the proximal and distal ends and this corresponds well with experimental observations of Vernhet et al.[78], who studied the effects of long term stenting in animal models.

Limitations of the Current Work

The present study is subject to several assumptions, generalizations and limitations that are discussed below. First the arterial geometry was assumed to be a simple helical tube and this artery was assumed to rest on a cylindrical heart. Here the main aim was to obtain generalized results that try to isolate the effects of the changes in curvature and torsion as seen in coronary arteries. Our comparisons of the computed intimal thickness from the current study with the measurements by Ojha et al. [89] show that the intimal thickness variations are well within the measurement variations for coronary arteries,

showing the applicability for the generalizations carried out. The effect of the stent deployment strategy and the post stent injury caused to the artery that would contribute to restenosis is not considered. However, the objective of the current study was to isolate the effects of the change in elastic modulus due to the presence of an idealized stent on the flow and on the hemodynamic parameters that have been implicated in stenosis. This study does not consider the effect of changes in mechanical stresses in the vessel wall that might be important and affect remodeling. However, this effect is compounded by the combined hemodynamic changes, and literature suggesting that changes in hemodynamics would affect stenosis is extensive. Yet, if and how elastic modulus mismatch affects the local hemodynamics is unresolved. The present study aims to help understand this effect. The wall model used to calculate the radial deformations due to the fluid flow is a cylindrical membrane model. Only the radial deformation term is considered, due to the fact that the radial forces (pressure) dominate the other fluid stress components and thus would contribute to a larger extent to the flow disturbances due to the presence of the stent. This model has been used extensively in the literature [56, 57]. This model predicts the wall shear stress accurately and can thus be used as a good predictor of local hemodynamic function. An exponential transition of the elastic modulus is used, as indicated in Fig. 3. Care was taken to make sure that the elastic modulus transition was continuous and smooth. It is acknowledged that the transition used in the current study might be less gradual than in reality and this might cause some over prediction of the parameters presented in this paper. A future extension of this work would be to include a transition length based on experimental measurements.

Conclusion

Systematic three-dimensional CFD calculations have been performed for pulsatile flow with moving wall boundaries in simplified coronary arteries, using physiologically relevant flow waveforms, with the objective of studying the effect of elastic modulus variations and change of curvature and torsion on the local hemodynamics. The first mode was to change the curvature, the second mode was to change the torsion and the third mode of motion was to change both curvature and torsion. This change in curvature and torsion was effected to mimic the movement of an idealized heart on which the

simplified artery rests. The elastic modulus was changed from the baseline to a value that is 2, 5 and 10 times higher in the middle of the vessel to emulate the placement of a stent. The results suggest that changes in elastic modulus with accompanying changes to curvature and torsion cause critical changes in local hemodynamics, namely altering the local pressure and velocity gradients and secondary flow patterns. The change in pressure gradient at the elastic modulus discontinuity is as high as 47% when the elastic modulus is increased to 10 with respect to the unstented vessel, under the influence of both curvature and torsion changes. The corresponding WSS change is 15.4%. We show that these changes are attributed to the physical mechanism associating the secondary flow patterns to the production of vorticity (vorticity flux) due to the wall movement. A surface fit was also defined relating the pressure wave reflection coefficient with stent stiffness and average γ parameter. We also demonstrate that the movement of the artery due to the movement of the myocardium cannot be ignored and needs to be considered to accurately predict the effects of elastic modulus discontinuities such as would be caused by stents in coronary arteries.

7. Effects of Stent Length, Transition Length and Overexpansion in Stented Arteries

Introduction

The effect of stent length, stent transition length and stent overexpansion, under the influence of the motion of the coronary artery due to the myocardium has not been studied extensively. In this work, we study the effect of these stent parameters under the influence of dynamic changes in curvature and torsion. It is our objective to understand the influence of these three parameters on local hemodynamics. A model with moving deformable walls with an elastic modulus change of five in the stented section is used as the baseline control case. The simulations provided detailed information regarding the secondary flow dynamics under the influence of these parameters. It was found that increasing stent length, decreasing transition length and increasing the overexpansion would affect the local hemodynamics adversely and lead to higher variations in wall shear stress and pressure wave reflections. From the local hemodynamics and wall shear stress changes, it can be concluded that the smaller stent length that adequately covers the lesion site, higher transition length and lower overexpansion of the stented section would lead to improved flow conditions in the stented section.

Boundary Conditions

It should be noted that the applied conditions for the pulsatile boundary conditions, FSI and wall movement due to the motion of the myocardium used in this chapter is the same as used to study the effects of the compliance variation in Chapter 6. As stated in the introduction, the object of current work is to find the effects of the following stent parameters: stent length, transition length and overexpansion. To this end, the above parameters are changed as shown in Table 7.1.

Table 7.1 Test Parameters used in the current study

Parameter	Stented Baseline	Transition Length Study				Stent Length Study				Overexpansion Study			
Designations	Base	T1	T2	T3	T4	S1	S2	S3	S4	A1	A2	A3	A4
Stiffness Ratio	5	5	5	5	5	5	5	5	5	5	5	5	5
Coverage Length	7	7.0	7.0	7.0	7.0	15.4	23.8	32.2	40.6	7.0	7.0	7.0	7.0
Effective Stent Length	**8.4**	9.8	11.2	12.6	14.0	**16.8**	**25.2**	**33.6**	**42.0**	8.4	8.4	8.4	8.4
Transition Length	**1.4**	**2.8**	**4.2**	**5.6**	**7.0**	1.4	1.4	1.4	1.4	1.4	1.4	1.4	1.4
Total Stent Length	9.8	12.6	15.4	18.2	21.0	18.2	26.6	35.0	43.4	9.8	9.8	9.8	9.8
Radius Change%	**0**	0	0	0	0	0	0	0	0	**5**	**10**	**15**	**20**

The proximal and distal ends of the stent are defined as the axial location where the elastic modulus ratio is half of the change from the unstented to the stented value (3 in this study). The coverage length is set to 7 units for the stented baseline, the transition length is set to 1.4 units on either end and the total stent length is 9.8. The effective stent length was defined to be the distance between the midpoints of the proximal and distal transition regions, as seen in Fig. 7.1. For the baseline, the effective length is 8.4 units. To study the effects of transition length, the baseline transition length is increased by 2, 3, 4 and 5 times the baseline value of 1.4 units, taking care to maintain the same coverage length of 7 units. To study the effect of the stent length, the baseline effective stent length is increased by 2, 3, 4 and 5 times the baseline value of 9.8 units. With an increase in total stent length, the coverage length also increases. The modeled overexpansion characterizes the global effects of stent overexpansion in addition to the changes in compliance.

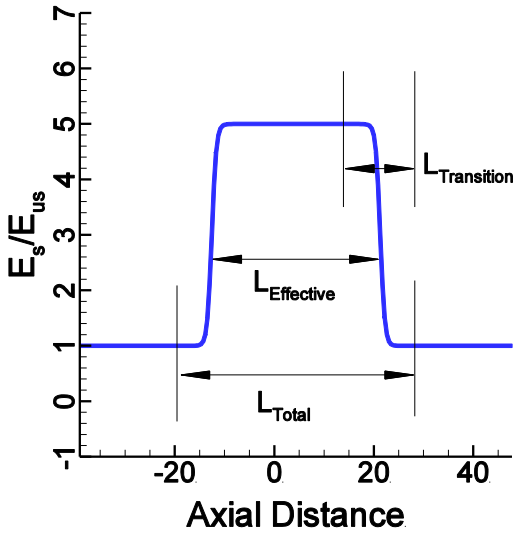

Figure 7.1 The definition of transition length and stent length as used in the current study

Results

Parameters Studied

In the following paragraphs, results from 12 sets of simulations are presented. This includes simulations with varying the transition length, stent length and overexpansion. For each of these simulations, the following parameters are tracked: axial velocity, secondary stream function and wall shear stress (WSS).

The primary flow is represented by the axial velocity and is plotted as contour lines in a cross section. For helical tubes, the cross plane pressure difference caused by the centrifugal forces produce a flow perpendicular to the primary flow direction and is termed as the secondary flow. The secondary flow is represented by contours of stream function obtained from the radial and circumferential velocities. This stream function is defined only in the r-θ (2D cross-sectional) coordinates at that instant in time. A positive value indicates a counter-clockwise rotating vortex and a negative value indicates a clockwise rotating vortex. Densely packed lines indicate higher fluid transport in the axial direction. Also a higher stream function value indicates higher secondary flow strength.

For figures showing flow characteristics in a cross-section, for example in Fig. 7.2, the inner wall is defined as the side of the helix that is in contact with the cylindrical

heart at all instances and the wall diametrically opposite to the inner wall is termed as the outer wall. The other two principle edges are designated as right and left walls, in the counter clockwise direction with respect to the inner wall. The inner wall is located at the lower end of the vertical axis and the outer wall is the upper end (Fig. 7.2). Most figures are plotted at T = 3.15 at the peak flow, unless otherwise stated. This is done for brevity and the flow field is representative of the flow fields seen at other time levels. Deductions made at T = 3.15 are applicable at other time levels also.

For the cases studied here, several groups were constructed by selecting a single parameter from Table 7.1 to change while the rest were held constant, allowing the relative effect of each change to be evaluated. The organization of the following sections is as follows. First the flow characteristics in the baseline stented elastic helical tube subject to changes in curvature and torsion is presented to establish the general characteristics seen in such flows. This is followed by the presentation of the flow field of each of the three parameters studied in this work.

Flow Field in the Baseline Stented Helical Tube

In this section, the flow characteristics of pulsatile flow in the baseline stented elastic helical tube moving with both the curvature and torsion changing is discussed, with the aim of providing a general description of the flow field seen in moving helical tubes and to isolate the effects of the γ parameter. Fig. 7.2 shows the axial velocity profiles at the mid-stent location, $44a^{*}$ from inlet of the helical tube at six time levels. At T = 0.05, when γ is the highest, due to the relatively less prominent effect of centrifugal forces, the velocity profile is near symmetrical (Fig. 7.2a). As γ decreases with an increase in curvature and centrifugal forces, the velocity profile tends to migrate towards the outer wall. A further decrease in γ leads to the maximum velocity moving further towards the outer wall and creating a flatter velocity profile as the effects of the centrifugal forces increases (Fig. 7.2d).

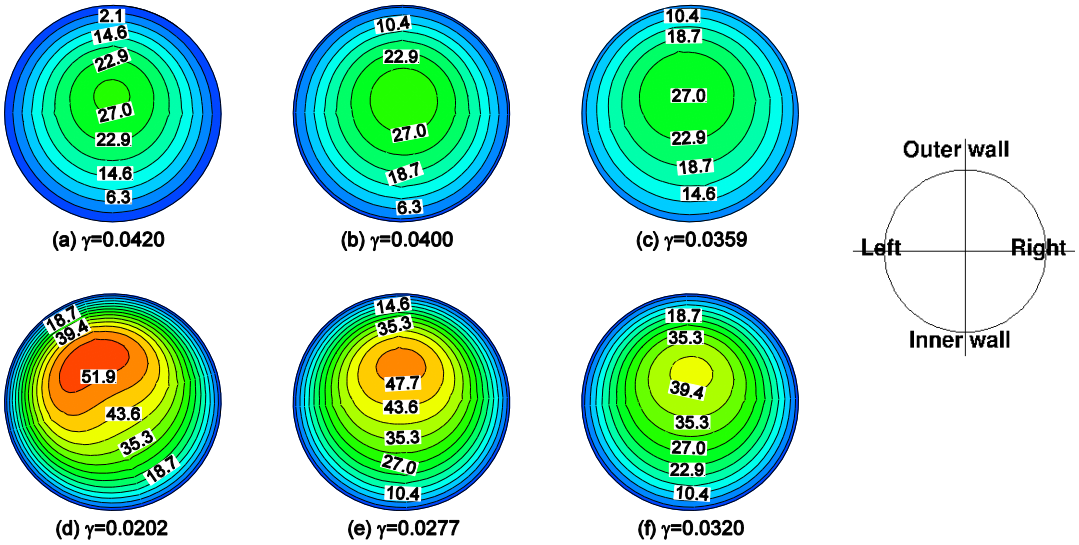

Figure 7.2 Axial velocity profiles at the middle of the tube (44a*) from the inlet of the stented helical tube at six time values: (a) T = 0.05 (b) T = 1.05 (c) T = 2.1 (d) T = 3.15 (e) T = 4.2 (f) T = 5.25. The value below the figures is the non-dimensional parameter γ.

Fig.7.3 shows the contours of stream-function at the same instances in time. When γ is large, the secondary stream lines are near symmetrical, with the dividing line between the two vortices being almost vertical. As seen in Fig.7.3a, the flow consists of a pair of counter-rotating vortices, placed symmetrically with respect to the plane of symmetry. This secondary flow pattern is known to form due to the centrifugally-induced pressure gradient, driving the slow moving fluid near the inner wall and the faster fluid from the center to the outside wall. When the Reynolds number is small, the secondary flow induced by the centrifugal forces due to the curvature is small. With the decrease in γ parameter, the boundary layers develop leading to the formation of a dominant vortex as seen in Fig. 7.3d. Similar observations were made by Yamamoto et al. [84] for a stationary helically coiled tube. It is also seen that the secondary streamlines become denser near the wall and sparser near the center of the flow as Reynolds number increases or as γ decreases. The general flow characteristics seen in moving helical tubes can thus be ascertained from Figs. 7.2 and 7.3.

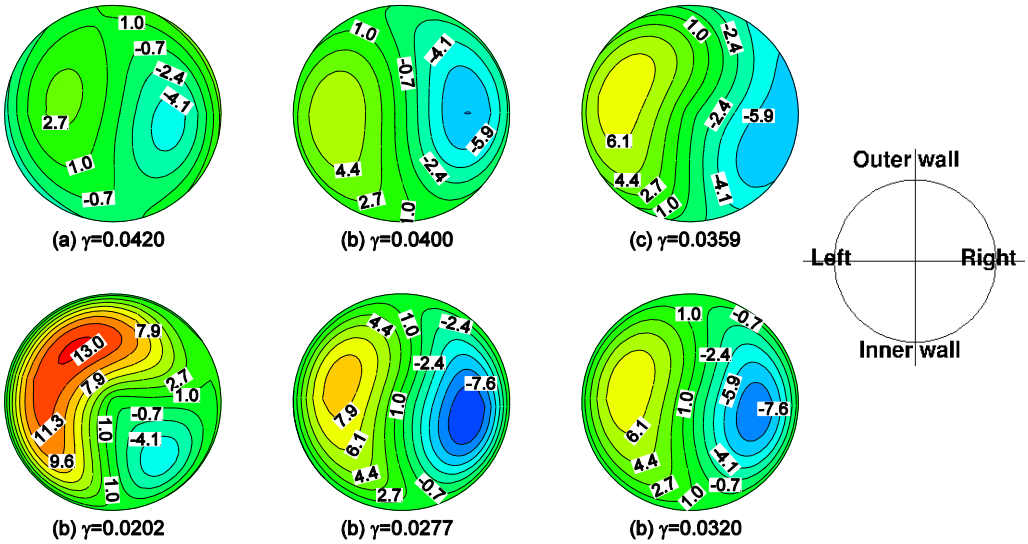

Figure 7.3 Contours of secondary stream function at the middle of the tube (44a*) from the inlet of the stented helical tube at six time values: (a) T = 0.05 (b) T = 1.05 (c) T = 2.1 (d) T = 3.15 (e) T = 4.2 (f) T = 5.25. The value below the figures is the non-dimensional parameter γ.

Transition Length Effects

To study the effect of the transition length, four lengths in addition to the baseline are examined: 2.8 (T1), 4.2 (T2), 5.6 (T3) and 7.0 (T4). Increasing the transition length smoothens the compliance variation from the unstented to the stented sections. This reduces the near wall velocities and secondary flow field strength as will be shown in Figs. 7.4 and 7.5 below.

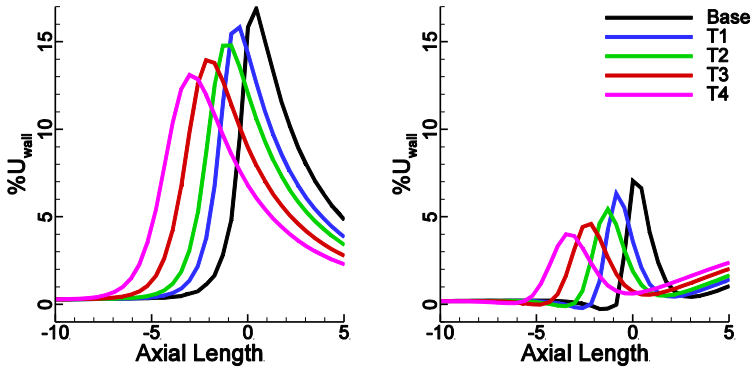

(a) Inner **(b) Outer**

Figure 7.4 Percentage change in near wall axial velocity profile with respect to the unstented helical tube at T = 3.15 for changes in transition length, at the proximal location for the (a) Inner and (b) Outer edges. The transition lengths are: base – 1.4, T1 – 2.8, T2 – 4.2, T3 – 5.6, T4 – 7.0.

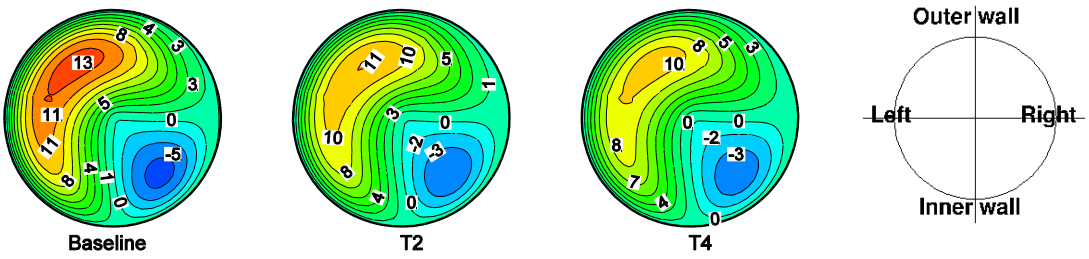

(a) Baseline = 1.4 **(b) T2 = 4.2** **(c) T4 = 7.0**

Figure 7.5 Contours of secondary stream in the stented artery at T = 3.15, at the mid-stent location. The transition lengths are given below each figure. $\gamma = 0.0202$ for all three figures.

The flow changes near the wall due to the variations in transition length are established via Fig.7.4. The near wall velocities drop with increasing transition length, affecting the shear stress distributions. In general, when there is no overexpansion, the near wall velocities increase due to the reduced wall deformation at the proximal location. Also the near wall velocity change is higher at the inner edge than the outer edge caused by the motion induced centrifugal forces. The transition length increase reduces the strength of the secondary flow field as seen in Fig. 7.5. This is due to the smoother wall deformation change between the pre-proximal locations and the proximal end of the stent.

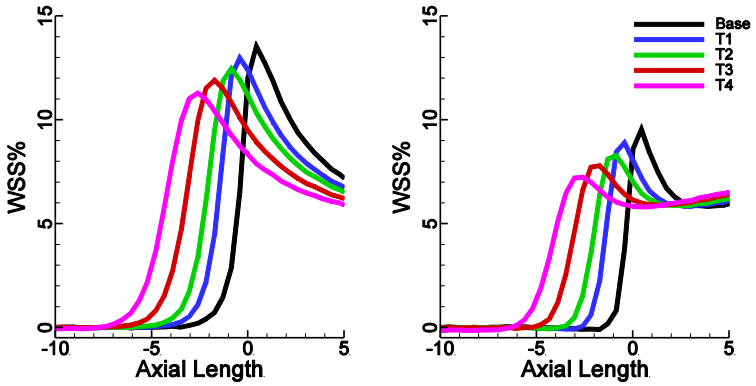

(a) Inner **(b) Outer**

Figure 7.6 Percentage change in time averaged WSS with respect to the unstented vessel at (a) Inner edge (b) Outer edge. The values shown are at the proximal end of the stent. The transition lengths are: base – 1.4, T1 – 2.8, T2 – 4.2, T3 – 5.6, T4 – 7.0.

Increase in transition length also reduces the wall shear stress (WSS) as shown in Fig. 7.6. At the same time the region subject to a higher WSS variation increases, as the

extent of the stent increases with an increase in transition length. Thus to summarize, the increase in transition length:

- reduces the near wall variation of axial velocity and the strength of the secondary flow field with respect to an unstented vessel
- reduces WSS changes with respect to the unstented vessel at the proximal and distal ends
- increase the total area exposed to abnormal WSS which will affect pressure reflection characteristics (discussed later)

Stent Length Effects

To study the effect of the stent length, four total stent lengths in addition to the baseline are examined: 19.6 (S1), 29.4 (S2), 39.2 (S3) and 49.0 (S4). The near wall velocities for the various stent lengths studied are examined in Fig. 7.7 for the inner and outer edges at T = 3.15 (peak flow). With increasing stent length, the near wall velocity with respect to the unstented artery decreases at the proximal end. This is due to the increased deformation induced by the higher upstream pressure. At the distal end, the near wall velocity increases with increasing stent length. This is due to the reduced deformation induced by the lower downstream pressure. A similar trend is seen at the outer edge, but as seen in Fig. 7.4, the near wall velocity change is lower due to centrifugal forces.

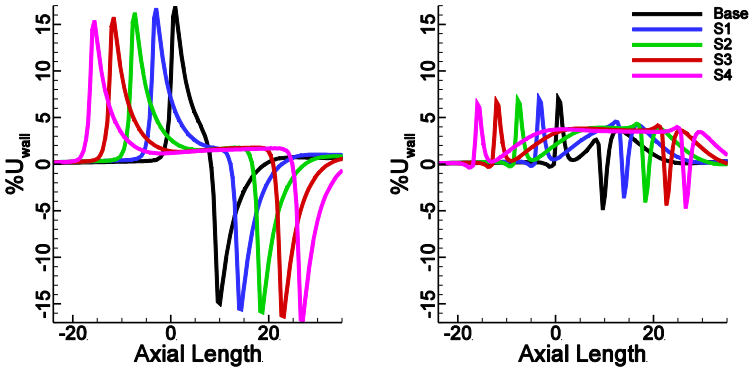

(a) Inner **(b) Outer**

Figure 7.7 Percentage change in near wall axial velocity profile with respect to the unstented helical tube at T = 3.15 for changes in stent length for the (a) Inner and (b) Outer edges. The total stent lengths are: base – 9.8, S1 – 19.6, S2 – 29.4, S3 – 39.2, S4

When the stent length is short, the relative closeness of the compliance transition zones increases the mid-stent $\%U_{wall}$ at the inner edge. This is reversed at the outer edge. A nominal drop in the strength of the counter clockwise vortex and a nominal increase in the strength of the clockwise rotating vortex are seen in Fig. 7.8, with increasing stent length. For both the vortices, this change is less than 4% for S4 with respect to the baseline stent length.

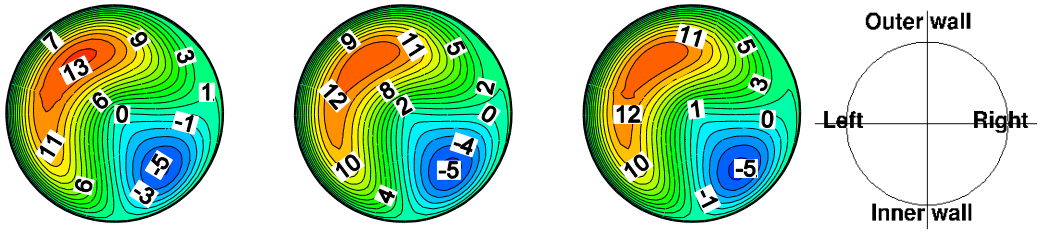

(a) Baseline = 9.8 **(b) S2 = 29.4** **(c) S4 = 49.0**

Figure 7.8 Contours of secondary stream in the stented artery at T = 3.15 at the mid-stent location. The stent lengths are given below each figure. γ = 0.0202 for all three figures.

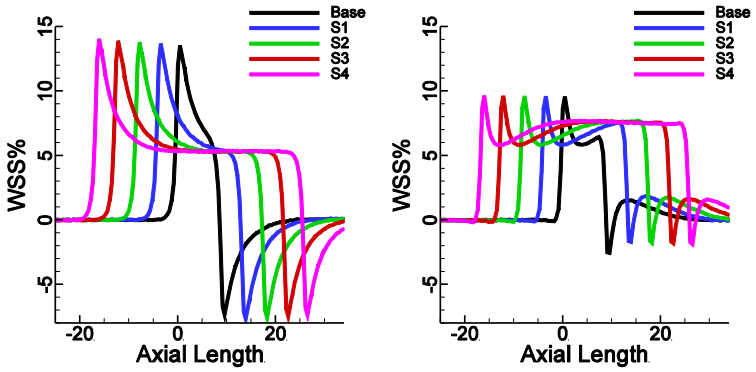

(a) Inner **(b) Outer**

Figure 7.9 Percentage change in time averaged WSS with respect to the unstented vessel at (a) Inner edge (b) Outer edge. The total stent lengths are: base – 9.8, S1 – 19.6, S2 – 29.4, S3 – 39.2, S4 – 49.0.

Fig. 7.9 shows the change in WSS with respect to the unstented helical tube. Increasing the stent length tends to increase WSS nominally. The decrease and increase of $\%U_{wall}$ at the proximal and distal ends respectively are offset by the relatively higher and lower deformation at the proximal ends and distal ends. As seen from the near wall velocity changes, a shorter stent leads to a higher WSS change at the mid-stent location, at the inner wall. Thus to summarize, increasing the stent length:

- decreases the near wall velocities at the proximal end and increases the same at the distal end
- increases the strength of the clockwise rotating secondary vortex and decreases the strength of the counter clockwise rotating vortex nominally
- reduces the WSS at the inner mid-stent region and increases the WSS at the outer edge
- increases the total area exposed to WSS variation and affects pressure reflection characteristics

Overexpansion Effects

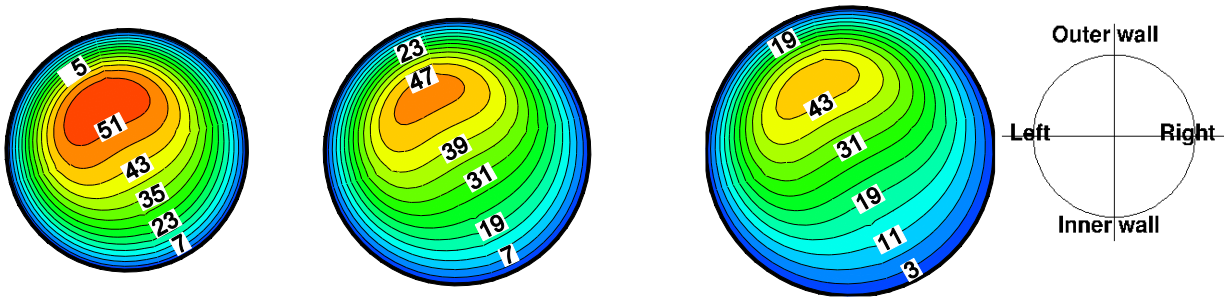

(a) Baseline = 0.0% **(b) A2 = 10.0%** **(c) A4 = 20.0%**

Figure 7.10 Axial velocity profile at mid-stent location for varying overexpansion. The stent overexpansion are given below each figure. $\gamma = 0.0202$ for all three figures.

To study the effects of overexpansion of the artery during stent deployment, four levels of change in arterial radius are studied: 5% (A1), 10% (A2), 15% (A3) and 20% (A4). The corresponding changes in cross section areas are 10.25%, 21%, 32.25% and 44%. It should be noted that the area transition matches the transition of the elastic modulus. Thus the changes in the flow field seen are due to both changes in cross-sectional area and compliance. The overexpansion of the artery causes drastic changes in the arterial geometry, creating a divergent channel at the proximal end and a convergent channel at the distal end of the stent. Thus, the primary and secondary flow fields are drastically affected as will be shown in Figs. 7.10 and 7.11.

Fig. 7.10 shows the axial velocity profile at the mid-stent location, for the baseline, A2 and A4. With an increase of the cross section, the axial velocity drops in the

stented region. This is in contrast to the unexpanded stented baseline, where the axial velocity tends to increase due to the reduced distensibility of the artery caused by the increased elastic modulus of the artery. Even a minimum overexpansion of 5% (A1) causes the axial velocity to drop by 5.8% with respect to the baseline stented helical tube (not shown). The secondary flow field is also drastically different when there is an overexpansion of the artery as seen in Fig. 7.11. For example, the counter-clockwise rotating vortex strength drops by 22% with respect to the baseline stent and the clockwise rotating vortex strength increases by 4.6% for A1 (not shown).

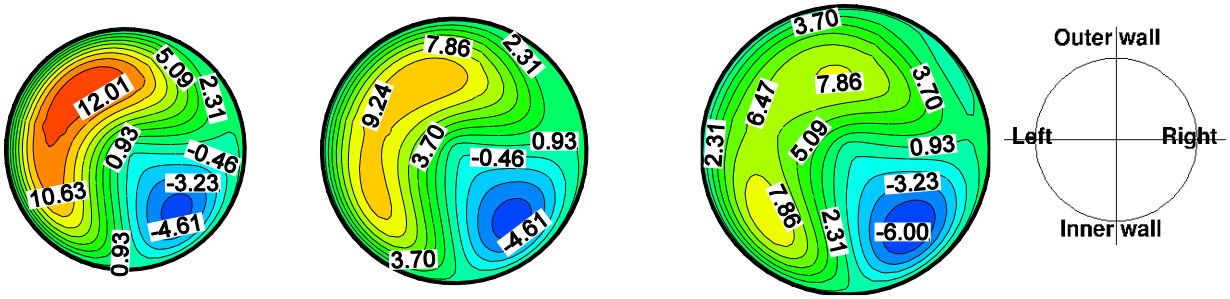

(a) 0.0% **(b)10.0%** **(c) 20.0%**

Figure 7.11 Contours of secondary stream at mid-stent location for varying overexpansion, at T = 3.15. The stent overexpansion are given below each figure. $\gamma = 0.0202$ for all three figures.

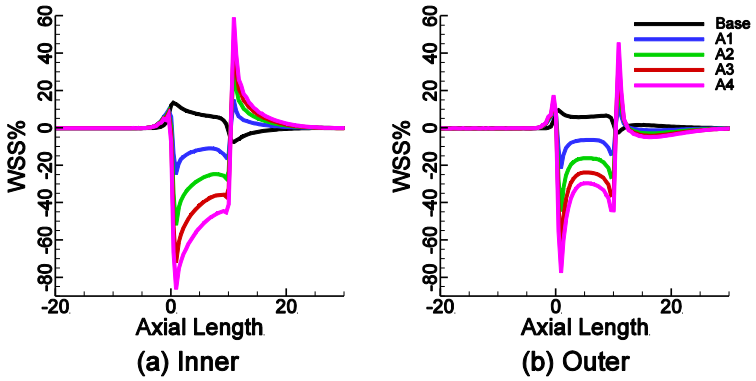

Figure 7.12 Percentage change in time averaged WSS with respect to the unstented vessel at (a) Inner edge (b) Outer edge. The radius changes are: base – 0.0%, A1 – 5.0%, A2 – 10.0%, A3 – 15.0%, A4 – 20.0%.

From Figs 7.10-7.11, even a 5% change in arterial radius causes drastic changes in the flow field and affects the WSS as seen in Fig. 7.12. The drop in axial velocity at the proximal end due to the overexpansion causes a drop in WSS. A corresponding

increase in velocity after the overexpansion causes the wall shear stress to increase at the post-distal region. For the baseline case with no overexpansion, WSS increases at the inner proximal end. By comparison, even an overexpansion in radius of 5% (A1) causes the WSS to drop significantly (24.6%) with respect to the unstented tube at the inner proximal end. Due to the movement induced centrifugal forces, the outer edge experiences slightly lower changes in WSS. It has long been hypothesized that low wall shear stress and the resultant stagnation of blood permit increased uptake of atherogenic blood particles as a result of increased residence time and thus lead to intimal thickening[81, 91, 92]. If this hypothesis is used, the overexpansion of the artery during stent placement would result in higher intimal thickening when compared to a stent placed with no overexpansion. Thus to summarize, increasing the overexpansion:

- decreases the axial velocity and secondary flow strength
- decreases the WSS in the stented region

Discussion

Hemodynamic Parameters

The following hemodynamic quantities are tracked to compare the various parameters studied in this work: pressure wave reflections, percentage circumferential area exposed to a WSS threshold change and circumferentially averaged WSS at the proximal end of the stent.

Flows in compliant vessels propagate in the form of waves and are characterized by pressure wave reflections due to obstacles. In this study, the reflection emanate from of elastic modulus variations due to the presence of stents. The contribution of pressure wave reflections to coronary artery disease is well known [33] .The time averaged pressure wave reflection caused by the presence of the stent, measured upstream of the stent for the various cases of interest studied in this work is presented in Fig. 7.13. In general, when there is no overexpansion (T1-T4 and S1-S4), the stent causes a decrease in arterial deformation in the stented region (narrowing with respect to the unstented vessel). This leads to a positive reflection coefficient and thus an increase in upstream

pressure reflection. An overexpansion (A1-A4), leads to a negative reflection coefficient and thus a decrease in upstream pressure reflection.

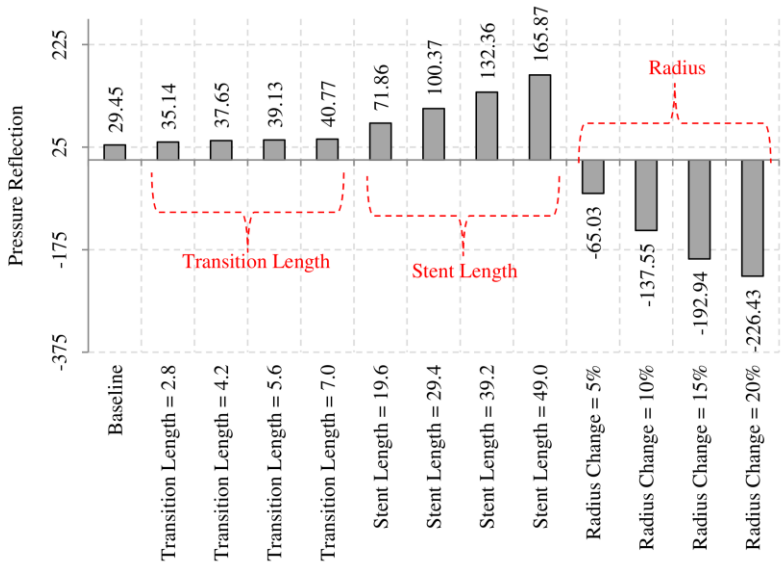

Figure 7.13 Reflected pressure upstream of the stent for all the cases of interest. The parameters are changed independently for each case.

Fig. 7.14a and 7.14b shows of the percentage circumferential area exposed to a WSS change greater than ±5.0% and ±10.0% respectively, with respect to the unstented artery for each of the parameter studied. Increasing the stent length and transition length increases the area exposed to a WSS change greater than ±5.0%. This is due to the corresponding increase in total stent length. When the area exposed to a WSS change greater than ±10.0% is considered, the dominant effect of overexpansion compared to stent length and transition length becomes apparent. This is almost constant when the stent length is changed, as the areas exposed to greater than 10% occur predominantly at the proximal and distal ends. The area exposed to WSS greater than ±10.0% decreases with increasing transition length as evident from Fig. 7.6. Fig. 7.15 provides a summary of the circumferentially averaged WSS at the proximal stent location with respect to the unstented vessel, a measure of the local hemodynamic changes. Similar variations of circumferential averaged WSS were observed at the distal end. From Figs. 7.13-7.15, the overexpansion of the artery has a dominant effect, compared to the stent length and transition length effects.

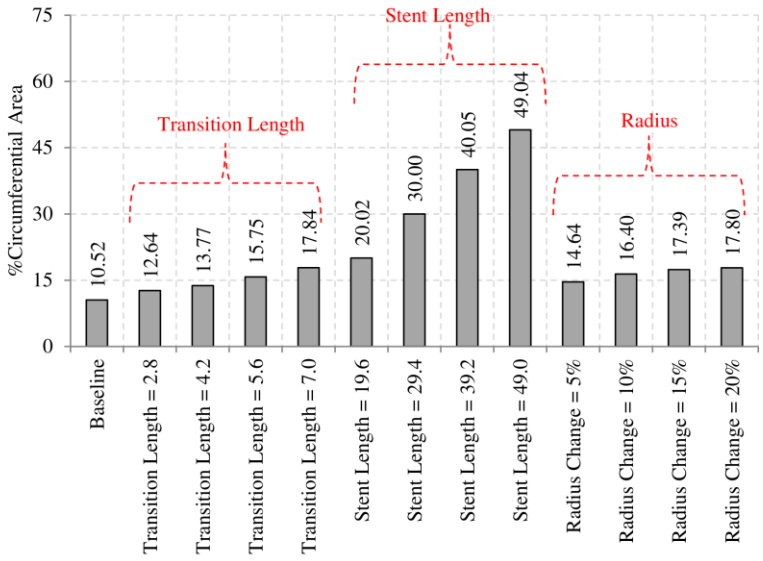

(a) ±5%

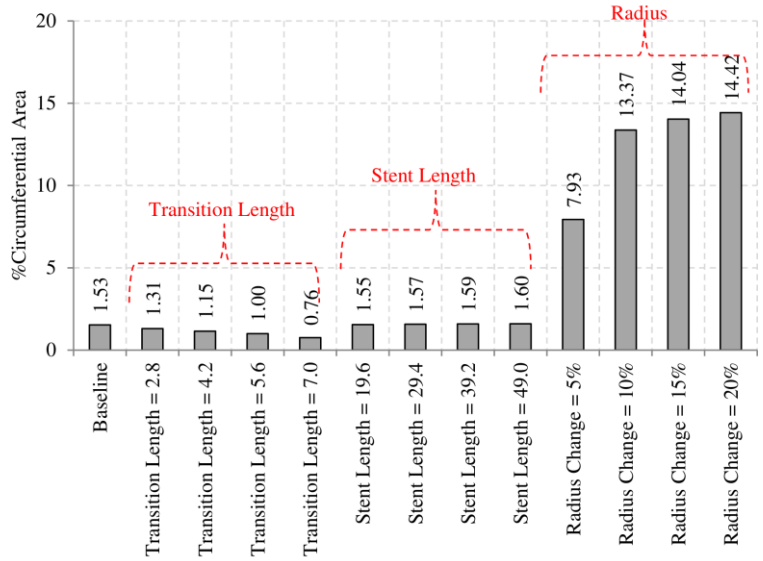

(b) ±10%

Figure 7.14 Percentage circumferential area exposed to a WSS change greater than (a) ±5.0% and (b) ±10.0% with respect to the unstented artery for each of the parameters studied. The parameters are changed independently for each case.

Effects of Stent Transition Length, Stent Length and Overexpansion

The results shown in the previous section demonstrate that variation in stent design and stent deployment can have a significant effect on the magnitude of the WSS created by the presence of the stent. For the cases tested here this effect could be as high as 80% with respect to the unstented artery. Thus, if a reduction in the WSS change and

reduction in pressure wave reflection with respect to an unstented healthy vessel caused by a stent is desired, several factors should be considered in its design and deployment.

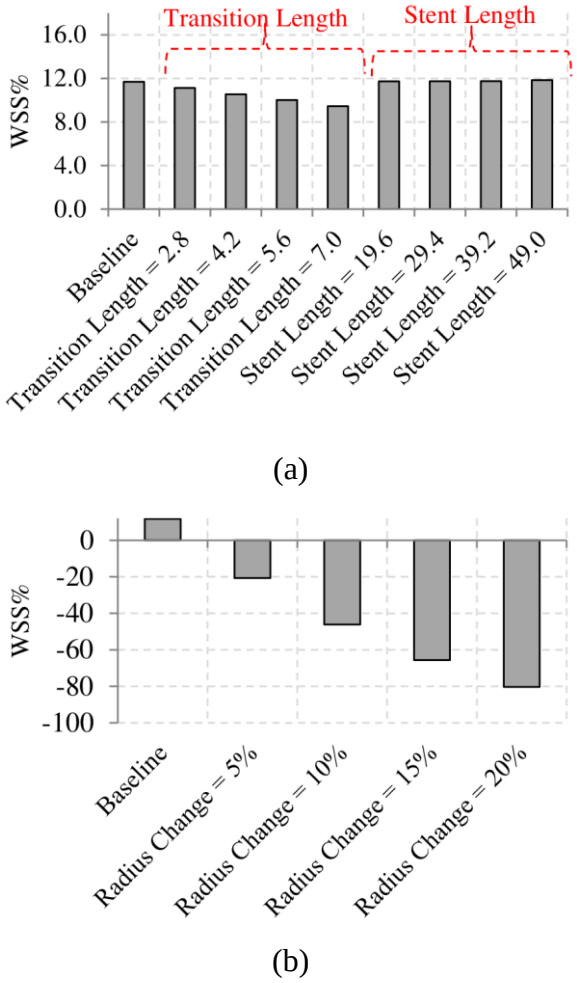

Figure 7.15 Relative change in circumferentially averaged WSS at the proximal location with respect to the unstented artery for (a) changes in transition length and stent length and (b) changes in overexpansion radius.

The first such parameter was considered is the stent transition length. Berry[46] showed that a gradual transition region can act to reduce the mechanical wall stresses imposed upon the artery, possibly improving the acute and chronic response of the vessel to the procedure. One of the goals of this research was to determine if a similar effect is seen in near wall hemodynamics. Charonko et al[33] looked at the pressure wave reflection for various stent transition lengths using a one-dimensional analysis for a straight stationary vessel. The maximum transition length studied was 1/5 of the total stent length. They concluded that their results showed no benefit to a gradual compliance

transition region at the ends of the stent. The magnitude of the reflection was unaffected by the transition zone lengths.

In the current study, the transition length was increased 2, 3, 4 and 5 times of the baseline value of 1/5 of the stent length. When the circumferentially averaged WSS at the proximal end for the various transition lengths studied is compared to the baseline stent, the changes are nominal compared to the other parameters studied in this work, in Fig. 7.15. This might point to the secondary role played by transition length to say stent length in terms of contributing towards restenosis. But, when the stent coverage length (constant elastic modulus ratio of 5) is held constant and the transition length is varied by itself, the WSS changes are significant. For example when the transition length is doubled to 2.8 units (T1), we see that the WSS (Fig. 7.15) drops by 4.9% with respect to the baseline stent. The WSS change at the proximal end drops with increasing transition length. It should be noted that when the transition length is increased, the total stent length increases, even though the coverage length is constant. This causes an increase in the reflected pressure in Fig. 7.13. This is also evident from the increase in area exposed to a WSS change greater than ±5.0% in Fig. 7.14a.

For case T4 in Table. 7.1, the total stent length is 21.0 units and is comparable to S1 where the total stent length is 18.2. The transition lengths for T4 and S1 are 7 units and 1.4 units respectively. Thus appraisal of the pressure wave reflection for these two cases might provide an insight on the effect of transition lengths. For T4, the pressure wave reflection changes by 38.4% and for S1, the pressure wave reflection changes by 144%, with respect to the baseline stent. Even though the total stent length differs by about 13.3%, the difference in pressure wave reflection is significant. Thus the transition length does seem to reduce the pressure wave reflection upstream of the stent. When the change in circumferentially averaged WSS at the proximal location with respect to the unstented artery at the proximal end is compared in Fig. 7.15, the effect of the transition length again becomes clear. WSS drops by 19.2% for T4 with respect to the baseline stent, compared to S1 when WSS does not change much with respect to the baseline stent.

The second factor that should be considered is the total length of the stent chosen for implantation. It is clear from Fig. 7.13 and 7.14a that the pressure reflection and the

percentage change in circumferential area exposed to a WSS change greater than ±5.0% is proportional to the stent length. This reinforces the results of several clinical studies that found a relationship between the length of the implanted stent and restenosis [42-45], where an increase in stent length increased restenosis rates.

The third parameter studied in the current work is the overexpansion of the artery after the placement of the stent. In order to prevent the problems associated with stent under-expansion and subsequent restenosis, it is recommended to over-expand the cross section of the stented region by at least 10% [47, 48]. But recent studies have shown that an aggressive overexpansion might lead to neointimal hyperplasia and might be counterproductive. Thus one of the objectives of the current work was to look at the effects of overexpansion of the artery after the placement of the stent purely from a fluid dynamic standpoint. For a cross-sectional area overexpansion of 10.25% (A1), the upstream pressure wave reflection drops by 320.8% with respect to the unexpanded baseline (Fig. 16). The percentage change in circumferential area exposed to a WSS change of ±5.0% increases, even though the total stent lengths are identical with the unexpanded baseline (Fig. 7.14a). When the area exposed to a WSS change greater than ±10.0% is considered, the dominant effect of the overexpansion becomes apparent, compared to the stent length and the stent transition length. WSS% at the proximal end (Fig. 7.15), which is an indicator of local hemodynamics, also significantly decreases. The importance of the drop in axial velocity and secondary flow strength due to the change in area caused by the overexpansion becomes clear.

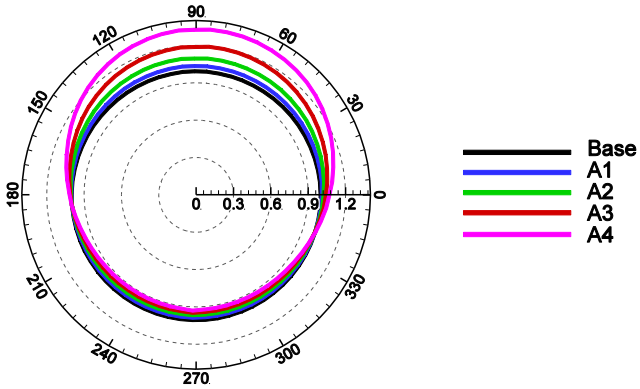

Figure 7.16 Normalized Intimal thickness with respect to the unstented helical tube calculated based on Friedman et al. [19] for changes in overexpansion area. The inner edge is located at 90° and the outer edge is located at 270°.

We use our results of WSS reduction caused by overexpansion to predict the intimal thickening. Friedman et al. [86] presented an empirical relationship between the observed shear rates in arterial casts and measured intimal thickness at 163 sites for arterial sections of various ages. They observed that the vessels subject to lower shear rates became thicker in older vessels at a slower rate. The opposite effect was seen in younger vessels, where the vessels become thicker when the shear rates increase. Based on data analysis, the intimal thickness was expressed as shown in Eq. (7.1)

$$\delta(s,T) = h(1+\alpha(s-1))e^{\frac{\beta(s-1)}{s}}\left(1-e^{-Te^{\frac{\beta(s-1)}{s}}}\right) \qquad 7.1$$

Here, δ is the intimal thickness, s is the shear rate normalized with respect to the average shear rate, T is the biological age parameter of the vessel, h is the thickness of the intimal layer exposed to average shear. The α parameter is the measure of the sensitivity of the uptake process to shear rate and β is the activation energy for the process that retards intimal thickening. Using Eq. (8), we calculated the intimal thickness (δ) using the shear rates obtained from the current simulation results to find the effect of overexpansion on intimal thickness. Following [86], α is set to 0.982 and β is set to 1.847. The biological age T is set to 6 units. The normalized intimal thickness ratio with respect to the unstented helical tube at the proximal end thus obtained is shown in Fig. 19, where the inner wall is indicated by 90° and the outer wall is indicated by 270°. As shown by the WSS and secondary flow fields presented in the preceding sections, δ is more pronounced at the inner wall than at the outer wall for all the cases. From Fig. 7.16, we can see that the intimal thickness is 1.33 times the unstented value at the inner edge.

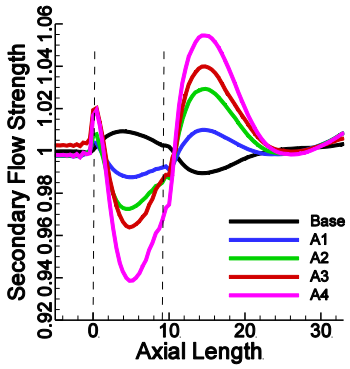

Figure 7.17 Variation of secondary flow field strength with respect to the unstented helical tube at T = 3.15 for overexpansion cases.

We now present the effects of overexpansion on the flow downstream of the stent as the observed downstream stenosis [93] in stented coronary arteries might be due to flow disturbances introduced by the presence of the over-expanded stented section. Thus to characterize the disturbance of the flow downstream due to stent overexpansion, post stent, the secondary flow field strength is calculated as defined in Eq. (7.2).

$$S = \frac{Max\left[|u_r|, |u_\theta|\right]}{|u_{s,\max}|} \qquad \textbf{7.2}$$

Here u_s, u_r and u_θ are the axial, radial and circumferential velocity components. The secondary flow strength ratio with respect to the unstented helical tube at T = 3.15 calculated for the stent length cases is shown in Fig. 20. The proximal and distal ends are indicated by the dotted lines. For the baseline stent, *S* increases at the proximal end. As we move towards the distal end, *S* decreases and falls below the unstented value. It is lower than the unstented value for about one stent length after which the secondary flow strength becomes higher than the unstented helical tube. When *S* is calculated for cases with an overexpansion, at the proximal end of the stent, S is lower with respect to the unstented helical tube for all cases (A1-A4). At the post-distal ends, due to the relative decrease in cross-sectional area, we see an increase in *S*. In fact S is as high as 5.4% compared to the unstented value for A4. This increase would affect downstream fluid residence times.

Limitations of the Current Work

The present study is subject to several assumptions, generalizations and limitations that are discussed below. First the arterial geometry was assumed to be a helical tube and this artery was assumed to rest on a cylindrical heart. Here the main aim was to obtain results of general applicability amenable to quantitative analysis. The effect of the post stent injury caused to the artery that would contribute to restenosis is not considered. However, the objective of the current study was to isolate the effects of the change in elastic modulus and deployment options due to the presence of an idealized stent on the flow and on the hemodynamic parameters that have been implicated in restenosis. This study does not consider the effect of changes in mechanical stresses in the vessel wall that might be important and affect remodeling. However, this effect is compounded by the

combined hemodynamic changes, and literature suggesting that changes in hemodynamics would affect stenosis is extensive. Yet, how the above mentioned parameters affects the local hemodynamics is not understood completely. The present study aims to help understand their effects. The wall model used to calculate the radial deformations due to the fluid flow is a cylindrical membrane model. Only the radial deformation term is considered, due to the fact that the radial forces (pressure) dominate the other fluid stress components and thus would contribute to a larger extent to the flow disturbances due to the presence of the stent. This model has been used extensively in the literature [56, 57]. This model predicts the wall shear stress accurately and can thus be used as a good predictor of local hemodynamic function. An exponential transition of the elastic modulus is used, as indicated in Fig. 4. Care was taken to make sure that the elastic modulus transition was continuous and smooth. A future extension of this work would be to include transition lengths based on experimental measurements.

Conclusion

Systematic three-dimensional CFD calculations have been performed for pulsatile flow with moving wall boundaries in simplified coronary arteries, using physiologically relevant flow waveforms, with the objective of studying the effect of transition length, stent length and overexpansion on hemodynamics. The curvature and the torsion of the helical coronary artery were changed with time and this was done to mimic the movement of an idealized heart on which the generalized artery rests. Increasing the transition length led to a decrease in proximal and distal end WSS values and a lower pressure reflection compared to cases with similar total stent length. Thus an increase in transition length reduces near wall hemodynamic changes. Increasing the stent length tends to increase the pressure wave reflections and area exposed to a WSS change greater than ±5.0% with respect to unstented artery. Increasing the overexpansion of the artery causes the WSS to drop significantly. The intimal thickness predicted using Friedman et al. [86] was found to be 1.33 times higher than the unstented helical tube, at the inner edge for the maximum overexpansion studied in this work. The downstream secondary flow strength is also higher when a stent overexpansion is present. Thus from a fluid dynamic standpoint, the overexpansion of stented section can lead to adverse flow

conditions. Thus to summarize the results from this work, decreasing transition length, increasing stent length and increasing the overexpansion would lead to higher variations in WSS.

8. Effect of Helical Geometry and Movement on Hemodynamics

This chapter contrasts the flow and its hemodynamic effects in a moving helical tube versus a straight tube, to bring out the importance of the effects of the curved geometry of the arteries and the motion that they experience. Comparisons are made between the stented (Es/Eus = 5) helical tube subject to changes in curvature and torsion, a stented stationary helical tube, and a straight non-moving tube of the same length. All the cases were subject to the same pulsatile boundary conditions. The key difference seen between the cases is the existence of the secondary flow field induced by the centrifugal forces in helical tubes. This causes a shift in the axial velocities towards the outer wall.

Boundary Conditions

The applied pulsatile boundary conditions for both the cases are shown in Fig. 6.4, for healthy resting conditions. The values used fall within observed physiological variations due to various biological factors. The peak Reynolds number is 191.6 and the near wall grid resolution is 8×10^{-3}. The temporal discretization used for the calculations was 5×10^{-4}, selected to maintain the CFL number less than 0.1. The convergence criteria for the pressure and momentum equations are set to 10^{-6} at each time step. The above simulation parameters apply for both the straight non-moving elastic tube and the moving helical tube. In order to study the effects of the motion of the myocardium on the hemodynamics, the curvature and torsion of the helix is changed as shown in Fig. 6.2 and Fig. 6.3. This condition together with the flow conditions in Fig. 6.4 provides a realistic correlation with actual flow conditions experienced by an idealized left main coronary artery.

Results and Discussion

Fig. 8.1 shows the axial velocity profiles at $44a^*$ from the inlet for the stationary straight tube, stationary helical tube, and the moving helical tube, at T = 3.15. The progression of the axial velocity profile from a centered symmetric profile in a straight tube to a distorted profile in the presence of curvature and torsion can be clearly seen. This flattening of the parabolic profile increases as the effects of the centrifugal force

increases and the axial velocity is rotated towards the left. This has a direct impact on the distribution of WSS along the length of the tube.

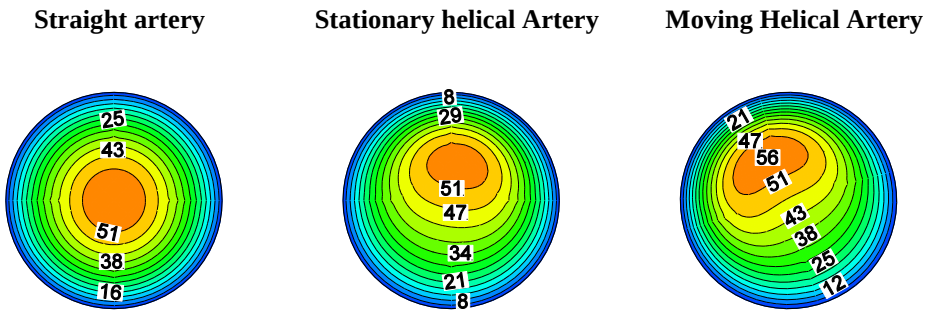

Figure 8.1 Variation of axial velocity for the straight, stationary helical and moving helical stented artery at T = 3.15. γ is 0.0277 and 0.0202 for the stationary helical tube and the moving helical tube respectively.

When the cross plane pressure is calculated, no variation is seen for the stationary straight tube, compared to the moving and stationary helical tubes. Thus by comparison, the secondary stream function in Fig. 8.2a for the stationary straight tube is very low, almost non-existent. In the stationary helical configuration, a pair of counter-rotating vortices is formed with the clockwise rotating vortex on the right side of higher strength compared to the counter-clockwise vortex. For the moving helical tube, when γ is still lower, the secondary and axial boundary layers develop leading to the formation of a dominant vortex seen in Fig. 8.2c. This secondary flow pattern is known to form due to the centrifugally-induced pressure gradient, driving the slow moving fluid near the wall inside and the faster fluid from the center to the outside.

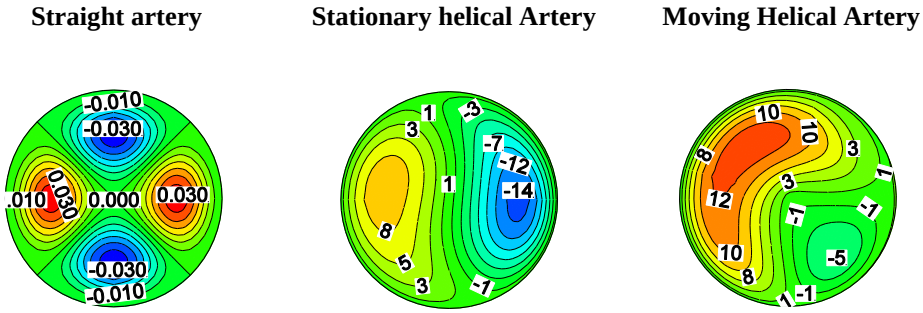

Figure 8.2 Variation of secondary flow field for the straight, stationary helical and moving helical stented artery at T = 3.15. γ is 0.0277 and 0.0202 for the stationary helical tube and the moving helical tube respectively.

The variation of WSS with respect to the straight non-moving stented artery is shown in Fig. 8.3, at the inner, outer, right and left edges. The proximal end of the stent is located at the axial location of 0.0. In general, a clear increase in WSS at the proximal end where elastic modulus changes from uniform compliance to a higher value. This is reversed at the distal end, as the vessel expands more after the stent, leading to a decrease in axial velocity. The variation of WSS is the same for all locations on the wall for the straight helical tube, due to the centered symmetrical axial velocity profile variation at all times. WSS changes are the highest at the inner edge and lowest at the outer edge for the helical tube, either stationary or moving. Due to the presence of the secondary flows and the distortion of the axial velocity profile, both the stationary and moving helical vessels encounter a sharp decrease in wall shear stress at the inner wall followed by a large increase at the outer wall over the length of the vessel. For the moving helical tube, WSS is higher at the outer edge and lower at the inner edge compared to the stationary helical tube, leading to a larger change in WSS at both sides. Similar trends are observed at the left and right edges.

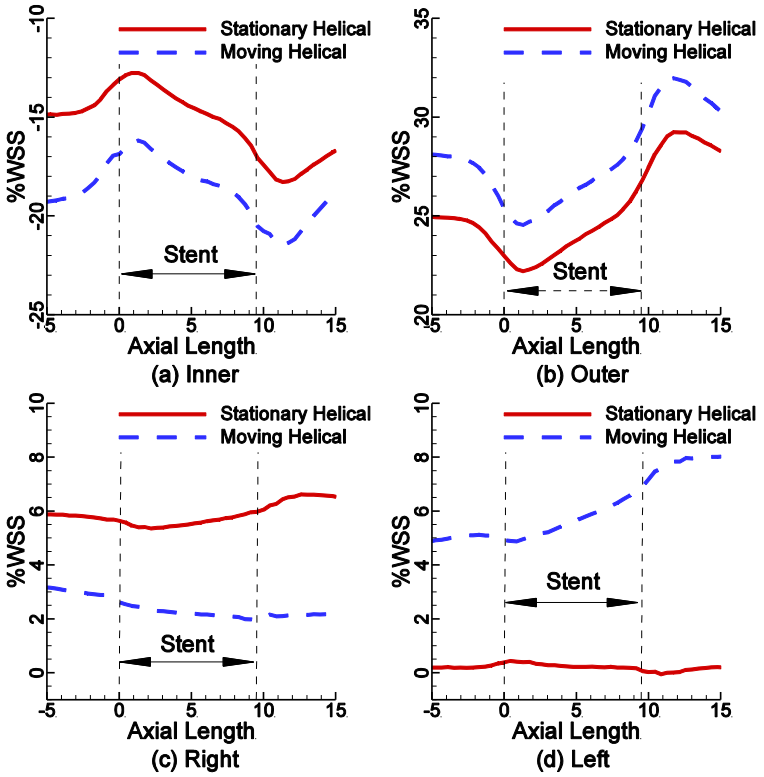

Figure 8.3 Variation of WSS for the stationary helical and moving helical stented artery with respect to the stationary straight tube at the (a) inner (b) outer (c) right and (d) left edges.

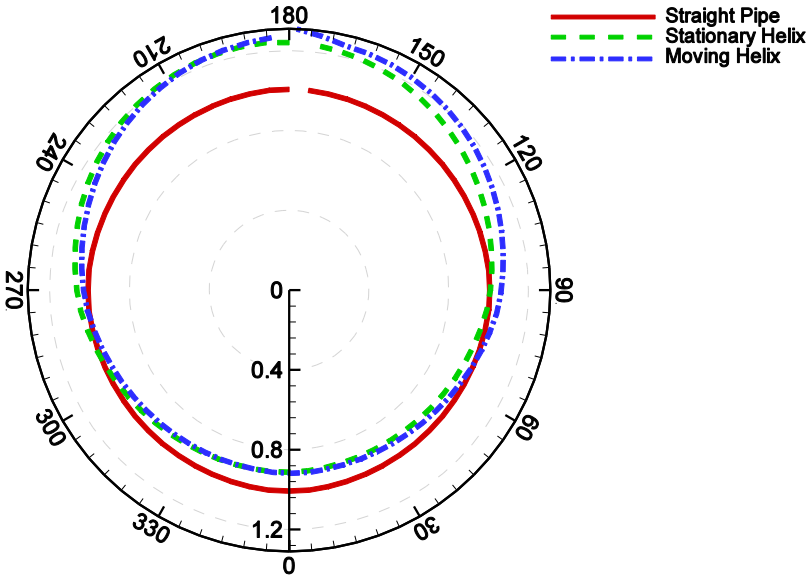

Figure 8.4 Intimal thickness comparison

Shown in Fig. 8.5 is the intimal thickness of at the proximal end for the stationary straight tube, stationary helical tube and the helical moving tube, calculated using the empirical relationship obtained by Friedman et al. [86]. In this figure, 180° is the inner edge and 0°

is the outer edge. The values shown are normalized with respect to the average intimal thickness. It can be seen that for the straight non-moving tube, the intimal thickness is uniform at all locations. For helical tubes, the intimal thickness is higher at the inner edge and lower at the outer edge, mainly due to the secondary flow field and the shifting of the axial velocity profile towards the outer wall. Comparing the intimal thickness values between the stationary helical tube and the moving tube, the effect of the dominant vortex formation becomes apparent. For the stationary helical tube, the clockwise vortex on the right side is stronger, leading to a higher WSS distribution on that side. Thus the intimal thickness calculated is lower on the right side for the stationary helical tube. For the moving helical tube, a dominant vortex form on the left side, leading to higher WSS value on that side. This causes the seen lower intimal thickness on the left side, compared to the right side.

Conclusion

From the above discussion, the helical tube geometry has a large impact on the WSS by modifying the axial velocity profile which is the primary WSS producing mechanism. Thus it becomes apparent that to accurately predict the distribution of WSS and stent efficacy in coronary arteries, the curved geometry and the movement needs to be considered.

9. Conclusions

As stated in the introduction, the main purpose of this work is to quantify the effect of the compliance change due to stenting in coronary arteries, including the effects of the deformation of the artery under the influence of fluid forces (FSI) and the induced motion of the artery due to the motion of the myocardium itself. This study also quantifies the effect of stent parameters: length, transition length and expansion area, on hemodynamics. The conclusions from the current work for each of the objectives stated in the introduction are presented below.

Effect of Compliance Mismatch on Hemodynamics

It is seen that as the elastic modulus ratio increases, the size and the residence times of the recirculation zones and WSS and OSI increase. This increase is more dominant at the compliance discontinuities. Thus we conclude that the changes in elastic modulus between the stented and unstented artery is one of the factors that would affect endothelial response in stented arteries.

Flow Characterization Due to Dynamic Motion of a Generalized CA

The helical geometry of the artery results in centrifugal and torsional forces acting on the flow, which produce secondary flows in the cross-section. It is found that centrifugal forces dominate over torsional forces and have a much larger effect on the flow. The secondary flow leads to a distortion of the axial velocity profile which directly influences the wall shear stress. The secondary flows are also sensitive to the motion of the artery. Thus we conclude that the motion of the helical artery makes an important contribution towards the hemodynamics in coronary arteries.

Effect of Compliance Change Due to Stenting in a Generalized CA

The changes in compliance and curvature and torsion cause critical deviations in local pressure and velocity gradients and secondary flow patterns. The pressure reflection upstream increases with increasing elastic modulus ratio and increasing curvature of the artery. We also demonstrate that the movement of the artery due to the movement of the

myocardium cannot be ignored and needs to be considered to accurately predict the effects of compliance discontinuities.

Effect of Stent Transition Length, Stent Length and Overexpansion

It was found that decreasing transition length, increasing stent length and increasing the overexpansion affects the local hemodynamics adversely and leads to higher variations in WSS. Stent overexpansion has a dominant effect compared to changes in stent length and stent transition length. The intimal thickness predicted was found to be 1.33 times higher than the unstented helical tube, at the inner edge for a stent expansion ratio of 0.92. The downstream secondary flow strength is also higher when stent overexpansion is present. Thus from a fluid dynamic standpoint, the overexpansion of stented section can lead to adverse flow conditions.

References

[1] Berger, S. A., and Jou, L. D., 2000, "Flows in stenotic vessels," Annual Review of Fluid Mechanics, 32, pp. 347-382.

[2] Ku, D. N., 1997, "Blood flow in arteries," Annual Review of Fluid Mechanics, 29, pp. 399-434.

[3] Caro, C. G., Fitz-Gerald, J. M., and Schroter, R. C., 1971, "Atheroma and Arterial Wall Shear Observation Correlation and Proposal of a Shear Dependant Mass Transfer Mechanism for Atherogenesis," Proceedings of the Royal Society of London Series B Biological Sciences, 177(1046), pp. 109-159.

[4] Wootton, D. M., and Ku, D. N., 1999, "Fluid mechanics of vascular systems, diseases, and thrombosis," Annual Review of Biomedical Engineering, 1, pp. 299-329.

[5] Wang, C. Y., 1981, "On the low-Reynolds-number flow in a helical pipe," Journal of Fluid Mechanics, 108, pp. 185-194.

[6] Germano, M., 1982, "On the effect of torsion on a helical pipe flow," Journal of Fluid Mechanics, 125, pp. 1-8.

[7] Kao, H. C., 1987, "Torsion effect on fully developed flow in a helical pipe," Journal of Fluid Mechanics, 184, pp. 335-356.

[8] Yamamoto, K., Yanase, S., and Yoshida, T., 1994, "Torsion effect on the flow in a helical pipe," Fluid Dynamics Research, 14, pp. 259-273.

[9] Berger, S. A., Talbot, L., and Yao, L. S., 1983, "Flow in curved pipes," Annual review of fluid mechanics. Vol.15, Annual Reviews, Palo Alto, CA, USA, pp. 461-512.

[10] Gammack, D., and Hydon, P. E., 2001, "Flow in pipes with non-uniform curvature and torsion," Journal of Fluid Mechanics, 433, pp. 357-382.

[11] Peterson, S. D., and Plesniak, M. W., 2008, "The influence of inlet velocity profile and secondary flow on pulsatile flow in a model artery with stenosis," Journal of Fluid Mechanics, 616, pp. 263-301.

[12] Moore Jr, J. E., Guggenheim, N., Delfino, A., Doriot, P. A., Dorsaz, P. A., Rutishhauser, W., and Meister, J. J., 1994, "Preliminary analysis of the effects of blood vessel movement on blood flow patterns in the coronary arteries," Journal of Biomechanical Engineering, 116, pp. 302-306.

[13] Santamarina, A., Weydahl, E., Siegel, J. M., Jr., and Moore, J. E., Jr., 1998, "Computational analysis of flow in a curved tube model of the coronary arteries: effects of time-varying curvature," Annals of Biomedical Engineering, 26, pp. 944-954.

[14] Moore, J. E., Weydahl, E. S., and Santamarina, A., 2001, "Frequency dependence of dynamic curvature effects on flow through coronary arteries," Transactions of the ASME. Journal of Biomechanical Engineering, 123, pp. 129-133.

[15] Prosi, M., Perktold, K., Ding, Z., and Friedman, M. H., 2004, "Influence of curvature dynamics on pulsatile coronary artery flow in a realistic bifurcation model," Journal of Biomechanics, 37, pp. 1767-1775.

[16] Zeng, D., Ding, Z., Friedman, M. H., and Ethier, C. R., 2003, "Effects of cardiac motion on right coronary artery hemodynamics," Annals of Biomedical Engineering, 31.

[17] Theodorakakos, A., 2008, "Simulation of cardiac motion on non-Newtonian, pulsating flow development in the human left anterior descending coronary artery," Physics in medicine & biology, 53(18), pp. 4875-4892.

[18] Torii, R., 2009, "The effect of dynamic vessel motion on haemodynamic parameters in the right coronary artery: a combined MR and CFD study," British journal of radiology, 82(special issue 1), pp. S24-S32.

[19] Ding, Z. H., and Friedman, M. H., 2000, "Dynamics of human coronary arterial motion and its potential role in coronary atherogenesis," Journal of Biomechanical Engineering-Transactions of the Asme, 122(5), pp. 488-492.

[20] Ding, Z. H., and Friedman, M. H., 2000, "Quantification of 3-D coronary arterial motion using clinical biplane cineangiograms," International Journal of Cardiac Imaging, 16(5), pp. 331-346.

[21] Zhu, H., Ding, Z. H., Piana, R. N., Gehrig, T. R., and Friedman, M. H., 2009, "Cataloguing the geometry of the human coronary arteries: A potential tool for predicting risk of coronary artery disease," International Journal of Cardiology, 135(1), pp. 43-52.

[22] Brinkman, A. M., Baker, P. B., Newman, W. P., Vigorito, R., and Friedman, M. H., 1994, "Variability of human coronary-artery geometry - an angiographic study of the left anterior descending arteries of 30 autopsy hearts " Annals of Biomedical Engineering, 22(1), pp. 34-44.

[23] Berry, J. L., Moore Jr, J. E., Newman, V. S., and Routh, W. D., "In vitro flow visualization in stented arterial segments," ASME, pp. 231-232.

[24] Rachev, A., Manoach, E., Berry, J., and Moore, J. E., 2000, "Model of stress-induced geometrical remodeling of vessel segments adjacent to stents and artery/graft anastomoses," Journal of Theoretical Biology, 206(3), pp. 429-443.

[25] Rolland, P. H., Charifi, A. B., Verrier, C., Bodard, H., Friggi, A., Piquet, P., Moulin, G., and Bartoli, J. M., 1999, "Hemodynamics and wall mechanics after stent placement in swine iliac arteries: Comparative results from six stent designs," Radiology, 213(1), pp. 229-246.

[26] Stone, P. H., Coskun, A. U., Kinlay, S., Clark, M. E., Sonka, M., Wahle, A., Ilegbusi, O. J., Yeghiazarians, Y., Popma, J. J., Orav, J., Kuntz, R. E., and Feldman, C. L., 2003, "Effect of endothelial shear stress on the progression of coronary artery disease, vascular remodeling, and in-stent restenosis in humans - In vivo 6-month follow-up study," Circulation, 108(4), pp. 438-444.

[27] Pache, J., Kastrati, A., Mehilli, J., Schuhlen, H., Dotzer, F., Hausleiter, J., Fleckenstein, M., Neumann, F. J., Sattelberger, U., Schmitt, C., Muller, M., Dirschinger, J., and Schomig, A., "Intracoronary stenting and angiographic results: Strut thickness effect on restenosis outcome (ISAR-STEREO-2) trial," Proc. 51st Annual Scientific Session of the American-College-of-Cardiology, pp. 1283-1288.

[28] Ojha, M., 1994, "Wall Shear-Stress Temporal Gradient and Anastomotic Intimal Hyperplasia," Circulation Research, 74(6), pp. 1227-1231.

[29] Leask, R. L., Butany, J., Johnston, K. W., Ethier, C. R., and Ojha, M., 2005, "Human saphenous vein coronary artery bypass graft morphology, geometry and hemodynamics," Annals of Biomedical Engineering, 33(3), pp. 301-309.

[30] Fry, D. L., 1968, "Acute Vascular Endothelial Changes Associated with Increased Blood Velocity Gradients," Circ. Res., 22(2), pp. 165-197.

[31] Baird, R. N., and Abbott, W. M., 1976, "Pulsatile Blood-Flow in Arterial Grafts," Lancet, 2(7992), pp. 948-949.

[32] Abbott, W. M., Megerman, J., Hasson, J. E., Litalien, G., and Warnock, D. F., 1987, "Effect of Compliance Mismatch on Vascular Graft Patency," Journal of Vascular Surgery, 5(2), pp. 376-382.

[33] Charonko, J. J., Ragab, S. A., and Vlachos, P. P., 2009, "A scaling parameter for predicting pressure wave reflection in stented arteries," Journal of Medical Devices, 3(1), p. 011006 (011010 pp.).
[34] Charonko, J., Karri, S., Schmieg, J., Prabhu, S., and Vlachos, P., 2009, "In Vitro, Time-Resolved PIV Comparison of the Effect of Stent Design on Wall Shear Stress," Annals of Biomedical Engineering, 37(7), pp. 1310-1321.
[35] Charonko, J., Karri, S., Schmieg, J., Prabhu, S., and Vlachos, P., "In Vitro Comparison of the Effect of Stent Configuration on Wall Shear Stress Using Time-resolved Particle Image Velocimetry," Annals of Biomedical Engineering, pp. 1–14.
[36] LaDisa, J. F., Guler, I., Olson, L. E., Hettrick, D. A., Kersten, J. R., Warltier, D. C., and Pagel, P. S., 2003, "Three-dimensional computational fluid dynamics modeling of alterations in coronary wall shear stress produced by stent implantation," Annals of Biomedical Engineering, 31(8), pp. 972-980.
[37] LaDisa, J. F., Hettrick, D. A., Olson, L. E., Guler, I., Gross, E. R., Kress, T. T., Kersten, J. R., Warltier, D. C., and Pagel, P. S., 2002, "Stent implantation alters coronary artery hemodynamics and wall shear stress during maximal vasodilation," Journal of Applied Physiology, 93(6), pp. 1939-1946.
[38] LaDisa, J. F., Olson, L. E., Molthen, R. C., Hettrick, D. A., Pratt, P. F., Hardel, M. D., Kersten, J. R., Warltier, D. C., and Pagel, P. S., 2005, "Alterations in wall shear stress predict sites of neointimal hyperplasia after stent implantation in rabbit iliac arteries," American Journal of Physiology-Heart and Circulatory Physiology, 288(5), pp. H2465-H2475.
[39] LaDisa, J. F., Warltier, D. C., Olson, L. E., Kersten, J. R., and Pagel, P. S., 2003, "Shear-modulated neointimal hyperplasia following stent implantation," Faseb Journal, 17(4), pp. A144-A144.
[40] Berry, J. L., Santamarina, A., Moore, J. E., Roychowdhury, S., and Routh, W. D., 2000, "Experimental and computational flow evaluation of coronary stents," Annals of Biomedical Engineering, 28(4), pp. 386-398.
[41] Yazdani, S. K., Moore, J. E., Berry, J. L., and Vlachos, P. P., 2004, "DPIV measurements of flow disturbances in stented artery models: Adverse affects of

compliance mismatch," Journal of Biomechanical Engineering-Transactions of the Asme, 126(5), pp. 559-566.

[42] Mauri, L., O'Malley, A. J., Cutlip, D. E., Ho, K. K. L., Popma, J. J., Chauhan, M. S., Baim, D. S., Cohen, D. J., and Kuntz, R. E., 2004, "Effects of stent length and lesion length on coronary restenosis," The American Journal of Cardiology, 93(11), pp. 1340-1346.

[43] Kereiakes, D., Linnemeier, T. J., Baim, D. S., Kuntz, R., O'Shaughnessy, C., Hermiller, J., Fink, S., Lansky, A., Nishimura, N., Broderick, T. M., and Popma, J., 2000, "Usefulness of stent length in predicting in-stent restenosis (the MULTI-LINK stent trials)," The American Journal of Cardiology, 86(3), pp. 336-341.

[44] Kobayashi, Y., De Gregorio, J., Kobayashi, N., Akiyama, T., Reimers, B., Finci, L., Di Mario, C., and Colombo, A., 1999, "Stented segment length as an independent predictor of restenosis," Journal of the American College of Cardiology, 34(3), pp. 651-659.

[45] Moreno, R., Fernández, C., Hernández, R., Alfonso, F., Angiolillo, D. J., Sabaté, M., Escaned, J., Bañuelos, C., Fernández-Ortiz, A., and Macaya, C., 2005, "Drug-eluting stent thrombosis: Results from a pooled analysis including 10 randomized studies," Journal of the American College of Cardiology, 45(6), pp. 954-959.

[46] Berry, J. L., Manoach, E., Mekkaoui, C., Rolland, P. H., Moore Jr, J. E., and Rachev, A., 2002, "Hemodynamics and Wall Mechanics of a Compliance Matching Stent: In Vitro and In Vivo Analysis," Journal of Vascular and Interventional Radiology, 13(1), pp. 97-105.

[47] Alfonso, F., Suarez, A., Angiolillo, D. J., Sabate, M., Escaned, J., Moreno, R., Hernandez, R., Banuelos, C., and Macaya, C., 2004, "Findings of intravascular ultrasound during acute stent thrombosis," Heart, 90(12), pp. 1455-1459.

[48] Romagnoli, E., Sangiorgi, G. M., Cosgrave, J., Guillet, E., and Colombo, A., 2008, "Drug-Eluting StentingThe Case for Post-Dilation," JACC: Cardiovascular Interventions, 1(1), pp. 22-31.

[49] Hoffmann, R., Mintz, G. S., Mehran, R., Kent, K. M., Pichard, A. D., Satler, L. F., and Leon, M. B., 1999, "Tissue proliferation within and surrounding Palmaz-Schatz

stents is dependent on the aggressiveness of stent implantation technique," The American Journal of Cardiology, 83(8), pp. 1170-1174.

[50] Russo, R. J., Silva, P. D., and Yeager, M., 2007, "Coronary artery overexpansion increases neointimal hyperplasia after stent placement in a porcine model," Heart, 93(12), pp. 1609-1615.

[51] Patel, D. J., and Vaishnav, R. N. j. a., 1980, Basic hemodynamics and its role in disease processes / by Dali J. Patel and Ramesh N. Vaishnav ; with chapters by H. Bulent Atabek ... [et al.], University Park Press, Baltimore :.

[52] Giddens, D. P., Zarins, C. K., and Glagov, S., "The role of fluid-mechanics in the localization and detection of atherosclerosis," Proc. 1993 ASME/AICHE/ASCE Summer Bioengineering Conference, Forum on the 20th Anniversary of ASME Biomechanics Symposium, ASME, pp. 588-594.

[53] Kamiya, A., Bukhari, R., and Togawa, T., 1984, "Adaptive regulation of wall shear-stress optimizing vascular tree function," Bulletin of Mathematical Biology, 46(1), pp. 127-137.

[54] Kamiya, A., and Togawa, T., 1980, "Adaptive regulation of wall shear-stress to flow change in the canine carotid artery," American Journal of Physiology, 239(1), pp. H14-H21.

[55] Selvarasu, N. K. C., Tafti, D. K., and Vlachos, P. P., 2011, "Hydrodynamic effects of compliance mismatch in stented arteries," J Biomech Eng, 133(2), p. 021008.

[56] Canic, S., Lamponi, D., Mikelic, A., and Tambaca, J., 2005, "Self-consistent effective equations modeling blood flow in medium-to-large compliant arteries," Multiscale Modeling & Simulation, 3(3), pp. 559-596.

[57] Causin, P., Gerbeau, J. F., and Nobile, F., 2005, "Added-mass effect in the design of partitioned algorithms for fluid-structure problems," Computer Methods in Applied Mechanics and Engineering, 194(42-44), pp. 4506-4527.

[58] Weber, T., Auer, J., O'Rourke, M. F., Kvas, E., Lassnig, E., Berent, R., and Eber, B., 2004, "Arterial stiffness, wave reflections, and the risk of coronary artery disease," Circulation, 109(2), pp. 184-189.

[59] Gopalakrishnan, P., and Tafti, D. K., 2009, "A parallel boundary fitted dynamic mesh solver for applications to flapping flight," Computers and Fluids, 38(8), pp. 1592-1607.
[60] Gopalakrishnan, P., D.K Tafti, 2008, "Effect of Rotation and Angle of Attack on Force Production of Flapping Flights," AIAA Journal.
[61] Gopalakrishnan, P., and Tafti, D. K., 2010, "Effect of wing flexibility on lift and thrust production in flapping flight," AIAA Journal, 48(5), pp. 865-877.
[62] Rozati, A., and Tafti, D. K., 2008, "Large-eddy simulations of leading edge film cooling. analysis of flow structures, effectiveness, and heat transfer coefficient," International Journal of Heat and Fluid Flow, 29(1), pp. 1-17.
[63] Tafti, D., 1995, "Alternate formulations for the pressure equation Laplacian on a collocated grid for solving the unsteady incompressible Navier-Stokes equations," Journal of Computational Physics, 116(1), pp. 143-153.
[64] Tafti, D., 1996, "Comparison of some upwind-biased high-order formulations with a second-order central-difference scheme for time integration of the incompressible Navier-Stokes equations," Computers & Fluids, 25(7), pp. 647-665.
[65] Tafti, D. K., "GenIDLEST - A scalable parallel computational tool for simulating complex turbulent flows," American Society of Mechanical Engineers, pp. 347-356.
[66] Tafti, D. K., 2005, "Evaluating the role of subgrid stress modeling in a ribbed duct for the internal cooling of turbine blades," International Journal of Heat and Fluid Flow, 26(1), pp. 92-104.
[67] Womersley, J. R., 1957, "An elastic tube theory of pulse transmission and oscillatory flow in mammalian arteries," U S a F Wright Air Development Center Tech Rept, pp. 56-614, 611-238.
[68] Zamir, M., 2000, The Physics of Pulsatile Flow, Springer-Verlag, New York.
[69] Santamarina, A., Weydahl, E., Siegel, J. M., Jr., and Moore, J. E., Jr., 1998, "Computational analysis of flow in a curved tube model of the coronary arteries: effects of time-varying curvature," Annals of Biomedical Engineering, 26(Copyright 1998, IEE), pp. 944-954.

[70] Zwart, B., van Werkum, J., Heestermans, A., and ten Berg, J., "Coronary Stent Thrombosis in the Current Era: Challenges and Opportunities for Treatment," Current Treatment Options in Cardiovascular Medicine, 12(1), pp. 46-57.

[71] Karri, S., 2009, "Laminar and Transitional Flow disturbances in Diseased and Stented Arteries," Ph.D Dissertation, Virginia Tech, Blacksburg.

[72] Olufsen, M. S., Peskin, C. S., Kim, W. Y., Pedersen, E. M., Nadim, A., and Larsen, J., 2000, "Numerical simulation and experimental validation of blood flow in arteries with structured-tree outflow conditions," Annals of Biomedical Engineering, 28(11), pp. 1281-1299.

[73] Canic, S., Hartley, C. J., Rosenstrauch, D., Tambaca, J., Guidoboni, G., and Mikelic, A., 2006, "Blood flow in compliant arteries: An effective viscoelastic reduced model, numerics, and experimental validation," Annals of Biomedical Engineering, 34(4), pp. 575-592.

[74] Canic, S., and Kim, E. H., 2003, "Mathematical analysis of the quasilinear effects in a hyperbolic model blood flow through compliant axi-symmetric vessels," Mathematical Methods in the Applied Sciences, 26(14), pp. 1161-1186.

[75] Canic, S., and Mikelic, A., 2003, "Effective equations modeling the flow of a viscous incompressible fluid through a long elastic tube arising in the study of blood flow through small arteries," Siam Journal on Applied Dynamical Systems, 2(3), pp. 431-463.

[76] Canic, S., Tambaca, J., Mikelic, A., Hartley, C. J., Mirkovic, D., Chavez, J., Rosenstrauch, D., and ieee, "Blood flow through axially symmetric sections of compliant vessels: new effective closed models," Proc. 26th Annual International Conference of the IEEE-Engineering-in-Medicine-and-Biology-Society, IEEE, pp. 3696-3699.

[77] Mikelic, A., Guidoboni, G., and Canic, S., 2007, "Fluid-structure interaction in a pre-stressed tube with thick elastic walls I: the stationary Stokes problem," Networks and Heterogeneous Media, 2(3), pp. 396-423.

[78] Vernhet, H., Demaria, R., Perez-Martin, A., Juan, J. M., Oliva-Lauraire, M. C., Marty-Double, C., Senac, J. P., and Dauzat, M., 2003, "Wall mechanics of the stented rabbit aorta: Long-term study and correlation with histological findings," Journal of Endovascular Therapy, 10(3), pp. 577-584.

[79] Tezduyar, T. E., Sathe, S., Schwaab, M., and Conklin, B. S., 2008, "Arterial fluid mechanics modeling with the stabilized space-time fluid-structure interaction technique," International Journal for Numerical Methods in Fluids, 57(5), pp. 601-629.

[80] Lighthill, M. J., 1963, Laminar Boundary Layers, Dover Publications Inc, New York.

[81] Lei, M., Kleinstreuer, C., and Truskey, G. A., 1995, "Numerical Investigation and Prediction of Atherogenic Sites in Branching Arteries," Journal of Biomechanical Engineering-Transactions of the Asme, 117(3), pp. 350-357.

[82] Canic, S., Tambaca, J., Mikelic, A., Hartley, C. J., Mirkovic, D., Chavez, J., and Rosenstrauch, D., 2004, "Blood flow through axially symmetric sections of compliant vessels: new effective closed models," Proc. 26th Annual International Conference of the IEEE-Engineering-in-Medicine-and-Biology-Society, IEEE, pp. 3696-3699.

[83] Shijie, L., and Masliyah, J. H., 1993, "Axially invariant laminar flow in helical pipes with a finite pitch," Journal of Fluid Mechanics, 251, pp. 315-353.

[84] Yamamoto, K., Aribowo, A., Hayamizu, Y., Hirose, T., and Kawahara, K., 2002, "Visualization of the flow in a helical pipe," Fluid Dynamics Research, 30, pp. 251-267.

[85] He, X. J., and Ku, D. N., 1996, "Pulsatile flow in the human left coronary artery bifurcation: Average conditions," Journal of Biomechanical Engineering-Transactions of the Asme, 118(1), pp. 74-82.

[86] Friedman, M. H., Deters, O. J., Bargeron, C. B., Hutchins, G. M., and Mark, F. F., 1986, "Shear-Dependent Thickening of the Human Arterial Intima," Atherosclerosis, 60(2), pp. 161-171.

[87] Kim, H. J., Vignon-Clementel, I. E., Coogan, J. S., Figueroa, C. A., Jansen, K. E., and Taylor, C. A., 2010, "Patient-specific modeling of blood flow and pressure in human coronary arteries," Annals of Biomedical Engineering, 38(10), pp. 3195-3209.

[88] Selvarasu, N. K. C., and Tafti, D. K., 2012, "Investigation of the Effects of Dynamic Change in Curvature and Torsion on Pulsatile Flow in a Helical Tube," Journal of Biomechanical Engineering, 134(7), p. 071005 (071017 pp.).

[89] Ojha, M., Leask, R. L., Butany, J., and Johnston, K. W., 2001, "Distribution of intimal and medial thickening in the human right coronary artery: a study of 17 RCAs," Atherosclerosis, 158(1), pp. 147-153.

[90] Bleasdale, R. A., Parker, K. H., and Jones, C. J. H., 2003, "Chasing the wave. Unfashionable but important new concepts in arterial wave travel," American Journal of Physiology - Heart and Circulatory Physiology, 284(6), pp. H1879-H1885.
[91] Shaaban, A. M., and Duerinckx, A. J., 2000, "Wall shear stress and early atherosclerosis: A review," American Journal of Roentgenology, 174(6), pp. 1657-1665.
[92] Glagov, S., Zarins, C., Giddens, D. P., and Ku, D. N., 1988, "Hemodynamics and Atherosclerosis - Insights and Perspectives Gained from Studies of Humar Arteries," Archives of Pathology & Laboratory Medicine, 112(10), pp. 1018-1031.
[93] Krasuski, R. A., Cater, G. M., Devendra, G. P., Wolski, K., Shishehbor, M. H., Nissen, S. E., Oberti, C., and Ellis, S. G., 2011, "Downstream coronary effects of drug-eluting stents," American Heart Journal, 162(4), pp. 764-771.e761.

Appendices

Appendix A: Macro to Post-process Time Dependent Data

The below TECPLOT macro is used to calculate the velocities in helical coordinates, the secondary stream function, vorticity flux density variation and the WSS change, based on time dependent data from the code. In the below code block, curly braces used in TECPLOT macros is replaced by <> signs, to avoid conflicts with the citation manager (EndNote). Please replace the <> signs by curly braces.

```
#-------------------------------------------------------------------------------#
#!MC 1200
# Created by Tecplot 360 build 12.2.0.9077
$!VarSet |MFBD| =
'/home/nareshcs/Documents/work_genidlest/Runs_With_JinWave_DefMov/BothCurvTors/
Emod5'
$!VarSet |DIR| =
'/home/nareshcs/Documents/work_genidlest/Runs_With_JinWave_DefMov/BothCurvTors/
Emod5/'

# counter for the file being read
$!VarSet |CURRENT| = '0'
# number of files read
$!VARSET |NUMFILES| = 125
#Time variable and offset
$!VARSET |TIME| = 0.0
$!VARSET |TIMEC| = 0.78854

#LOOP Through all the files
$!LOOP |NUMFILES|
$!VarSet |CURRENT| += 1
#Set Time variable
$!VarSet |TIME| += 0.05

$!VarSet |INPUTFILE1| = 'tec0|CURRENT|.plt'
$!VarSet |INPUTFILE2| = 'WSSAngle|CURRENT|.plt'

#Read the tecplot File
$!READDATASET  '"|DIR||INPUTFILE1|" '
  READDATAOPTION = NEW
  RESETSTYLE = YES
  INCLUDETEXT = NO
  INCLUDEGEOM = NO
  INCLUDECUSTOMLABELS = NO
  VARLOADMODE = BYNAME
  ASSIGNSTRANDIDS = YES
  INITIALPLOTTYPE = CARTESIAN3D
  VARNAMELIST = '"x" "y" "z" "u" "v" "w" "p" "t" "vor_x" "vor_y" "vor_z"
"u_eigen" "u_eigen_x" "u_eigen_y" "u_eigen_z"'

# Calculate volume at a given instant of time
$!alterdata
  equation = '<vol1>=5843.380684*cos(1*(|TIME|-|TIMEC|))-
7941.707872*sin(1*(|TIME|-|TIMEC|))'
$!alterdata
```

```
  equation = '<vol2>=4135.077472*cos(2*(|TIME|-
|TIMEC|))+1688.024115*sin(2*(|TIME|-|TIMEC|))'
$!alterdata
  equation = '<vol3>=-57.85730464*cos(3*(|TIME|-|TIMEC|))-
424.7869296*sin(3*(|TIME|-|TIMEC|))'
$!alterdata
  equation = '<vol4>=607.6803434*cos(4*(|TIME|-
|TIMEC|))+318.8142644*sin(4*(|TIME|-|TIMEC|))'
$!alterdata
  equation = '<vol5>=-844.8446829*cos(5*(|TIME|-
|TIMEC|))+356.5603767*sin(5*(|TIME|-|TIMEC|))'
$!alterdata
  equation = '<vol6>=56.65205337*cos(6*(|TIME|-|TIMEC|))-
70.58494876*sin(6*(|TIME|-|TIMEC|))'
$!alterdata
  equation = '<vol7>=-154.4602735*cos(7*(|TIME|-
|TIMEC|))+451.904645*sin(7*(|TIME|-|TIMEC|))'
$!alterdata
  equation = '<vol8>=-106.1765527*cos(8*(|TIME|-|TIMEC|))-
163.215112*sin(8*(|TIME|-|TIMEC|))'
$!alterdata
  equation = '<volshift>=7760.3923*(cos(|TIME|)*-1.0+1.0)/2.0'
$!alterdata
  equation =
'<vol>=(28307.61959+<vol1>+<vol2>+<vol3>+<vol4>+<vol5>+<vol6>+<vol7>+<vol8>)*2.
040311+<volshift>'
#Calculate the helix properties
#Arc Length
$!alterdata
  equation = '<arclen>=pi*(20**2+(60/pi)**2)**0.5'
#Radius of cylinder
$!alterdata
  equation = '<a>=(<vol>/3/pi)**(1/3)'
#Turns of helix
$!alterdata
  equation = '<turns>=(<arclen>**2-(<a>*3)**2)**0.5/pi/<a>'
#Circumfrential Raise
$!alterdata
  equation = '<b>=<a>*3/pi/<turns>'
#Curvarure and Torsion
$!alterdata
  equation = '<f>=sqrt(<a>**2+<b>**2)'
$!alterdata
  equation = '<kappa>=<a>/((<a>)**2+(<b>)**2)'
$!alterdata
  equation = '<tau>=<b>/((<a>)**2+(<b>)**2)'
#Axial coordinate
$!alterdata
  equation = '<s>=(i-1)*pi*<turns>/200'
#Centerline of helix (R)
$!alterdata
  equation = '<c1>=<a>*cos(<s>)'
$!alterdata
  equation = '<c2>=<a>*sin(<s>)'
$!alterdata
  equation = '<c3>=<b>*<s>'
#Radius of each point
$!alterdata
  equation = '<r>=sqrt((<c1>-<x>)**2+(<c2>-<y>)**2+(<c3>-<z>)**2)'
#Normal vector T
$!alterdata
  equation = '<n1>=-1*cos(<s>)'
$!alterdata
```

```
  equation = '<n2>=-1*sin(<s>)'
$!alterdata
  equation = '<n3>=0'
#Position vector of each point
$!alterdata
  equation = '<p1>=(<x>-<c1>)/<r>'
$!alterdata
  equation = '<p2>=(<y>-<c2>)/<r>'
$!alterdata
  equation = '<p3>=(<z>-<c3>)/<r>'
#Tangent vector T
$!alterdata
  equation = '<t1>=-<a>*sin(<s>)/<f>'
$!alterdata
  equation = '<t2>=<a>*cos(<s>)/<f>'
$!alterdata
  equation = '<t3>=<b>/<f>'
$!alterdata
  equation = '<normp>=sqrt((<p2>*<n3>-<p3>*<n2>)**2+(<p3>*<n1>-
<p1>*<n3>)**2+(<p1>*<n2>-<p2>*<n1>)**2)'
$!alterdata
  equation = '<dotp>=(<n1>*<p1>+<n2>*<p2>+<n3>*<p3>)'
$!alterdata
  equation = '<theta>=atan2(<normp>,<dotp>)'
$!alterdata
  equation = '<g>=1+<kappa>*<r>*sin(<theta>)'
$!alterdata
  equation = '<fact1>=0.0'
$!alterdata
  equation = '<fact2>=0.0'
#Intersection vector
$!ALTERDATA
  EQUATION = '<V1>=(<P2>*<N3>-<P3>*<N2>)'
$!ALTERDATA
  EQUATION = '<V2>=(<P3>*<N1>-<P1>*<N3>)'
$!ALTERDATA
  EQUATION = '<V3>=(<P1>*<N2>-<P2>*<N1>)'
#Find angle of the point w.r.t normal vector
$!ALTERDATA
  EQUATION = '<signdot>=<T1>*<V1>+<T2>*<V2>+<T3>*<V3>'
$!ALTERDATA
  EQUATION = '<sign>=sign(<signdot>)'
$!ALTERDATA
  EQUATION = '<theta1>=<theta>*<sign>'
#Find helical velocities
$!ALTERDATA
  EQUATION = '<A>=<kappa>/(<kappa>**2+<tau>**2)'
$!ALTERDATA
  EQUATION = '<B>=<tau>/(<kappa>**2+<tau>**2)'
$!ALTERDATA
  EQUATION = '<C>=<kappa>/sqrt(<kappa>**2+<tau>**2)'
$!ALTERDATA
  EQUATION = '<D>=<tau>/sqrt(<kappa>**2+<tau>**2)'
$!ALTERDATA
  EQUATION = '<E>=sqrt(((1-
<kappa>*<r>*cos(<theta>))**2+(<r>*<tau>)**2)/(<kappa>**2+<tau>**2))'
$!ALTERDATA
  EQUATION = '<u_s>=(-
<a>/<f>*sin(<s>))*<u>+(<a>/<f>*cos(<s>))*<v>+(<b>/<f>)*<w>'
$!ALTERDATA
  EQUATION =
'<u_r>=(sin(<theta>)*cos(<s>)+<f>*<tau>*cos(<theta>)*sin(<s>))*<u>+(sin(<theta>
)*sin(<s>)-<f>*<tau>*cos(<theta>)*cos(<s>))*<v>+(<f>*<kappa>*cos(<theta>))*<w>'
```

```
$!ALTERDATA
  EQUATION = '<u_t>=(cos(<theta>)*cos(<s>)-
<f>*<tau>*sin(<theta>)*sin(<s>))*<u>+(cos(<theta>)*sin(<s>)+<f>*<tau>*sin(<thet
a>)*cos(<s>))*<v>+(-1*<f>*<kappa>*sin(<theta>))*<w>'
$!ALTERDATA
  EQUATION = '<u_s1>=((<r>*cos(<theta1>)*sin(<s>)-
<A>*sin(<s>)+<r>*<D>*sin(<theta1>)*cos(<s>))*<u>+(-
<r>*cos(<theta1>)*cos(<s>)+<A>*cos(<s>)+<r>*<D>*sin(<theta1>)*sin(<s>))*<v>+<B>
*<w>)/<E>'
$!ALTERDATA
  EQUATION = '<u_r1>=(-
cos(<theta1>)*cos(<s>)+<D>*sin(<theta1>)*sin(<s>))*<u>+(-
cos(<theta1>)*sin(<s>)-<D>*sin(<theta1>)*cos(<s>))*<v>+<C>*sin(<s>)*<w>'
$!ALTERDATA
  EQUATION =
'<u_t1>=(sin(<theta1>)*cos(<s>)+<D>*cos(<theta1>)*sin(<s>))*<u>+(sin(<theta1>)*
sin(<s>)-<D>*cos(<theta1>)*cos(<s>))*<v>+<C>*cos(<s>)*<w>'

#Find Secondary flow field
$!ALTERDATA
  EQUATION = '<diff_us>=(<u_s>(i,j,k)-<u_s>(i,j-1,k))'
$!ALTERDATA
  EQUATION = '<diff_r>=(<r>(i,j,k)-<r>(i,j-1,k))'
$!ALTERDATA
  EQUATION = '<Q1>=<u>*cos(<s>)+<v>*sin(<s>)'
$!ALTERDATA
  EQUATION = '<Q2>=<u>*sin(<s>)-<v>*cos(<s>)'
$!ALTERDATA
  EQUATION = '<Q3>=<f>*<kappa>*<w>*sin(<theta>)'
$!ALTERDATA
  EQUATION = '<I2>=<r>*<u_t>*(1+0.5*<r>*<kappa>*sin(<theta>))'
$!ALTERDATA
  EQUATION = '<I1>=(-<r>*cos(<theta>)+<kappa>*(<r>)**2*(<theta>/2-
sin(2*<theta>)/4))*<Q1>+(<r>*<f>*<tau>*sin(<theta>)+<kappa>*(<r>)**2*<f>*<tau>/
2*sin(<theta>))*<Q2>+(<r>+<kappa>*(<r>)**2*sin(<theta>))*<Q3>'
$!ALTERDATA
  EQUATION = '<G>=1+<kappa>*<r>*sin(<theta>)'
$!ALTERDATA
  EQUATION = '<phi>=-1*<r>*<u_t>'
$!ALTERDATA
  EQUATION = '<phi1>=-1*<r>*<u_t1>'
$!ALTERDATA
  EQUATION = '<angle1>=acos(-1*<a>*cos(<s>)/<f>)'
$!ALTERDATA
  EQUATION = '<angle2>=acos(<a>*sin(<s>)/<f>)'
$!ALTERDATA
  EQUATION = '<angle3>=acos(<b>/<f>)'
#Find planar axis for cross-sectional plots - rotx, roty, rotz
$!ALTERDATA
  EQUATION = '<pt1>=<x>+<a>*sin(<s>)'
$!ALTERDATA
  EQUATION = '<pt2>=<y>-<a>*cos(<s>)'
$!ALTERDATA
  EQUATION = '<pt3>=<z>-<b>'
$!ALTERDATA
  EQUATION = '<den1>=sqrt(<pt1>**2+<pt2>**2)'
$!ALTERDATA
  EQUATION = '<den2>=sqrt(<pt1>**2+<pt2>**2+<pt3>**2)'
$!ALTERDATA
  EQUATION = '<ca>=atan2(<a>,<b>)'
$!ALTERDATA
```

```
  EQUATION = '<rotx>=sin(<ca>)*(<z>*sin(<s>)-<b>*<s>*sin(<s>))+<x>*cos(<ca>)-
(cos(<ca>)-1)*(cos(<s>)*(-
<a>*sin(<s>)**2+<y>*sin(<s>)+<x>*cos(<s>))+<a>*cos(<s>)*sin(<s>)**2)'
$!ALTERDATA
  EQUATION = '<roty>=<y>*cos(<ca>)-sin(<ca>)*(<z>*cos(<s>)-<b>*<s>*cos(<s>))-
(cos(<ca>)-1)*(sin(<s>)*(-
<a>*cos(<s>)**2+<x>*cos(<s>)+<y>*sin(<s>))+<a>*cos(<s>)**2*sin(<s>))'
$!ALTERDATA
  EQUATION = '<rotz>=sin(<ca>)*(<y>*cos(<s>)-<x>*sin(<s>))+<z>*cos(<ca>)-
<b>*<s>*(cos(<ca>)-1)*(cos(<s>)**2+sin(<s>)**2)'
#Find Vorticity Flux
$!ALTERDATA
  EQUATION = '<den3>=(<kappa>*<r>*sin(<theta1>)+1)'
$!ALTERDATA
  EQUATION = '<const1>=(sin(<theta1>)*sin(<s>)-
<f>*<tau>*cos(<theta1>)*cos(<s>))'
$!ALTERDATA
  EQUATION =
'<const2>=(sin(<theta1>)*cos(<s>)+<f>*<tau>*cos(<theta1>)*sin(<s>))'
$!ALTERDATA
  EQUATION =
'<const3>=(cos(<theta1>)*sin(<s>)+<f>*<tau>*sin(<theta1>)*cos(<s>))'
$!ALTERDATA
  EQUATION = '<const4>=(cos(<theta1>)*cos(<s>)-
<f>*<tau>*sin(<theta1>)*sin(<s>))'
$!ALTERDATA
  EQUATION = '<omega3>=-(<u>*<const1>-
<v>*<const2>+<kappa>*sin(<theta1>)*((<b>*<w>)/<f>+(<a>*<v>*cos(<s>))/<f>-
(<a>*<u>*sin(<s>))/<f>))/<den3>'
$!ALTERDATA
  EQUATION = '<omega2>=(<r>*(<u>*<const3>-
<v>*<const4>)+<kappa>*<r>*cos(<theta1>)*((<b>*<w>)/<f>+(<a>*<v>*cos(<s>))/<f>-
(<a>*<u>*sin(<s>))/<f>))/(<r>*(<kappa>*<r>*sin(<theta1>)+1))'
$!ALTERDATA
  EQUATION = '<Re>=3.0734'
$!ALTERDATA
  EQUATION = '<const5>=<u>*<const1>-<v>*<const2>'
$!ALTERDATA
  EQUATION = '<const6>=<u>*<const3>-<v>*<const4>'
$!ALTERDATA
  EQUATION = '<VortFlux>=-
(((<r>*<const5>+<kappa>*<r>*sin(<theta1>)*<u_s1>)/(<r>*<den3>)+(<kappa>*cos(<th
eta1>)*(<r>*<const6>+<kappa>*<r>*cos(<theta1>)*<u_s1>))/<den3>**2)/<r>+(<kappa>
*sin(<theta1>)*(<const5>+<kappa>*sin(<theta1>)*<u_s1>))/<den3>**2)/<Re>'
$!ALTERDATA
  EQUATION = '<do2>=(<omega2>(i,j,k)-<omega2>(i,j,k-1))'
$!ALTERDATA
  EQUATION = '<do3>=(<omega3>(i,j,k)-<omega3>(i,j-1,k))'
#WSS calculation
$!ALTERDATA
  EQUATION = '<WSS>=-1*<diff_us>(i,17,k)/<diff_r>(i,17,k)/<Re>(i,17,k)'
#Output the required data into tecplot files
$!WRITEDATASET  "|DIR||INPUTFILE2|"
  INCLUDETEXT = NO
  INCLUDEGEOM = NO
  INCLUDECUSTOMLABELS = NO
  INCLUDEDATASHARELINKAGE = YES
  INCLUDEAUTOGENFACENEIGHBORS = YES
  ASSOCIATELAYOUTWITHDATAFILE = NO
  ZONELIST =  [1-5]
  VARPOSITIONLIST =  [1-3,33,58,102]
  BINARY = YES
  USEPOINTFORMAT = NO
```

```
  PRECISION = 9
  TECPLOTVERSIONTOWRITE = TECPLOTCURRENT

#End loop
$!ENDLOOP
$!RemoveVar |MFBD|
#-------------------------------------------------------------------------------#
```

Appendix B: MATLAB Code to Generate Surface Grid of Helical Tube

The below MATLAB code is used to generate the surface grid of the helical tube. The tube radius (variable called 'rval') is set to 1.0 for the outer surface and to 0.5 for generating the edges of the inner block. This code is needed as GRIDGEN does not generate orthogonal surfaces in the axial direction for curved tubes and the grid generated using the below code provides better control on grid distribution in all directions.

```
%-------------------------------------------------------------------------%
clear all;
clc;

%**Set the initial radius of cylinder and circumferential raise**%
a=20;b=60/pi;

%**Define number of points on surface grid needed**%
u=linspace(0,pi,201);
v=linspace(-1*pi,pi,65);

%**Radius of tube surface - 1.0 for outer surface and 0.5 for inner
%rectangular grid surfaces**%
rval=1.0;

%**Radius Change percentage**%
RRatio =0.2;

%**Calculate the factor to find the change in radius based on
%overexpansion and appropriate transition length. r(i) is the %radius
%every axial location**%
for i=1:length(u)
   if i<101
       ti(i) = (i-90.5)/3.0*4.0*pi-2*pi;
       factor(i)=RRatio/(1.0+exp(-1.0*ti(i)));
   elseif i>=101
       ti(i) = (i-113.5)/3.0*4.0*pi-2*pi;
       factor(i)=RRatio/(1.0+exp(1.0*ti(i)));
   end
   r(i)=(1+factor(i))*rval;
end

%**Define helix properties**%
for i=1:length(u)
    C(i,:)=[a*cos(u(i)) a*sin(u(i)) b*u(i)];
    T(i,:)=[-1*a*sin(u(i)) a*cos(u(i)) b]./(a^2+b^2)^0.5;
    N(i,:)=[-1*cos(u(i)) -1*sin(u(i)) 0.0];
    B(i,:)=cross(N(i,:),T(i,:))/norm(cross(N(i,:),T(i,:)));
```

```
end

%**Define x,y, z coordinates**%
for i=1:length(u)
    for j=1:length(v)

        ar1(i,j)=B(i,1)*sin(v(j))+N(i,1)*cos(v(j));
        ar2(i,j)=B(i,2)*sin(v(j))+N(i,2)*cos(v(j));
        ar3(i,j)=B(i,3)*sin(v(j))+N(i,3)*cos(v(j));

        x(i,j)=C(i,1)+r(i)*ar1(i,j);
        y(i,j)=C(i,2)+r(i)*ar2(i,j);
        z(i,j)=C(i,3)+r(i)*ar3(i,j);

    end
end

%**Print to file here that can be read by GRIDGEN**%
f3=fopen('forL87r10pt0I201.grd','a');
for i=1:length(u)
    for j=1:length(v)
        fprintf(f3,'%d ',x(i,j));
    end
end
for i=1:length(u)
    for j=1:length(v)
        fprintf(f3,'%d ',y(i,j));
    end
end
for i=1:length(u)
    for j=1:length(v)
        fprintf(f3,'%d ',z(i,j));
    end
end
fclose(f3);
%-------------------------------------------------------------------------%
```